UNIVERSITÀ DEGLI STUDI DI TRIESTE

UNIVERSITÀ DEGLI STUDI DI TRIESTE

XXXVIII CICLO DEL DOTTORATO DI RICERCA IN FISICA

Finanziato dall'Unione europea – NextGenerationEU

FROM FUZZY SPACETIME TO CLASSICAL REALITY

Settore scientifico-disciplinare: FIS/02

DOTTORANDA
LARIA FIGURATO

COORDINATORE
PROF. ANGELO BASSI Angelo Bassi

SUPERVISORE DI TESI
PROF. ANGELO BASSI Angelo Bassi

CO-SUPERVISORI DI TESI
DR. MATTEO CARLESSO Matteo Carlesso
DR. SANDRO DONADI Donadi Sandro

ANNO ACCADEMICO 2024/2025

Finanziato dall'Unione europea NextGenerationEU | Ministero dell'Università e della Ricerca | Italiadomani | UNIVERSITÀ DEGLI STUDI DI TRIESTE

Contents

Introduction and main results

Reconciling quantum mechanics with relativity remains one of the deepest open problems in modern physics. Quantum theory superbly accounts for microscopic phenomena, while general relativity governs spacetime and the dynamics of massive bodies; yet a unified, fully consistent framework is still missing. At the heart of this tension lies the question of how quantum systems behave in gravitational fields and how the longstanding measurement problem should be resolved.

A promising avenue toward the measurement problem is provided by collapse models, which introduce stochastic and nonlinear modifications to Schrödinger dynamics. These models trigger spontaneous wave-function reduction, ensuring macroscopic localization while preserving agreement with quantum predictions at microscopic scales. Among them, the Diósi–Penrose (DP) model is especially compelling: it ties collapse to gravitational effects and thereby enables experimental scrutiny of quantum–gravitational signatures. Because the DP model departs from standard quantum mechanics, it yields testable consequences and bounds on its characteristic length scale. Matter-wave interferometry, spontaneous radiation, and astrophysical constraints such as neutron-star heating already exclude sizeable parameter regions, though substantial gaps remain. Further progress hinges on sharper theory and carefully designed experiments near the quantum–classical threshold. Here we develop theoretical upper bounds on the DP parameter by demanding that collapse be strong enough to suppress observable macroscopic superpositions.

In parallel, alternative scenarios posit that spacetime fluctuations induce gravitational decoherence. Károlyházy's original idea attributes limits on positional measurements to stochastic metric fluctuations, which in turn degrade quantum coherence. Early implementations faced difficulties—notably unrealistically large radiation rates—but subsequent refinements based on generalized correlation functions restore compatibility with experimental bounds. Part of this thesis advances precisely these refinements.

These two lines of inquiry capture distinct mechanisms by which gravity might alter quantum behavior: (i) classical, stochastic metric fluctuations that induce

decoherence while preserving linear, unitary dynamics (Károlyházy); and (ii) an intrinsically non-unitary contribution that drives objective localization (DP). In the first case, a "fuzzy" spacetime yields dephasing under a random gravitational potential without solving the measurement problem. In the second, gravity sources genuine collapse rather than mere loss of coherence from tracing out unobserved degrees of freedom.

From a conceptual standpoint, it is important to distinguish between the two broad classes of modifications of quantum dynamics that are often discussed in connection with gravity: decoherence models and collapse models. Decoherence models describe the emergence of classical behaviour as an effective process resulting from the interaction between a quantum system and additional degrees of freedom, typically treated as an environment. In this case, the fundamental dynamics remain linear and unitary, and the apparent loss of coherence arises from tracing out unobserved degrees of freedom. While decoherence successfully explains the suppression of interference effects and the stability of classical states, it does not, by itself, provide a solution to the measurement problem, since macroscopic superpositions remain valid solutions of the underlying equations of motion.

Collapse models, on the other hand, introduce genuine modifications of quantum mechanics by adding stochastic and nonlinear terms to the Schrödinger dynamics. These models aim to provide an objective mechanism for wave-function reduction, ensuring definite outcomes in individual measurements and the absence of macroscopic superpositions. Within this framework, gravity has long been considered a natural candidate for triggering collapse, both because of its universal coupling to mass and because of the conceptual tension between quantum superpositions and classical spacetime geometry. The DP model represents one of the most prominent realizations of this idea, proposing a direct link between gravitational self-energy and the collapse rate of spatial superpositions.

The Károlyházy model is properly understood as a gravitational decoherence model within this landscape. In this approach, spacetime is endowed with intrinsic stochastic fluctuations that induce dephasing in quantum systems, while preserving linearity and the superposition principle. As such, the model does not solve the measurement problem, but it provides a concrete and physically motivated framework in which gravitational effects limit the coherence of quantum states.

This thesis explores both of these perspectives in a unified way. On the one hand, we revisit and generalize the Károlyházy model, focusing on the role of space-time correlations and on the phenomenological constraints arising from radiation emission and energy conservation. On the other hand, we perform a detailed analytical and numerical study of the DP collapse model, with the goal of identifying robust theoretical bounds on its characteristic parameters, and clarifying the dependence of the collapse dynamics on the mass and geometry of the systems involved. By addressing gravitational decoherence and gravitational collapse within the same work, we aim to clarify their conceptual differences, assess their respective physical implications, and contribute to the broader effort of understanding whether gravity can play a fundamental role in the emergence of classicality.

Scope of this thesis. We develop and test both directions. On the decoherence side (Károlyházy), we formulate a more general stochastic structure that satisfies theoretical consistency and the latest experimental constraints, thereby narrowing the viable parameter window. On the collapse side (DP), we combine analytic and numerical tools to map how the collapse time scales with mass, geometry, and dimensionality; we also assess memory effects via non-Markovian generalizations. Together, these results clarify when gravity could plausibly underpin the emergence of classicality and where experiments should focus next.

Outline

This thesis is organized as follows.

- In Chapter **1**, we introduce the general framework of open quantum systems, decoherence, and collapse models. We present the conceptual and mathematical background necessary to describe how classicality can emerge from quantum dynamics, emphasizing the role of stochastic and nonlinear modifications to the Schrödinger equation.
- In Chapter **2**, we provide an overview of the relationship between quantum mechanics and gravity, focusing on various approaches to gravitationally induced decoherence. We discuss several semiclassical schemes, including the Károlyházy model, the Schrödinger–Newton equation, and recent formulations within Oppenheim's framework, outlining their conceptual motivations and limitations.
- Chapter **3** is devoted to a detailed analysis of the Károlyházy model. After revisiting its original formulation, we propose a generalized version based on a modified spacetime correlation function. The consequences of this generalization are explored both theoretically and phenomenologically, leading to updated predictions for radiation emission and energy violation, as well as refined theoretical and experimental bounds on the model's parameters.
- Chapter **4** focuses on the Diósi-Penrose model. We develop an analytic and numerical study of the model's master equation for the center of mass of macroscopic systems, with particular emphasis on determining theoretical upper bounds on the characteristic parameter R_0. We also investigate the dependence of the collapse rate on system dimensionality and examine non-Markovian generalizations of the DP dynamics.
- Finally, in Chapter **5** we summarize the main results, highlight the conceptual connections between gravitational decoherence and collapse models, and discuss future directions for both theoretical developments and experimental tests aimed at probing gravity-induced modifications of quantum mechanics.

Chapter 1

Open Quantum Systems: from Decoherence to Collapse Models

1.1 Introduction

In quantum mechanics, the evolution of a physical system is described by its quantum state, a mathematical object encoding all probabilistic information about measurable observables via the Born rule. In idealized situations where a system is perfectly isolated, its state evolves unitarily according to the Schrödinger equation, preserving the purity of the state. However, real physical systems are never completely isolated: they constantly interact with their surroundings, exchanging information and energy. The study of such systems, in which the environment cannot be neglected, falls under the framework of open quantum systems [1–4]. The standard treatment of open quantum systems begins by considering the system together with its environment as a single, isolated entity undergoing unitary dynamics. However, the total number of degrees of freedom (system plus environment) is typically enormous, often infinite, making it impossible to track the full evolution explicitly. Since our interest lies in the behavior of the system alone, one adopts a reduced description by averaging over the environmental degrees of freedom. The resulting dynamics of the system, influenced but not fully determined by the environment, define the essence of an open quantum system.

A central phenomenon emerging from this framework is decoherence [5, 6], the process by which a system loses quantum coherence with respect to a certain basis. Physically, the origin of this loss of coherence is related to the interaction between the system and a large (quantum) environment and/or classical noise. When a system interacts with its surroundings, modeled, for example, as a thermal bath, entanglement is generated between the system and environmental degrees of freedom. Although the global evolution remains unitary, the system

itself exhibits non-unitary behaviour, effectively losing information in a manner analogous to energy dissipation in classical mechanics. This loss of coherence underpins the emergence of classicality.

Despite the success of decoherence theory in explaining the quantum-to-classical transition at the level of effective states, it does not resolve the well-known measurement problem: the question of why specific outcomes are observed in individual measurements rather than statistical mixtures [7]. To address this problem, phenomenological frameworks known as collapse models have been developed [8, 9]. They modify standard quantum dynamics to include both stochasticity and nonlinearity in the Schrödinger evolution, effectively enforcing the collapse of the wave function in macroscopic regimes. They are constructed to satisfy stringent conditions. At microscopic scales, deviations from standard quantum mechanics must be negligible to remain consistent with experimental observations. At macroscopic scales, the dynamics must ensure well-localized centers of mass wave function, preventing the observation of superposition states and thereby offering a solution to the measurement problem. Strikingly, collapse models fulfill both objectives: they offer a consistent framework that connects the quantum and classical domains. For small systems, they retain the full predictive accuracy of quantum mechanics, while for macroscopic systems they enforce classical-like definiteness, thus providing a unified account of wave function dynamics across all scales.

This Chapter explores the dynamics of open quantum systems, from the mechanisms of decoherence to the theoretical structure and experimental implications of collapse models. By understanding how environmental interactions and intrinsic modifications to quantum dynamics shape the evolution of physical systems, we gain insight into the profound question of how classical reality emerges from the quantum substrate.

From a broader perspective, the theory of open quantum systems provides a unifying language to describe a wide range of physical situations in which quantum coherence is degraded, either effectively or fundamentally. In standard approaches, the reduced dynamics arises from tracing out environmental degrees of freedom, leading—under suitable assumptions—to Markovian master equations of Lindblad type. More refined descriptions relax these assumptions and give rise to non-Markovian dynamics, memory effects, colored noise, and time-dependent generators. Such extensions are essential whenever the environment

has a structured spectrum or long correlation times.

Within this framework, both decoherence models and collapse models can be interpreted as specific realizations of open-system dynamics. Environmental decoherence corresponds to an effective reduced description of an underlying unitary evolution. In collapse models, the role of the bath is played by a classical noise field, to which the system is coupled through nonlinear terms in the dynamics. Both approaches admit a master-equation formulation and can be analyzed using the same mathematical tools developed for open quantum systems. This formal overlap makes it possible to compare their physical predictions and to identify experimentally testable signatures that distinguish effective decoherence from genuine collapse mechanisms.

In the following sections, we introduce the general formalism of open quantum systems and show how decoherence and collapse models naturally fit within it. This will provide the conceptual and mathematical groundwork for the gravitational decoherence and collapse scenarios analyzed in the rest of the thesis.

1.2 Open Quantum Systems

In the following, we outline the general properties and features of open quantum systems. For a more detailed exposition of the theory, we refer the reader to [1–5].

1.2.1 Reduced state and its evolution

In the study of open quantum systems [2], one typically considers the system of interest S as coupled to an external environment E. The Hilbert space is thus given by the tensor product $\mathcal{H} = \mathcal{H}_S \otimes \mathcal{H}_E$. The total composite $S + E$ is treated as a closed system, whose dynamics are governed by the unitary time evolution generated by the total Hamiltonian

$$\hat{H} = \hat{H}_S + \hat{H}_E + \hat{H}_{int}, \tag{1.1}$$

with the system and environment associated with $\hat{H}_S$ and $\hat{H}_E$, respectively, and where $\hat{H}_{int}$ describes the interaction between system and environment. The complete state of the composite is described by a density operator $\hat{\rho}_{SE}(t)$, evolving

according to the Liouville–von Neumann equation

$$i\hbar\frac{\mathrm{d}}{\mathrm{d}t}\hat{\rho}_{SE}(t) = [\hat{H}, \hat{\rho}_{SE}(t)]. \tag{1.2}$$

Since our interest is solely in the system d.o.f., one introduces the reduced density matrix by tracing over the environment

$$\hat{\rho}_S(t) = \mathrm{Tr}^{(E)}\big[\hat{\rho}_{SE}(t)\big]. \tag{1.3}$$

This reduced state contains all accessible information about the system and provides the correct statistical predictions for any observable acting on $\mathcal{H}_S$. Its dynamics, however, is in general non-unitary, reflecting the influence of the environment. To implement the partial trace explicitly, one chooses any orthonormal basis $\{|\psi_i^{(E)}\rangle\}$ on the environmental Hilbert space. The reduced state is then obtained as the sum

$$\hat{\rho}_S(t) = \sum_i \langle\psi_i^{(E)} \,|\, \hat{\rho}_{SE}(t) \,|\, \psi_i^{(E)}\rangle, \tag{1.4}$$

which is independent of the basis choice and thus well defined.

The operator $\hat{\rho}_S(t)$ inherits the defining properties of a quantum state: it is Hermitian, linear, positive semidefinite, and normalized with unit trace $\mathrm{Tr}^{(S)}\big[\hat{\rho}_S(t)\big] = 1$. The system's time evolution can be represented as a reduced dynamical map $\hat{\Phi}_t$ acting on the initial system state $\hat{\rho}_S$. Namely, this is constructed as

$$\hat{\Phi}_t :\ \hat{\rho}_S \longmapsto \hat{\rho}_S(t) = \mathrm{Tr}^{(E)}\Big[\,\hat{U}_t\,\hat{\rho}_{SE}\,\hat{U}_t^{\dagger}\Big]\,, \tag{1.5}$$

which departs from unitarity because tracing out the environment destroys reversibility. We note that the construction of the reduced dynamical map $\hat{\Phi}_t$ as a map from system states $\hat{\rho}_S$ to $\hat{\rho}_S(t)$ is strictly valid only if the initial global state is factorized, $\hat{\rho}_{SE} = \hat{\rho}_S \otimes \hat{\rho}_E$, with a fixed environment state $\hat{\rho}_E$. In the general case of correlated initial states, $\hat{U}_t$ followed by a partial trace defines a map from global states to system states, but not a well-defined map acting solely on the system's density operators. Here $\hat{U}(t) = \mathcal{T}\,\exp\Big(-\frac{i}{\hbar}\int_0^t \hat{H}(s)\,ds\Big)$ is the global unitary evolution generated by the total Hamiltonian $\hat{H}$ where $\mathcal{T}$ denote the time ordering (which is not required if $\hat{H}$ is time independent). Operationally, $\hat{\Phi}_t$ results from

the composition of the global unitary $\hat{U}_t$ followed by the environmental trace

$$\hat{\rho}_{SE} \xrightarrow{\hat{U}_t} \hat{\rho}_{SE}(t) = \hat{U}_t \hat{\rho}_{SE} \hat{U}_t^\dagger \xrightarrow{\mathrm{Tr}^{(E)}} \hat{\rho}_S(t) = \mathrm{Tr}^{(E)}\left[\hat{U}_t \hat{\rho}_{SE} \hat{U}_t^\dagger\right], \tag{1.6}$$

or equivalently

$$\hat{\rho}_{SE} \xrightarrow{\mathrm{Tr}^{(E)}} \hat{\rho}_S \xrightarrow{\hat{\Phi}_t} \hat{\rho}_S(t) = \mathrm{Tr}^{(E)}\left[\hat{U}_t \hat{\rho}_{SE} \hat{U}_t^\dagger\right]. \tag{1.7}$$

Both representations highlight that the reduced dynamics is induced by the system–environment coupling rather than by an autonomous unitary on the system's Hilbert space $\mathcal{H}_S$. The reduced dynamical map admits a time-ordered exponential representation reading

$$\hat{\Phi}_t[\,\cdot\,] = \mathcal{T} \exp\left(\int_0^t \mathrm{d}s\, \mathcal{L}_s\right)[\,\cdot\,], \tag{1.8}$$

where $\mathcal{L}_s$ the generator of the evolution. Differentiating this representation yields the most important dynamical equation in the theory of the open quantum system: *the quantum master equation*

$$\frac{\mathrm{d}}{\mathrm{d}t}\hat{\rho}_S(t) = \mathcal{L}_t[\hat{\rho}_S(t)]\,. \tag{1.9}$$

Any map $\hat{\Phi}_t$ preserves the density-operator character of the state, related to the probability interpretation we give to $\hat{\rho}_S$: its diagonal terms, taken in the eigenbasis of the measured observable, describe the probabilities of finding the system in a particular state

$$\hat{\Phi}_t[\hat{\rho}_S] \geq 0, \qquad \left(\hat{\Phi}_t[\hat{\rho}_S]\right)^\dagger = \hat{\Phi}_t[\hat{\rho}_S], \qquad \mathrm{Tr}^{(S)}[\hat{\rho}_S] = 1. \tag{1.10}$$

The off-diagonal terms represent quantum coherences between different basis states, responsible for interference phenomena; their decay through decoherence leads to the emergence of classical statistical mixtures.

Complete positivity

To ensure that these probabilistic and coherence properties of the density operator are consistently preserved under time evolution, one requires the dynamical map to satisfy a stronger condition than mere positivity, namely Complete Positivity

(CP).

A linear map

$$\hat{\Phi} : \mathcal{B}(\mathcal{H}_S) \to \mathcal{B}(\mathcal{H}_S), \tag{1.11}$$

is called positive if it maps positive operators to positive operators, i.e.

$$\hat{\rho} \geq 0 \quad \Rightarrow \quad \hat{\Phi}(\hat{\rho}) \geq 0. \tag{1.12}$$

It is called CP if positivity is preserved even when the map acts only on part of a larger system, namely

$$\hat{\mathbb{1}}_n \otimes \hat{\Phi} \ \text{ is positive} \quad \forall n \in \mathbb{N}, \tag{1.13}$$

where $\mathbb{1}_n$ identifies the identity operator acting on N-dimensional Hilbert space.

Physically, complete positivity guarantees that the evolution is valid even in the presence of entanglement with an arbitrary ancilla, a necessary condition for the consistency of open quantum system dynamics.

1.2.2 Lindblad equation

A central example of a generator $\mathcal{L}$ in Eq. (1.9) is the so-called Lindblad equation [10, 11]. For an N-dimensional system, the most general time-independent, trace-preserving CP generator reads

$$\mathcal{L}[\hat{\rho}_S(t)] = -\frac{i}{\hbar}\left[\hat{H}_S, \hat{\rho}_S(t)\right] + \sum_{a,b=1}^{N^2-1} K_{ab}\left[\hat{L}_a \hat{\rho}_S(t) \hat{L}_b^\dagger - \frac{1}{2}\{\hat{L}_b^\dagger \hat{L}_a, \hat{\rho}_S(t)\}\right], \tag{1.14}$$

where $\hat{H}_S$ is the system Hamiltonian, $\hat{L}_a$ are the Lindblad (noise) operators, and K_{ab} are the entries of the Kossakowski matrix. The first term describes the free coherent evolution with respect to the system Hamiltonian $\hat{H}_S$, as it is isolated. Dissipation, diffusion, and decoherence originate from the dissipator (the last term).

The Lindblad master equation provides the most general form of a Markovian, time-homogeneous, and completely positive quantum dynamical semigroup. Its validity relies on a number of physical assumptions concerning the interaction between system and environment. In particular, the coupling between the system and the environment is assumed to be sufficiently weak so that correlations

built up during the evolution remain negligible. Moreover, the environmental degrees of freedom are characterized by a very short correlation time compared to the typical timescales of the system dynamics, allowing one to neglect memory effects and to approximate the environment as being continuously reset to a stationary state.

Under these conditions, the reduced dynamics of the system become Markovian, in the sense that the future evolution depends only on the instantaneous state of the system and not on its past history. This property leads to a dynamical map that satisfies the semigroup composition law and admits a generator of Lindblad form. Deviations from these assumptions generally result in non-Markovian dynamics, which cannot be captured by a time-independent Lindblad equation and typically require memory kernels or time-dependent generators.

An important feature of Lindblad dynamics is that it admits a stochastic representation in terms of quantum trajectories. In this picture, the master equation can be obtained by averaging over stochastic evolutions of the system state, driven by classical noise processes. When the environment is characterized by delta-correlated fluctuations, the corresponding unravelings involve Gaussian white-noise terms, leading to stochastic Schrödinger equations. This connection provides a natural bridge between the theory of open quantum systems and collapse models, where white-noise stochastic dynamics is postulated at a fundamental level.

1.3 Decoherence

Decoherence corresponds to the loss of quantum coherence, often interpreted as the transfer of information from a system to its environment.

However, if the system is not perfectly isolated, for instance, during a measurement, coherence is shared with the environment and appears to degrade over time. This process is known as quantum decoherence or environmental decoherence. The coherence is not truly lost; rather, it becomes distributed among many degrees of freedom in the environment, similar to how energy appears to be "lost" to friction in classical mechanics while actually being converted into heat in the surroundings.

1.3.1 Concise overview

Decoherence is the process by which interference terms in the reduced state of a quantum system are suppressed as a consequence of its coupling to external degrees of freedom. Let us pursue a purely quantum mechanical account in terms of von Neumann measurement scheme and entanglement [5, 12]. This description will become the basis for our description of the process of decoherence, where the environment will assume the role of the which-path detector.

In order to illustrate the mechanism of decoherence, we present a simple but insightful example. This scenario allows us to explicitly show how the loss of coherence arises due to the interaction between a quantum system and its environment. Let us consider a particle prepared in a superposition of two wave packets, one propagating to the right and the other to the left

$$|\psi\rangle = \frac{|R\rangle + |L\rangle}{\sqrt{2}}. \tag{1.15}$$

Assume that a gas particle is localized along the rightward path, initially in the state $|\phi\rangle$. Before any interaction takes place, the joint state of the system is

$$|\Psi_i\rangle = |\psi\rangle\,|\phi\rangle, \tag{1.16}$$

whereas after the interaction it evolves into

$$|\Psi_f\rangle = \frac{|R,\phi_s\rangle + |L,\phi\rangle}{\sqrt{2}}, \tag{1.17}$$

with $|\phi_s\rangle$ denoting the scattered state of the gas particle.

The initial density matrix $\hat{\rho}_i$ of the system, expressed in the $\{|R\rangle, |L\rangle\}$ basis, is given by

$$\begin{aligned} \hat{\rho}_i &= \mathrm{Tr}_g\big[\,|\Psi_i\rangle\langle\Psi_i|\,\big] = |\psi\rangle\langle\psi| = \\ &= \tfrac{1}{2}\big(|R\rangle\langle R| + |R\rangle\langle L| + |L\rangle\langle R| + |L\rangle\langle L|\big) \quad \longrightarrow \quad \frac{1}{2}\begin{pmatrix} 1 & 1 \\ 1 & 1 \end{pmatrix}. \end{aligned} \tag{1.18}$$

The arrow simply indicates the transition from the explicit operator form of the density matrix to its matrix representation in the $\{|R\rangle, |L\rangle\}$ basis. At the end of the process, the final density matrix $\hat{\rho}_f$ of the system in the same basis takes the

form

$$\hat{\rho}_f = \mathrm{Tr}_g\big[\,|\Psi_f\rangle\langle\Psi_f|\,\big] = \\ = \tfrac{1}{2}\Big(|R\rangle\langle R| + |R\rangle\langle L|\,\langle\phi|\phi_s\rangle + |L\rangle\langle R|\,\langle\phi_s|\phi\rangle + |L\rangle\langle L|\Big) \;\longrightarrow\; \frac{1}{2}\begin{pmatrix} 1 & \langle\phi|\phi_s\rangle \\ \langle\phi_s|\phi\rangle & 1 \end{pmatrix}. \tag{1.19}$$

In general, $\big|\langle\phi_s|\phi\rangle\big| < 1$ underlying the coherence reduction. Moreover, if instead of a single gas particle there are n such particles, the overlap scales as $\langle\phi_s|\phi\rangle^n$, which is even closer to zero. As the off-diagonal elements tend to vanish, quantum coherences are lost, and consequently, the interference effects disappear.

1.4 Measurement Problem

The theory of Quantum Mechanics is based on the following set of rules [13]

1. The state of a quantum system is described by a vector in Hilbert space.
2. The state evolves according to the Schrödinger equation. A fundamental property of the Schrödinger equation is linearity: the linear combination of two solutions is a new solution. This is the quantum superposition principle.
3. Physical quantities are represented by specific self-adjoint operators. Their (real) eigenvalue represent the possible outcomes of measurements of those quantities.
4. In a measurement, outcomes are random and distributed according to the Born rule $|\langle a_n|\psi\rangle|^2$, where $|a_n\rangle$ is the eigenstate corresponding to the eigenvalues that has been observed when the system is in the state. After the measurement, the wave function collapses into the eigenstate corresponding to the eigenvalues that have been obtained. This is the von Neumann projection postulate.

It is evident that this set of rules contains an ambiguity [7, 14–17]. There is nothing fundamentally wrong with having two distinct types of evolution—Schrödinger and collapse. The issue lies in the theory's ambiguity regarding when each should be applied. When left undisturbed, a quantum system evolves according to the Schrödinger equation, possibly forming superpositions; yet, when a measurement is performed, it undergoes a random collapse. From a phenomenological

standpoint, this seems reasonable: in the first case the system is isolated, while in the second, it interacts with a measuring apparatus. The difficulty, however, lies in the fact that quantum theory is not intended to be merely phenomenological, but rather a fundamental account of nature. If the dualism between "isolated" and "measured" systems is taken seriously as a fundamental aspect of nature, then the distinction between the two is not merely a practical or epistemic one, but must correspond to a genuine physical property of reality: that is, nature itself would make an objective distinction between the two situations. But the justification for such a distinction is far from obvious: measuring devices themselves are composed of atoms, which are quantum in nature. Consequently, they too should admit a quantum-mechanical description. If consistently applied to a system including the measurement apparatus, the Schrödinger equation predicts the unitary evolution of the combined system. Due to its linearity, microscopic superpositions become entangled with the apparatus degrees of freedom, giving rise to macroscopic superpositions as illustrated by Schrödinger's famous cat paradox [14]. However, this unitary evolution does not account for the emergence of definite outcomes in individual measurements: instead of selecting a single result, it predicts a superposition of macroscopically distinct states of the apparatus. This mismatch between the linear, deterministic evolution of the quantum state and the definite outcomes observed in experiments constitutes the measurement problem in quantum mechanics.

1.5 Collapse models

The measurement problem in quantum mechanics finds a potential resolution in collapse models (CM). CM are phenomenological approaches developed to describe the quantum-to-classical transition, i.e. the passage from the microscopic regime, where quantum mechanics provides an accurate description, to the macroscopic regime, in which physical systems are never observed in superposition states. CM modify standard quantum dynamics in two key ways. First, they introduce a nonlinearity into Schrödinger's equation to enforce wave function collapse. Second, they incorporate stochasticity, a necessary feature, as deterministic nonlinear evolution would permit superluminal communication via entangled systems [18, 19].

Beyond these foundational aspects, CM must satisfy critical constraints. At microscopic scales, deviations from standard quantum mechanics must remain undetectable to preserve agreement with experiments. Conversely, at macroscopic scales, the dynamics must ensure a well-localized center of mass wave function, eliminating quantum superpositions and thus addressing the measurement problem.

Remarkably, these models achieve both requirements [8, 9], bridging the quantum and classical domains. They maintain the accuracy of quantum predictions for small systems while enforcing collapse in large systems, providing a unified framework for wave function behavior across all scales.

1.5.1 The general structure of collapse equations

At the core of CM lies a fundamental proposition: the wave function collapse is spontaneously there in nature, and not some ad-hoc postulate introduced when a measurement happens. In the most studied CM, the Continuous Spontaneous Localization model and the Diósi–Penrose model, the collapse emerges as a continuous process, driven by interaction with an external noise field. This dynamics is mathematically described through stochastic differential equations, a formulation that is not arbitrary but rather uniquely determined by fundamental constraints.

While the physical origin of the collapse mechanism remains unknown, rendering these models phenomenological, their theoretical consistency is exceptional. To date, no alternative approach has been shown to introduce nonlinearity into quantum mechanics without conflicting with relativistic causality or probability conservation. Thus, despite their provisional nature, CM currently offer the only mathematically rigorous framework known for unifying quantum dynamics with objective wave function reduction [20].

First of all, we summarize the general features of collapse equations. The dynamics is represented by a stochastic Schrödinger equation, valid only in the Markovian case, of the form [21]

$$\mathrm{d}|\phi_t\rangle = \Big[-\frac{i}{\hbar}\hat{H}\mathrm{d}t + \sqrt{\gamma}\sum_{i=1}^{N}(\hat{A}_i - \langle\hat{A}_i\rangle_t)\mathrm{d}W_{i,t} - \frac{\gamma}{2}\sum_{i=1}^{N}(\hat{A}_i - \langle\hat{A}_i\rangle_t)^2\mathrm{d}t\Big]|\phi_t\rangle, \quad (1.20)$$

where $\hat{H}$ is the standard quantum hamiltonian of the system, $\hat{A}_i$ are a set of commuting self-adjoint operators, $W_{i,t}$ are N independent standard Wiener processes (a noise without drift and with no memory [22]), $\langle \hat{A}_i \rangle_t \equiv \langle \psi_t | \hat{A}_i | \psi_t \rangle$ is the standard quantum expectation of $\hat{A}_i$, and γ is a positive constant which sets the strength of the collapse process. The presence of terms $\langle \hat{A}_i \rangle_t$ introduces nonlinearity to the dynamics, which are necessary in order to suppress quantum superpositions. The Wiener process $W_{i,t}$ adds stochasticity; hence, the collapse occurs randomly, and it can be shown that it happens in agreement with the Born rule. While the first term on the equation's right hand side represents standard Schrödinger evolution, the remaining two govern wave function collapse. The several collapse models that have been proposed so far differ from each other basically only by the choice of the localizing operators, and the characteristics of the noises W.

To clarify the collapse mechanism and its connection to operators $\hat{A}_i$, we examine Eq. (1.20) without the Hamiltonian term. This analysis reveals that all initial states evolve toward the (common) eigenstates of $\hat{A}_i$ [21]. The reduction properties of Eq. (1.20) can easily be verified by computing the time evolution of the variance $V_{\hat{A}}(t) \equiv \langle \hat{A}^2 \rangle_t - \langle \hat{A} \rangle_t^2$ of an operator $\hat{A}$ that commutes with all the operators $\hat{A}_i$. As shown for example in [23], by using standard Itô calculus rules, one gets for the average value $\mathbb{E}[V_{\hat{A}}(t)]$ the following equation

$$\mathbb{E}[V_{\hat{A}}(t)] = V_{\hat{A}}(0) - 4\gamma \sum_{i=1}^{N} \int_0^t \mathrm{d}s \, \mathbb{E}\big[C^2_{\hat{A},\hat{A}_i}(s)\big], \tag{1.21}$$

where $C_{\hat{A},\hat{A}_i}(t) \equiv \langle (\hat{A} - \langle \hat{A} \rangle_t)(\hat{A}_i - \langle \hat{A}_i \rangle_t) \rangle_t$ is the correlation between the operator $\hat{A}$ and $\hat{A}_i$. Given that $V_{\hat{A}}(t)$ must remain positive for all times t and the second term on the right-hand side of Eq. (1.21) is always negative, it necessarily follows that $C_{\hat{A},\hat{A}_i}(t) \to 0$ as $t \to \infty$ for any i. Therefore, if we choose $\hat{A}$ as one of the operators $\hat{A}_i$, this implies that its variance $V_{\hat{A}_i}(t) = C_{\hat{A}_i,\hat{A}_i}(t)$ goes to zero for large enough times. This means that any initial state $|\phi_0\rangle$ converges asymptotically to one of the common eigenstates of the operators $\hat{A}_i$.

1.5.2 The master equation

We derive now the master equation related to Eq. (1.20). Using here the Itô product rule, we have

$$\begin{aligned}
\mathrm{d}(|\phi_\mathrm{t}\rangle\langle\phi_\mathrm{t}|) &= (\mathrm{d}|\phi_\mathrm{t}\rangle)\langle\phi_\mathrm{t}| + |\phi_\mathrm{t}\rangle(\mathrm{d}\langle\phi_\mathrm{t}|) + (\mathrm{d}|\phi_\mathrm{t}\rangle)(\mathrm{d}\langle\phi_\mathrm{t}|) = \\
&= \Big[-\frac{i}{\hbar}\hat{H}\mathrm{dt} + \sqrt{\gamma}\sum_{\mathrm{i}=1}^{\mathrm{N}}(\hat{\mathrm{A}}_\mathrm{i} - \langle\hat{\mathrm{A}}_\mathrm{i}\rangle_\mathrm{t})\mathrm{dW}_{\mathrm{i,t}} - \frac{\gamma}{2}\sum_{\mathrm{i}=1}^{\mathrm{N}}(\hat{\mathrm{A}}_\mathrm{i} - \langle\hat{\mathrm{A}}_\mathrm{i}\rangle_\mathrm{t})^2\mathrm{dt}\Big]|\phi_\mathrm{t}\rangle\langle\phi_\mathrm{t}| \\
&+ |\phi_t\rangle\langle\phi_t|\Big[\frac{i}{\hbar}\hat{H}dt + \sqrt{\gamma}\sum_{i=1}^{N}(\hat{A}_i - \langle\hat{A}_i\rangle_t)\mathrm{dW}_{\mathrm{i,t}} - \frac{\gamma}{2}\sum_{\mathrm{i}=1}^{\mathrm{N}}(\hat{\mathrm{A}}_\mathrm{i} - \langle\hat{\mathrm{A}}_\mathrm{i}\rangle_\mathrm{t})^2\mathrm{dt}\Big]|\phi_\mathrm{t}\rangle\langle\phi_\mathrm{t}| \\
&+ \gamma\sum_{i=1}^{N}(\hat{A}_i - \langle\hat{A}_i\rangle_t)|\phi_t\rangle\langle\phi_t|(\hat{A}_i - \langle\hat{A}_i\rangle_t)\mathrm{dt}. \qquad (1.22)
\end{aligned}$$

It can be shown that through a direct calculation all the terms involving $\langle\hat{A}_i\rangle_t$ and $\langle\hat{A}_i\rangle_t^2$ multiplied with dt cancel each other, and the expectation value of the terms containing $\mathrm{dW}_{\mathrm{i,t}}$ is zero.

Therefore, the equation for the density matrix $\hat{\rho}(t) = \mathbb{E}[|\phi_t\rangle\langle\phi_t|]$ becomes

$$\frac{\mathrm{d}\hat{\rho}(\mathrm{t})}{\mathrm{dt}} = \frac{i}{\hbar}[\hat{\rho}(t), \hat{H}] - \frac{\gamma}{2}\sum_{i=1}^{N}\{\hat{A}_i^2\hat{\rho}(t) + \hat{\rho}(t)\hat{A}_i^2 - 2\hat{A}_i\hat{\rho}(t)\hat{A}_i\}. \qquad (1.23)$$

If we rewrite the second term in a more compact way, we obtain

$$\mathcal{L}[\hat{\rho}(t)] = -\frac{i}{\hbar}[\hat{H}, \hat{\rho}(t)] + \sum_{i=1}^{N}\gamma\left[\hat{A}_i\hat{\rho}(t)\hat{A}_i - \frac{1}{2}\{\hat{A}_i\hat{A}_i, \hat{\rho}(t)\}\right], \qquad (1.24)$$

which is precisely of a Lindblad form discussed above in Eq. (1.14). For simplicity, throughout this Chapter we restrict ourselves to the Markovian (white-noise) case, which already captures the essential structure of collapse models. Non-Markovian generalizations, involving colored noise and memory effects, will be discussed only when required, in particular in Section 4.4.

1.5.3 The Continuous Spontaneous Localization model

The Continuous Spontaneous Localization (CSL) model, which was formulated by Ghirardi, Rimini, and Pearle in 1990 [23]. In the CSL model, the collapse is continuous in time, described by a stochastic differential equation of the same

form as those used in the theory of continuous measurements. The wave function is subject to a continuous spontaneous collapse, driven by a family of Wiener processes $W(\mathbf{x}, t)$, one for each point of space $\mathbf{x}$, which is of the form introduced in Eq. (1.20).

The collapse equation for the wave function reads

$$\begin{aligned} \mathrm{d}|\psi_t\rangle = \Bigg[-\frac{i}{\hbar}\hat{H}\,\mathrm{d}t + \sqrt{\frac{\gamma}{m_0}} \int \mathrm{d}\mathbf{x}\, \big(\hat{M}(\mathbf{x}) - \langle \hat{M}(\mathbf{x})\rangle_t\big)\, \mathrm{d}W_t(\mathbf{x}) \\ - \frac{\gamma}{2m_0^2} \int \mathrm{d}\mathbf{x}\, \big(\hat{M}(\mathbf{x}) - \langle \hat{M}(\mathbf{x})\rangle_t\big)^2\, \mathrm{d}t \Bigg] |\psi_t\rangle, \end{aligned} \tag{1.25}$$

where continuous label $\mathbf{x}$ corresponding positions in space. We see that Eq. (1.25) is of the same form of Eq. (1.20) above, with the discrete index j replaced by the continuos variables $\mathbf{x}$. The collapse operators are chosen in order to satisfy the following requirements:

1. A macroscopic object must be well localized in space;
2. The model should be able to describe systems of identical particles.

Both conditions lead to the choice of a continuous set of operators $\hat{M}(\mathbf{x})$, one for each point of space $\mathbf{x}$

$$\hat{M}(\mathbf{x}) = \sum_{j,s} m_j \int \mathrm{d}\mathbf{y}\, g(\mathbf{x}-\mathbf{y})\, \hat{\psi}_j^\dagger(\mathbf{y}, s)\, \hat{\psi}_j(\mathbf{y}, s), \tag{1.26}$$

where m_j is the mass of the particles of the j-th kind. Here, $\hat{\psi}_j^\dagger(\mathbf{y}, s)$ and $\hat{\psi}_j(\mathbf{y}, s)$ are respectively the creation and annihilation operators of a particle of type j in the point $\mathbf{y}$ with spin s and

$$g(\mathbf{x}-\mathbf{y}) = \frac{1}{\left(\sqrt{2\pi}\, r_C\right)^3} \exp\left(-\frac{(\mathbf{x}-\mathbf{y})^2}{2r_C^2} \right), \tag{1.27}$$

is a Gaussian smearing function where the parameter r_C describes the length-scale above which the collapse is more effective. The Wiener increments associated with different points in space are independent, so we have $\mathbb{E}[\,\mathrm{d}W_t(\mathbf{x})\,] = 0$ and $\mathbb{E}[\,\mathrm{d}W_t(\mathbf{y})\,\mathrm{d}W_t(\mathbf{y})\,] = \delta(\mathbf{x}-\mathbf{y})\,\mathrm{d}t$.

In the CSL model, the amplified rate depends on the distance between the particles composing the system with respect to r_C. Two limiting cases are relevant

[24]: one can show that when r_C is much smaller than the distance between the particles, one gets $\lambda \simeq N\lambda$; on the other hand, when r_C is much larger than the size of the system, one gets a quadratic amplification in the number of particles $\lambda \simeq N^2\lambda$.

This amplification mechanism is a key feature of the CSL model, as it ensures the emergence of classical behaviour for macroscopic objects while leaving microscopic systems essentially unaffected. Physically, the amplification arises because the collapse noise couples to the mass density of the system: when many particles are present, their individual contributions to the localization process add up, leading to a much faster suppression of spatial superpositions.

As a representative example, consider a rigid macroscopic body whose linear size is much smaller than the correlation length r_C. In this regime, all particles are effectively localized by the same noise realization, and the collapse rate scales quadratically with the total mass (or equivalently with the number of constituents), leading to an extremely fast localization of the center-of-mass wave function. In contrast, for extended or dilute systems whose size exceeds r_C, different parts of the system experience approximately independent noise contributions. In this case, the amplification becomes linear in the number of particles, and the collapse acts locally on each constituent. This ensures that spatial superpositions of macroscopic objects are dynamically suppressed on very short time scales.

On the other hand, microscopic systems such as atoms or small molecules exhibit negligible deviations from standard quantum mechanics, while mesoscopic systems interpolate smoothly between the microscopic and macroscopic regimes.

This mass-dependent amplification mechanism lies at the heart of the empirical viability of the CSL model, allowing it to reconcile the persistence of quantum coherence at small scales, with the absence of macroscopic superpositions in everyday life experience.

1.5.4 The Diósi–Penrose model

In the present Subsection, we introduce only the essential elements of the model, while a detailed and comprehensive analysis will be presented in Chapter 4.

The Diósi–Penrose model falls within the class of models of spontaneous wave function collapse, and it is specified by setting the correlation function of the noise equal to the Newtonian gravitational potential. The model was first proposed by Diósi [25, 26], and later revived by Penrose [27], based on independent arguments on the behavior of spacetime in the presence of quantum superpositions.

Namely, the dynamical equation for the wave function in this model reads [26]

$$\begin{aligned} \mathrm{d}|\psi(\mathrm{t})\rangle = \Bigg[& -\frac{i}{\hbar}\hat{H}\,\mathrm{d}t + \sqrt{\frac{G}{\hbar}}\int \mathrm{d}\mathbf{r}\,(\hat{\mu}(\mathbf{r}) - \langle\hat{\mu}(\mathbf{r})\rangle_t)\,\mathrm{d}W_t(\mathbf{r}) \\ & - \frac{G}{2\hbar}\int \mathrm{d}\mathbf{r}\,\mathrm{d}\mathbf{r}'\,\frac{(\hat{\mu}(\mathbf{r}) - \langle\hat{\mu}(\mathbf{r})\rangle_t)(\hat{\mu}(\mathbf{r}') - \langle\hat{\mu}(\mathbf{r}')\rangle_t)}{|\mathbf{r}-\mathbf{r}'|}\Bigg]|\psi(t)\rangle, \end{aligned} \tag{1.28}$$

where $\hat{\mu}(\boldsymbol{r})$ is mass density operator, and the Wiener processes have correlation $\mathbb{E}\big[\,\mathrm{d}W_t(\mathbf{r})\,\mathrm{d}W_t(\mathbf{r}')\,\big] = 1/|\mathbf{r}-\mathbf{r}'|\,\mathrm{d}t$.

The corresponding master equation describing the time evolution for the statistical operator $\hat{\rho}(t)$ of a generic particles system under the DP dynamics is given by

$$\frac{\mathrm{d}\hat{\rho}(\mathrm{t})}{\mathrm{dt}} = -\frac{i}{\hbar}\big[\hat{H},\hat{\rho}(t)\big] + \mathcal{D}[\hat{\rho}(t)], \tag{1.29}$$

where $\hat{H}$ is the standard Hamiltonian and

$$\mathcal{D}[\hat{\rho}(t)] = -\frac{4\pi G}{\hbar}\int \mathrm{d}\mathbf{r}\int \mathrm{d}\mathbf{r}'\frac{1}{|\mathbf{r}-\mathbf{r}'|}\big[\hat{\mu}(\mathbf{r}'),\big[\hat{\mu}(\mathbf{r}),\hat{\rho}(\mathrm{t})\big]\big], \tag{1.30}$$

describes the DP non-unitary term. This term is responsible for the collapse, whose strength is determined by the Newtonian interaction (with G being the gravitational constant) and by the mass density operator $\hat{\mu}(\boldsymbol{r})$ of the system.

To determine how fast the model collapses in space, one can neglect the Hamiltonian evolution and look at the dynamics of the off-diagonal elements in the position basis, which reads

$$\langle\mathbf{x}|\hat{\rho}(t)|\mathbf{y}\rangle = \langle\mathbf{x}|\hat{\rho}(0)|\mathbf{y}\rangle\,e^{-t/\tau}, \tag{1.31}$$

where we introduced the time of decay τ defined as

$$\tau^{-1} = \frac{G}{2\hbar}\int \mathrm{d}\mathbf{r}\int \mathrm{d}\mathbf{r}'\,\frac{\big[\mu(\mathbf{r}-\mathbf{x})-\mu(\mathbf{r}-\mathbf{y})\big]\big[\mu(\mathbf{r}'-\mathbf{x})-\mu(\mathbf{r}'-\mathbf{y})\big]}{|\mathbf{r}-\mathbf{r}'|}, \tag{1.32}$$

where $\mu(\mathbf{r})$ is the mass density of the system. If one considers a point-like particle, i.e. $\mu(\mathbf{x}) = m\delta(\mathbf{x})$, the integral in Eq. (1.32) diverges, predicting an instantaneous collapse regardless of how small the particle's mass is. This is clearly in contradiction with observations. To avoid such standard divergences, that occur when dealing with point-like masses, the mass density is smeared over a width R_0, which is the only free parameter of the DP model. Specifically, by assuming for convenience that the mass density as well as the smearing are of a Gaussian form [28], for a system of N distinguishable particles of radius R_i, mass m_i and of position operator $\hat{\boldsymbol{x}}_i$, one has

$$\hat{\mu}(\boldsymbol{r}) = \sum_{i=1}^{N} \frac{m_i}{(2\pi R_{\text{eff},i}^2)^{3/2}} e^{-\frac{(\boldsymbol{r}-\hat{\boldsymbol{x}}_i)^2}{2R_{\text{eff},i}^2}}, \tag{1.33}$$

where $R_{\text{eff},i} = \sqrt{R_0^2 + R_i^2}$ is the effective radius of the particle. In the point-like particle limit, $R_{\text{eff},i}$ reduces to R_0.

To conclude, Eq. (1.32) indicates that objects with large masses collapse faster compared to small ones: to give an estimation [24], the time of decay for a proton is $\tau \simeq 10^6$ years, while for a dust of grain (assumed to be spherical) with a radius of 10μm and a mass of 10^{-12} kg one gets $\tau \simeq 10^{-8}$s.

While this provides only a rough estimation of the collapse time τ and its dependence on mass, in Chapter 4 we will carry out a more detailed analysis to determine the collapse time τ for rigid bodies and to examine how it depends on their geometry.

Chapter 2

Quantum Mechanics, Gravity, and the Challenge of Unification

2.1 Introduction

Quantum Mechanics (QM) and General Relativity (GR) stand as the two foundational pillars of modern physics. While QM governs the behavior of microscopic systems—atoms, molecules, and fundamental particles—GR provides an elegant and accurate description of the macroscopic world, including massive bodies and spacetime itself. Despite their unparalleled successes in their respective domains, a fully consistent unification of these two theories remains an open challenge. Understanding how gravity influences quantum systems [29–31], or how quantum behavior persists under gravitational interaction, lies at the heart of this unresolved tension.

Historically, the dominant approach to unification has focused on quantizing gravity [32–36]. In this framework, one aims to describe gravitational interactions in the same language as quantum field theory, ultimately leading to a theory of Quantum Gravity (QG). While notable progress has been made, such as string theory and loop quantum gravity, no single proposal has yet emerged as a complete and experimentally verified theory. This situation is compounded by the fact that experimental access to quantum-gravitational effects is extremely limited, particularly at the Planck scale, where these phenomena are expected to be most prominent [33–35, 37]. In recent years, attention has increasingly shifted from the inaccessible high-energy Planck regime toward low-energy, table-top experiments designed to probe the interplay between QM and gravitation [38–41]. These efforts seek to determine whether gravitational effects can induce measurable deviations from standard quantum predictions at scales within experimental reach.

2.2 Gravitational Decoherence

An alternative approach to quantizing gravity is the idea of retaining a classical description of the gravitational field while modifying quantum theory itself. In this framework, rather than directly quantizing space-time, one introduces modifications to the standard quantum dynamics to accommodate general relativity. As Penrose phrased it, the goal of such strategies is to achieve a "gravitization of QM" [42], rather than a quantization of gravity. A notable motivation for this perspective is that departures from conventional quantum mechanics have been proposed independently of gravitational considerations, primarily to address the measurement problem [7, 14–17].

One of the key concepts emerging in this context is gravitational decoherence [43–46]. If gravity is a quantum field, then gravitational degrees of freedom may act as an environment, introducing fluctuations that decohere quantum states. This is analogous to standard open quantum systems, where interactions with the environment cause the system to lose its quantum coherence. In this picture, tracing over the quantum gravitational field leads to a modified, non-unitary evolution for the system, thus effectively acting as a source of decoherence. Alternatively, if gravity is fundamentally classical, several of the proposed models expect the existance of stochastic fluctuations in the spacetime metric, which also induce decoherence [47–49]. Some approaches even interpret gravitational interactions as a form of continuous measurement, where classical gravity effectively "monitors" the quantum system and induces a collapse-like behaviour [39].

In the following Subsections, we present specific realizations of this ideas, including the Károlyházy model [50–52], the Schrödinger–Newton equation [32], the Kafri-Taylor- Milburn (KTM) approach [53], the Tilloy–Diósi (TD) model [54], and the semi-classical schemes discussed by Oppenheimer and collaborators [55], all of which aim to maintain a classical gravitational field while allowing for consistent quantum dynamics. The list also includes the DP model [25–27, 42, 56], already introduced above in Chapter 1, and that will be further discussed in Chapter 4.

2.2.1 The Károlyházy model

In the present Subsection, we introduce only the essential elements of the model, while a detailed and comprehensive analysis will be presented in Chapter 3.

Károlyházy's model is based on the assumption that spacetime is fuzzy below a specific scale, and this fuzziness causes a lack of quantum coherence in space (and time) for material systems, which is stronger the larger the systems.

The key idea is that lengths and times cannot be measured with arbitrary precision, given that measuring devices are made of atoms and therefore are ultimately quantum and must obey the Heisenberg uncertainty principle. Thus, there is a fundamental uncertainty in the structure of spacetime. By using the uncertainty principle and some basic (albeit a bit heuristic) arguments, he arrives at the following relation for the best precision with which a length s can be measured

$$\Delta s^3 = l_p^2 s, \tag{2.1}$$

with $l_p = \sqrt{\hbar G/c^3}$ being the Planck length. So spacetime is undetermined beyond some scale, according to Károlyházy. The model assumes the validity of the Schrödinger equation, supplemented by a random gravitational potential with a specific correlation function. As such, although often quoted as a collapse model, it is not: here, the superposition principle remains valid and macroscopic superpositions are still solutions of the equations of motion. The model does not represent a resolution of the quantum measurement problem. It is, however, interesting since it shows that when quantum systems couple to gravity, even if gravity is treated classically, intrinsic fluctuations can exist, which cause decoherence, preventing full control of the quantum state of the system.

2.2.2 The Schrödinger–Newton equation

The Schrödinger–Newton (SN) equation was first introduced in [32]. It is a non-linear modification of the Schrödinger equation that incorporates a non-linear potential, as the Newtonian gravitational potential, and uses $|\psi^2|$ as mass density. The inclusion of a self-interaction term represents a fundamental alteration of quantum mechanics. The SN equation can be derived from semiclassical gravity in the weak coupling and non relativistic regimes [57, 58].

In semiclassical gravity, the dynamical equations governing spacetime are based on the Einstein equations of general relativity,

$$G_{\mu\nu} = \frac{8\pi G}{c^4} T_{\mu\nu}, \tag{2.2}$$

which relate the geometry of spacetime, encoded in the Einstein tensor $G_{\mu\nu}$, to its matter and energy content, described by the energy-momentum tensor $T_{\mu\nu}$. The Einstein tensor is constructed from the spacetime metric and its derivatives and accounts for the local curvature of spacetime, while $T_{\mu\nu}$ acts as the source of the gravitational field.

Within the semiclassical framework, matter fields are treated quantum mechanically, whereas gravity remains classical. As a consequence, the energy-momentum tensor is promoted to a quantum operator $\hat{T}_{\mu\nu}$ acting on the Hilbert space of the matter fields. The coupling between quantum matter and classical geometry is implemented by replacing the classical source term with the expectation value of this operator in a given quantum state $|\psi\rangle$,

$$G_{\mu\nu} = \frac{8\pi G}{c^4} \langle\psi|\hat{T}_{\mu\nu}|\psi\rangle. \tag{2.3}$$

In this formulation, the spacetime geometry responds to the average distribution of energy and momentum associated with the quantum state of matter, while gravitational degrees of freedom are not quantized.

In the weak field limit, one can expand the metric around flat spacetime $g_{\mu\nu} = \eta_{\mu\nu} + h_{\mu\nu}$ with $|h_{\mu\nu}| \ll |\eta_{\mu\nu}|$; in the non-relativistic limit, the only relevant component of the metric is g_{00}. Then, Eq. (2.3) reduces to [59]

$$\nabla^2 h_{00} = -\frac{8\pi G}{c^4} \langle\psi|\hat{T}_{00}|\psi\rangle. \tag{2.4}$$

The interaction between gravity and matter is described by the Hamiltonian $\hat{H}_I = -\frac{1}{2}\int \mathrm{d}x h_{\mu\nu}\hat{T}^{\mu\nu}$. By considering only the relevant $'00'$ component, and given that $\hat{T}^{00} = \hat{\mu}c^2$ with the mass density $\hat{\mu} = \sum_j m_j \hat{\psi}_j^\dagger \hat{\psi}_j$, (the sum runs over the different kinds of particles composing the system, and $\hat{\psi}_j^\dagger \hat{\psi}_j$ is the number density operator for particles of type j), and using the solution of the Poisson Eq. (2.4), one gets

$$\hat{H}_I = -G \int \mathrm{d}\mathbf{x} \int \mathrm{d}\mathbf{x}' \, \frac{\langle\psi|\hat{\mu}(\mathbf{x}')|\psi\rangle}{|\mathbf{x}-\mathbf{x}'|} \, \hat{\mu}(\mathbf{x}). \tag{2.5}$$

When this potential is added into the Schrödinger equation, one obtains the SN equation, which for one particle is

$$i\hbar \frac{\mathrm{d}}{\mathrm{d}t}\psi_t(\mathbf{x},t) = \left[-\frac{\hbar^2}{2m}\nabla^2 - Gm^2 \int \mathrm{d}^3\mathbf{y} \, \frac{|\psi_t(\mathbf{y},t)|^2}{|\mathbf{x}-\mathbf{y}|}\right] \psi_t(\mathbf{x},t). \tag{2.6}$$

The second term on the right-hand side represents a Newtonian gravitational self-attraction between different parts of the wave function. For a free particle, this contribution counteracts the indefinite spreading of the wave function induced by the kinetic term. The two effects eventually balance, leading the wave function to asymptotically attain a finite width. While negligible for microscopic systems on typical timescales, the effect becomes increasingly significant for larger masses.

The SN equation is non-linear and deterministic, which raises a serious issue, since such a dynamics have been shown to permit faster-than-light signalling [18]. In the specific case of the SN equation, this was explicitly demonstrated in [59]. We will not delve into this topic further, as it lies beyond the scope of the present work, but the interested reader can find a detailed discussion in [59].

2.2.3 The KTM model

The model proposed by Kafri, Taylor, and Milburn (KTM) [53] is based on the idea of implementing Newtonian gravity through a hybrid classical-quantum dynamics based on a continuous measurement and feedback protocol. The model considers two masses m_1 and m_2, each confined in a harmonic potential with trapping frequencies, respectively ω_1 and ω_2. The two masses interact via the Newtonian gravitational potential. The distance d between the masses is supposed to be much larger than the spread of the position of the wave function of each particle, so the Newtonian potential can be approximated by a linear potential, leading to the effective one-dimensional Hamiltonian

$$\hat{H} = \hat{H}_0 + K\,\hat{x}_1\hat{x}_2, \qquad \hat{H}_0 = \sum_{j=1}^{2}\left(\frac{\hat{p}_j^2}{2m_j} + \tfrac{1}{2}m_j\omega_j^2\hat{x}_j^2\right), \tag{2.7}$$

where $\tilde{\omega}_j^2 = \omega_j^2 - K/m_j$ and $K = 2Gm_1m_2/d^3$.

The first assumption of the KTM model is that each particle undergoes a continuous measurement of its position [60]. The measurement records $r_j(t)$ are random variables with mean $\langle\hat{x}_j(t)\rangle$ and fluctuations proportional to white noises $w_j(t)$

$$r_j(t) = \langle\hat{x}_j(t)\rangle + \sqrt{\gamma_j}\,w_j(t), \tag{2.8}$$

where the parameters γ_j , which at this stage are arbitrary, control the information associated to the outcome of the continuous measurement. Next, the measurement records are used as a feedback to generate an hybrid classical-quantum (linearized) Newtonian interaction in place of the standard quantum interaction

$$K\,\hat{x}_1\hat{x}_2 \;\longrightarrow\; K\big(r_1(t)\,\hat{x}_2 + r_2(t)\,\hat{x}_1\big). \tag{2.9}$$

This is why one speaks of a continuous measurement and feedback protocol [60–62].

The continuous position measurement perturbs the dynamics of the two particles, leading to decoherence through measurement backaction and feedback-induced noise. In the framework introduced by KTM, decoherence is quantified by the noise terms appearing in the unconditional master equation, in particular by the coefficients of the double-commutator terms that govern momentum diffusion and spatial decoherence.

KTM showed that, for a fixed gravitational coupling strength K, the total decoherence rate arising from the combined effects of continuous measurement and classical feedback is minimized when the measurement strengths are chosen as $\gamma_j = 2K$. This choice optimally balances measurement backaction against feedback-induced noise, yielding the smallest possible additional decoherence compatible with reproducing the correct Newtonian interaction. As a result, the measurement strength is directly linked to the gravitational coupling. The corresponding evolution for the wave function is given by [63]

$$\begin{aligned}
\mathrm{d}|\psi(t)\rangle = \Bigg\{ & -\frac{i}{\hbar}\hat{H}_0\,\mathrm{d}t - \sum_{\substack{j,k=1\\ j\neq k}}^{2}\left[\frac{i}{\hbar}K\hat{x}_j r_k(t) + \frac{K\hat{x}_j^2}{4\hbar}\right]\mathrm{d}t \\
& + \sum_{j=1}^{2}\left[-\frac{K}{4\hbar}\left(\hat{x}_j - \langle\hat{x}_j(t)\rangle\right)^2\mathrm{d}t + \sqrt{\frac{K}{2\hbar}}\left(\hat{x}_j - \langle\hat{x}_j(t)\rangle\right)\mathrm{d}W_j(t)\right] \\
& - \sum_{\substack{j,k=1\\ j\neq k}}^{2}\frac{i}{2\hbar}K\hat{x}_j\left(\hat{x}_k - \langle\hat{x}_k(t)\rangle\right)\mathrm{d}t\Bigg\}|\psi(t)\rangle,
\end{aligned} \tag{2.10}$$

where the first term on the right-hand-side is the standard Hamiltonian term $\hat{H}_0$ of Eq. (2.7) (without the gravitational part), the second term corresponds to the feedback contribution, the third and fourth term to the continuous measurement,

while the last term is the Itô term arising from their combined effect. As one can see, this is a stochastic and highly non-linear equation, where the gravitational interaction can barely be recognized. Yet, the corresponding master equation, when an average over the noise is taken, is

$$\frac{\mathrm{d}\hat{\rho}(t)}{\mathrm{d}t} = -\frac{i}{\hbar}\big[\hat{H}_0 + K\hat{x}_1\hat{x}_2,\, \hat{\rho}(t)\big] - \frac{K}{2\hbar}\sum_{j=1}^{2}\big[\hat{x}_j,\, [\hat{x}_j,\, \hat{\rho}(t)]\big]. \tag{2.11}$$

This is a Lindblad equation in which the linearized gravitational interaction appears in the unitary part of the evolution as a conventional quantum interaction. Consequently, while the wave function dynamics follows a hybrid classical–quantum evolution, the master equation describes a fully quantum evolution since the classical and non-linear contributions are averaged out. The trade-off is the presence of a Lindblad term, which accounts for position decoherence.

2.2.4 The Tilloy–Diósi model

The Tilloy-Diósi (TD) model [54] has several connections to the models introduced in the previous Subsections: it was proposed as a solution to the faster-than-light signalling problem in semi-classical gravity discussed in Subsection 2.2.2. It introduces a feedback mechanism similar to that used in the KTM model presented in Subsection 2.2.3. In an appropriate limit, its master equation reduces to that of the DP model of Subsection 1.5.4.

The main issue with the non-linear SN Eq. (2.6) is that it is fully deterministic. To address this, Tilloy and Diósi introduce stochastic terms into the dynamics. They replace the gravitational source $\langle\psi|\hat{\rho}(\mathbf{r})|\psi\rangle$ with $\langle\psi|\hat{\rho}(\mathbf{r})|\psi\rangle + \int \mathrm{d}\mathbf{s}\,\gamma^{-1}(\mathbf{r}-\mathbf{s})\,\delta\rho_t(\mathbf{s})$, where γ^{-1} is the inverse of the kernel γ, satisfying $\int \mathrm{d}\mathbf{s}\,\gamma(\mathbf{r}-\mathbf{s})\,\gamma^{-1}(\mathbf{s}-\mathbf{r}') = \delta(\mathbf{r}-\mathbf{r}')$, and $\delta\rho_t(\mathbf{s})$ is a stochastic fluctuation resulting from a continuous measurement of the mass density at spacetime point $(t,\mathbf{s})$, with zero mean and correlation $\mathbb{E}[\delta\rho_t(\mathbf{s})\,\delta\rho_{t'}(\mathbf{s}')] = \gamma(\mathbf{s}-\mathbf{s}')\,\delta(t-t')$. By using a similar continuous measurement and feedback mechanism as in the KTM model, now generalized to measurements at each spacetime point, they obtain a non-trivial stochastic non-linear evolution for the wave function $|\psi_t\rangle$, generalizing Eq. (2.10) to the full Newtonian potential [63]. Averaging over the noise then gives a Lindblad-type

master equation

$$\frac{\mathrm{d}\hat{\rho}(t)}{\mathrm{d}t} = -\frac{i}{\hbar}\big[\hat{H} + \hat{V}_{\mathrm{NEW}},\, \hat{\rho}(t)\big] - \int \mathrm{d}\mathbf{s}\, \mathrm{d}\mathbf{r}\, D(\mathbf{r}-\mathbf{s})\, \big[\hat{\rho}(\mathbf{s}),\, [\hat{\rho}(\mathbf{r}),\, \hat{\rho}(t)]\big], \tag{2.12}$$

where $\hat{V}_{\mathrm{NEW}}$ is the standard Newtonian potential and

$$D(\mathbf{r}-\mathbf{s}) = \frac{\gamma(\mathbf{r}-\mathbf{s})}{8\hbar^2} + \frac{G^2}{2}\int \mathrm{d}\mathbf{r}' \int \mathrm{d}\mathbf{s}'\, \frac{\gamma^{-1}(\mathbf{r}'-\mathbf{s}')}{|\mathbf{r}-\mathbf{r}'|\,|\mathbf{s}-\mathbf{s}'|}, \tag{2.13}$$

acts as the decoherence kernel. Following the same reasoning as in the KTM model, the function $\gamma(\mathbf{r}-\mathbf{s})$ can be chosen so as to minimize the total decoherence rate induced by the measurement–feedback scheme, quantified by the strength of the double-commutator term in the unconditional master equation, under the constraint that the effective interaction reproduces the Newtonian potential. This optimization leads to $\gamma(\mathbf{r}-\mathbf{s}) = 2\hbar G/|\mathbf{r}-\mathbf{s}|$. With this choice, the Lindblad term in Eq. (2.12) reduces to that of Eq. (1.29) in the DP model. Although the decoherence term is identical to that of the DP model, the TD model has the important advantage of naturally incorporating the Newtonian interaction, which in the DP model is introduced by hand into the Hamiltonian.

As a final remark, it is important to emphasize that, contrary to intuition, the TD model does not reduce to the KTM model in the linearized gravity limit, as shown in [63]. This difference arises due to the noise sources associated with the measurements having a fundamentally different structure in the two models: in the KTM model, the noises are attached to the particles, whereas in the TD model, there is a noise at every point in spacetime, independent of the particle positions. This broader perspective is necessary to properly account for the full gravitational potential, as discussed in [63].

2.2.5 Semiclassical Schemes in Oppenheim's Framework

In order to overcome the inconsistencies of the standard semi-classical Einstein equation

$$G_{\mu\nu} \;=\; \frac{8\pi G}{c^4}\,\langle \hat{T}_{\mu\nu}\rangle, \tag{2.14}$$

which leads to pathological predictions when quantum fluctuations are large [64], Oppenheim and collaborators constructed a general hybrid dynamics for

classical-quantum (CQ) systems [55]. The state of the composite system is described by a density operator $\hat{\rho}(\mathbf{z}, t)$, a positive operator on the Hilbert space depending on the classical phase–space coordinate $\mathbf{z} = (\mathbf{q}, \mathbf{p})$, normalized such that

$$\int \mathrm{d}\mathbf{z}\, \mathrm{tr}\, \hat{\rho}(\mathbf{z}, t) = 1. \tag{2.15}$$

The evolution is governed by a completely positive, trace-preserving master equation, which in its most general form (under the assumption of a joint Markovian dynamics) reads

$$\begin{aligned} \partial_t \hat{\rho}(\mathbf{z}, t) = &-i\big[\hat{H}(z), \hat{\rho}(\mathbf{z}, t)\big] + \lambda_{\alpha\beta}(z) \left(\hat{L}_\alpha \hat{\rho}(\mathbf{z}, t) \hat{L}_\beta^\dagger - \tfrac{1}{2}\{\hat{L}_\beta^\dagger \hat{L}_\alpha, \hat{\rho}(\mathbf{z}, t)\} \right) \\ &+ \int \mathrm{d}\mathbf{z}'\, W_{\alpha\beta}(\mathbf{z}|\mathbf{z}')\, \hat{L}_\alpha \hat{\rho}(\mathbf{z}', t) \hat{L}_\beta^\dagger - \tfrac{1}{2}\, W_{\alpha\beta}(\mathbf{z})\, \{\hat{L}_\beta^\dagger \hat{L}_\alpha, \hat{\rho}(\mathbf{z}, t)\}_+, \end{aligned} \tag{2.16}$$

where $\hat{L}_\alpha$ are Lindblad operators, $\lambda_{\alpha\beta}(\mathbf{z})$ and $W_{\alpha\beta}(\mathbf{z}|\mathbf{z}')$ are positive-semidefinite kernels ensuring complete positivity, and

$$W_{\alpha\beta}(\mathbf{z}) = \int \mathrm{d}\mathbf{z}' W_{\alpha\beta}(\mathbf{z}'|\mathbf{z})$$

encodes classical outflow rates. In particular, the coefficients $W_{\alpha\beta}(\mathbf{z}'|\mathbf{z})$ represent the transition rates from the classical state $\mathbf{z}$ to $\mathbf{z}'$, while $W_{\alpha\beta}(\mathbf{z})$ quantifies the total outflow rate, i.e., the probability per unit time for the system to leave configuration $\mathbf{z}$ towards any other, thereby ensuring probability conservation and the complete positivity of the dynamics.

Moreover, Oppenheim and collaborators analyse the standard non-relativistic limit using the Wigner representation of a single quantum system [65]. For a state $\hat{\rho}$, the Wigner function is defined as

$$W(q, p) = \mathrm{tr}\left[\hat{A}_{q,p}\, \hat{\rho}\right], \tag{2.17}$$

where the Wigner kernel can be compactly written as

$$\hat{A}_{q,p} = \frac{1}{2\pi\hbar} \int \mathrm{d}y\, e^{-ipy/\hbar}\, |q + y/2\rangle\langle q - y/2|\,, \tag{2.18}$$

and is standard in phase-space quantum mechanics [66, 67]. Although $W(q, p)$ is a quasi-probability distribution that can take negative values, its dynamics reduces to a classical form in the $\hbar \to 0$ limit. Expanding the unitary evolution to lowest

order in $\hbar$ yields the Liouville equation

$$\frac{\partial W}{\partial t} = \{H, W\}, \tag{2.19}$$

where $\{\cdot, \cdot\}$ denotes the Poisson bracket and H is the classical Hamiltonian function of $(\mathbf{q}, \mathbf{p})$, distinct from the quantum Hamiltonian $\hat{H}(\mathbf{z})$ in the hybrid master equation. This equation governs the evolution of classical probability distributions in phase space and represents the emergence of classical mechanics from quantum theory in the $\hbar \to 0$ limit. While consistent for a single system, the authors show that this procedure fails for subsystems, where entanglement with other degrees of freedom prevents a fully classical description.

Such effective classical limits can also be interpreted within the broader framework of measurement and feedback dynamics. In this picture, classicality emerges since the subsystem is continuously "monitored" by its environment, with the resulting back-action providing the feedback that stabilises a classical trajectory. This perspective connects the present analysis with other hybrid classical-quantum models, including the continuous measurement approaches developed by Tilloy and Diósi [54].

Chapter 3

The Károlyházy model

This chapter is based on the results presented in L. Figurato et al., *New Journal of Physics*, **26** (1), 013001 (2024) [68], which elaborates the data that were available until 2024.

3.1 Introduction

One of the first proposals for gravitational decoherence was formulated by Károlyházy [50]. He suggested that there is a fundamental limitation in the precision with which a length can be measured using a quantum probe. He interpreted this limit as arising due to what he called, with a bit of humor, spacetime haziness, i.e. stochastic fluctuations of the spacetime metric, which prevent measurements from being too sharply defined. A first consequence of these fluctuations is of course decoherence in space, which has been well studied in the literature [50–52, 69]. Another, less-known, consequence of spacetime haziness is that charged particles, being accelerated by the metric fluctuations, emit radiation. Diósi and Lukács computed the expected photon emission rate for the Károlyházy model, showing that it is incompatible with observations [70, 71]. The model was thus ruled out. The same effect was used to bound the parameters of models of spontaneous wave function collapse [21, 72–77] , and led to the exclusion of some of them [78].

Károlyházy's original paper resorted to an additional ingredient, besides spacetime fluctuations: it assumed that these fluctuations have the form of gravitational waves. This assumption constrains the correlation function of the fluctuations, which is ultimately responsible for predicting a large photon emission rate from matter, which in turn is excluded by experimental evidence. Yet, gravitational waves are not necessary to implement Károlyházy's goal of explaining why there is a fundamental limitation to position measurements; spacetime fluctuations alone, with a more general correlation function, suffice.

In this chapter we explore the possibility of generalizing Károlyházy's model by considering a larger class of correlation functions for the gravitational fluctuations, showing that compatibility with current experimental evidence can be restored.

3.2 A brief review of the Károlyházy model

The genesis of Károlyházy's model [50, 51] lies in the attempt to answer the following question: with what precision can a time-like length $s = cT$ in flat spacetime, where T is the proper time in the Minkowski metric, be measured using a quantum probe obeying the uncertainty principle? By combining the uncertainty principle together with the requirement that the mass of the system is small enough to guarantee that its Schwarzschild radius R_s is smaller than the uncertainty in the position measurements Δx, Károlyházy provided an argument as to why there is a minimum uncertainty Δs in the inferred length s. More precisely [50], he imagined (Figure 3.1) a coordinate system in flat space and tried to "materialize" a segment of its temporal axis by the narrowest possible tube formed by a standing wave function. Let the width of the wave function be Δx_0 at the bottom of the segment. From the uncertainty principle we have $\Delta x_0 M \Delta v = \hbar$ where Δv is the velocity spread and M is the mass concentrated within the wave function, the corresponding Δx at the top of the segment will be $\Delta x = \Delta v T = [\hbar/(Mc\Delta x_0)]cT$, where cT is the length of the segment. He regarded Δx_0 and Δx as the measures of the indefiniteness of the length of the segment. The minimum total uncertainty for a given $cT = s$ is obtained by setting $\Delta x = \Delta x_0$. This uncertainty diminishes with increasing mass. The value of M is ultimately limited by the requirement that its Schwarzschild radius $R_s = 2GM/c^2$ should not be greater than Δx, and M is expressed from $\Delta x \approx (G/c^2)M$, where G is the gravitational constant.

Using these ingredients, we can write the following relation

$$\Delta x = \frac{\hbar T c}{Mc\Delta x_0}, \tag{3.1}$$

and since the minimum total uncertainty for a given $cT = s$ is obtained by setting $\Delta x = \Delta x_0$, we have

$$\Delta x^2 = \frac{\hbar T c}{Mc}. \tag{3.2}$$

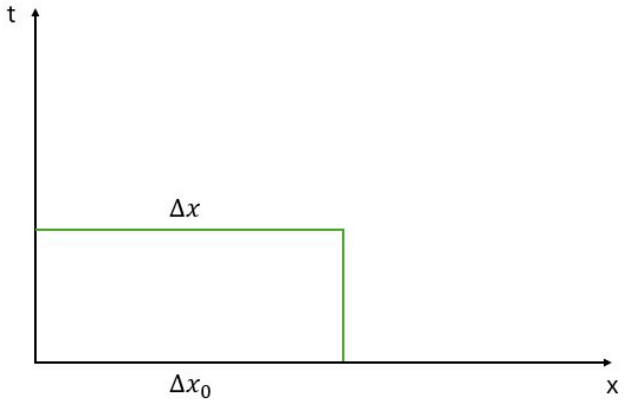

Figure 3.1: The coordinate system in flat space imagined by Károlyházy in which he tried to "materialize" a segment of its temporal axis by the narrowest possible tube formed by a standing wave function. Let the width of the wave function be Δx_0 at the bottom of the segment. From the uncertainty principle we have $\Delta x_0 M \Delta v = \hbar$ where Δv is the velocity spread and M is the mass concentrated within the wave function, the corresponding Δx at the top of the segment will be $\Delta x = \Delta v T = (\hbar / M c \Delta x_0) cT$, where cT is the length of the segment. He regarded Δx_0 and Δx as the measures of the indefiniteness of the length of the segment. The minimum total uncertainty for a given $cT = s$ is obtained by setting $\Delta x = \Delta x_0$.

For the condition on the Schwarzschild radius on M, we have that

$$M = \frac{\Delta x c^2}{G}, \tag{3.3}$$

from which

$$\Delta x^3 = \frac{\hbar G T c}{c^3}. \tag{3.4}$$

Now we have to make it clear that for Károlyházy, the wave function evolves only in time and not in space since he considers $\Delta s = c\Delta t$, which holds only under this assumption. So, given this condition, we can replace Δx with Δs, which leads to

$$\Delta s^3 = \frac{\hbar G}{c^3} s, \tag{3.5}$$

from which we finally obtain for the minimum Δs the relation [1]

$$\Delta s^3 = l_p^2 s, \tag{3.6}$$

[1] There is a typo in the original work of Károlyházy [50] which, however, it does not propagate through the rest of the text: in his Eq. (3.1) the power of s is 3/2 while the correct power is 2/3, required for having consistent dimensions on both sides of the equation.

with $l_p = \sqrt{\hbar G/c^3}$ being the Planck length [50]. Károlyházy accounted for this uncertainty by assuming that spacetime fluctuates around the flat Minkowski metric $\eta_{\mu\nu}$. The total metric $g_{\mu\nu}$ is then given by $(g_{\mu\nu})_\beta(\boldsymbol{x}, t) = \eta_{\mu\nu}(\boldsymbol{x}, t) + (h_{\mu\nu})_\beta(\boldsymbol{x}, t)$, where $\eta_{\mu\nu}(\boldsymbol{x}, t)$ is the flat Minkowski metric and $(h_{\mu\nu})_\beta(\boldsymbol{x}, t)$ is the ensemble of fluctuating metrics with β labelling the different realizations of the fluctuations. Then, the proper length s between two fixed points in space is defined as the average of the lengths s_β corresponding to the different realizations of the fluctuations. Their average is

$$s = \mathbb{E}[s_\beta] = cT, \tag{3.7}$$

where $\mathbb{E}[...]$ denotes the average over the stochastic metric and the uncertainty Δs on this length is given by

$$\Delta s = \sqrt{\mathbb{E}(s_\beta - s)^2}, \tag{3.8}$$

The relation in Eq. (3.6) clearly limits the kind of possible stochastic metrics.

Károlyházy's analysis proceeds by considering non-relativistic dynamics and weak gravitational fields. It implies that only the component g_{00} of the metric is relevant for the dynamics, and that the fluctuations around the Minkowski metric can be written as

$$(g_{00})_\beta(\boldsymbol{x}, t) = 1 + \gamma_\beta(\boldsymbol{x}, t), \tag{3.9}$$

where we introduced $\gamma_\beta(\boldsymbol{x}, t) := (h_{00})_\beta(\boldsymbol{x}, t)$, which is the ensemble of fluctuating metrics (the temporal gravitational perturbation) with β labelling the different realizations of the fluctuations, and it measures how much the g_{00} component of the metric deviates from the flat (Minkowskian) value. For each realization of the stochastic metric β, the line element is given by

$$s_\beta = \int_0^T \sqrt{(g_{00})_\beta} c\mathrm{d}t = \int_0^T \sqrt{1 + \gamma_\beta(\boldsymbol{x}, t)} c\mathrm{d}t \simeq c \int_0^T \Big(1 + \frac{1}{2}\gamma_\beta(\boldsymbol{x}, t)\Big)\mathrm{d}t. \tag{3.10}$$

In order to obtain Eq. (3.7), it follows that $\mathbb{E}[\gamma_\beta(\boldsymbol{x}, t)] = 0$. Moreover, when the latter expression is replaced in Eq. (3.8), one gets

$$\Delta s^2 = \frac{c^2}{4}\mathbb{E}\Big(\int_0^T \gamma_\beta(\boldsymbol{x}, t)\mathrm{d}t\Big)^2, \tag{3.11}$$

and when imposing the constraint derived by Károlyházy in Eq. (3.6), we have

$$\Delta s^2 = l_p^{4/3} s^{2/3}. \tag{3.12}$$

By comparing the latter two expressions, we obtain the relation

$$\frac{c^2}{4}\mathbb{E}\Big(\int_0^T \gamma_\beta(\boldsymbol{x},t)\mathrm{d}t\Big)^2 = l_p^{4/3}s^{2/3}. \tag{3.13}$$

Note that in Eq. (3.11) one considers the correlation functions at the same point in space, i.e. $\boldsymbol{x} = \boldsymbol{x}'$ because Károlyházy defines the proper length as $s = cT$, hence assuming that the probe is not moving in space [50, 52].

Károlyházy assumed that γ_β satisfies the wave equation

$$\frac{1}{c^2}\frac{\partial^2\gamma_\beta(\boldsymbol{x},t)}{\partial t^2} - \nabla_x^2\gamma_\beta(\boldsymbol{x},t) = 0. \tag{3.14}$$

This implies that the Fourier expansion of the γ_β is of the form

$$\gamma_\beta(\boldsymbol{x},t) = \frac{1}{\sqrt{l^3}}\sum_{\boldsymbol{k}}\Big[c_\beta(\boldsymbol{k})e^{i(\boldsymbol{k}\cdot\boldsymbol{x}-\omega_{\boldsymbol{k}}t)} + c_\beta^*(\boldsymbol{k})e^{-i(\boldsymbol{k}\cdot\boldsymbol{x}-\omega_{\boldsymbol{k}}t)}\Big], \tag{3.15}$$

with $\omega_{\boldsymbol{k}} = |\boldsymbol{k}|c$, and $c_\beta(\boldsymbol{k}), c_\beta^*(\boldsymbol{k})$ are coefficients. Here, in order to work with normalized plane waves of discrete momentum k, we confined the system in a box with side l, which we will later take to infinity. Károlyházy further assumed that the different modes are independent and that the correlation depends only by a function $F(k)$ of the modulus of $k = |\boldsymbol{k}|$ of the wave vector, namely

$$\mathbb{E}[c_\beta(\boldsymbol{k})c_\beta^*(\boldsymbol{k'})] = \delta_{\boldsymbol{k},\boldsymbol{k'}}F(k), \tag{3.16}$$

where the correlations of the coefficients are given by [79]

$$\langle c_\beta(\boldsymbol{k})\rangle = 0, \qquad \langle c_\beta^2(\boldsymbol{k})\rangle = 0, \qquad \langle c_\beta(\boldsymbol{k})c_\beta^*(\boldsymbol{k})\rangle = \delta_{\boldsymbol{k},\boldsymbol{k'}}\left(F(k)\right)^2. \tag{3.17}$$

At this point, we must make an important clarification: Károlyházy suggested that the model should be considered meaningless for distances smaller than a cutoff $\lambda_c = 10^{-15}$ m [50]. This seems reasonable considering that the model was derived in the non-relativistic regime; we would otherwise belong to a regime in which relativistic effects would come into play. Given this caveat, by replacing the Fourier expansion Eq. (3.15) in Eq. (3.11), we obtain

$$\Delta s^2 = \frac{c^2}{4}\,\mathbb{E}\left[\left(\int_0^T \frac{1}{\sqrt{l^3}}\sum_{\boldsymbol{k}}\left(c_\beta(\boldsymbol{k})\,e^{i(\boldsymbol{k}\cdot\boldsymbol{x}-\omega_{\boldsymbol{k}}t)} + c_\beta^*(\boldsymbol{k})\,e^{-i(\boldsymbol{k}\cdot\boldsymbol{x}-\omega_{\boldsymbol{k}}t)}\right)dt\right)^2\right]. \tag{3.18}$$

Using Eq. (3.16) with the correlations in Eq. (3.17) and taking the continuum limit $l \to \infty$, so by applying the box normalization $1/l^3 \sum_{\boldsymbol{k}} \to 1/(2\pi)^3 \int \mathrm{d}\boldsymbol{k}$, it is then shown that in order to recover the bound in Eq. (3.6), the function $F(k)$ must be[2]

$$F(k) = \frac{8\pi^2}{3\Gamma(\frac{1}{3})} \, l_p^{4/3} k^{-5/3}. \tag{3.19}$$

This cutoff implies that the power-law spectrum in Eq. (3.19) is not meant to hold for arbitrarily large wave vectors, but only within its domain of validity $k \leq 2\pi/\lambda_c$, with $F(k)$ vanishing for higher momenta. The cutoff is introduced to regularize the integrals appearing in the model, which would otherwise diverge due to the contribution of arbitrarily large wave vectors.

To summarize, in Karolyhazy's model, matter is subject to spacetime fluctuations with zero mean, and the correlation function is given by Eq. (3.16), with $F(k)$ given by Eq. (3.19). As we will see, these fluctuation induce decoherence in position, as described by Eq. (3.34) below. Models predicting position decoherence are hard to test with interferometric experiments, but a possibility is given by non interferometric experiments as those focused on the spontaneous radiation emission and energy violation [77], as we will analyse in the Section 3.4.

3.3 Semiclassical derivation of the emission rate

We present the derivation of the formula for the radiation emission rate for a free particle following the calculation performed by Diósi and Lukács in [70]. Many of the equations introduced here will serve as a basis for the analysis that will be carried out in the next sub-sections. This derivation is based on a semiclassical approach that, whenever used in connection to spontaneous wavefunction collapse models (which also impose a stochastic fluctuation), proved to be perfectly consistent with the fully quantum mechanical calculation [75, 78, 80].

The starting point of the derivation of the formula for the radiation emission rate for a free particle is the Larmor formula relating the total emitted power P to the acceleration a of a charged particle. For a time average over the stochastic process, a^2 is to be interpreted as $\mathbb{E}[a^2]$, with $\mathbb{E}[...]$ being the stochastic expectation. As just said, the Larmor formula relating the total emitted power P to the acceleration a

[2]Compared to the article of Károlyházy [52], we have an extra multiplicative factor $\frac{8\pi^2}{3\Gamma(\frac{1}{3})}$, which is necessary to satisfy the constraint given in Eq. (3.6) with the correct constants.

of a charge is given by

$$P(t,\boldsymbol{x}) = \frac{e^2}{6\pi\epsilon_0 c^3}\mathbb{E}[a^2(\boldsymbol{x},t)], \tag{3.20}$$

where $a(\boldsymbol{x},t)$ is the modulus of the acceleration at time t of a particle with charge e, located in $\boldsymbol{x}$. We are interested in computing the radiation emission rate $\mathrm{d}\Gamma(t)/\mathrm{d}\omega_{\boldsymbol{k}}$, which gives the number of photons that are emitted per unit of time at a given frequency $\omega_{\boldsymbol{k}}$. The total emitted power is related to the radiation emission rate by the relation

$$P(t) = \int_0^{+\infty} \mathrm{d}\omega_{\boldsymbol{k}}\, \hbar\omega_{\boldsymbol{k}} \frac{\mathrm{d}\Gamma(t)}{\mathrm{d}\omega_{\boldsymbol{k}}}. \tag{3.21}$$

In order to find the emission rate it is convenient to take the Fourier transform of the acceleration

$$\boldsymbol{a}(\boldsymbol{x},t) = \frac{1}{2\pi}\int_{-\infty}^{+\infty} \mathrm{d}\omega\; e^{i\omega t}\boldsymbol{a}(\boldsymbol{x},\omega), \tag{3.22}$$

and insert it into the total radiation power in Eq. (3.20), obtaining

$$P(t,\boldsymbol{x}) = \frac{e^2}{6\pi\epsilon_0 c^3}\frac{1}{(2\pi)^2}\sum_{j=1}^{3}\int_{-\infty}^{+\infty}\mathrm{d}\nu\int_{-\infty}^{+\infty}\mathrm{d}\omega\; e^{i(\nu+\omega)t}\,\mathbb{E}[a_j(\boldsymbol{x},\omega)a_j(\boldsymbol{x},\nu)]. \tag{3.23}$$

We now specialize the calculation to the Károlyházy model. The effect of γ_β perturbing the metric tensor component g_{00} is equivalent to introducing a random potential [49, 70, 79]

$$V_\beta(\boldsymbol{x},t) = \frac{1}{2}mc^2\gamma_\beta(\boldsymbol{x},t), \tag{3.24}$$

into the Schrödinger equation. The corresponding acceleration is

$$\boldsymbol{a}(\boldsymbol{x},t) = -\frac{1}{2}c^2\nabla_x\gamma_\beta(\boldsymbol{x},t), \tag{3.25}$$

and its Fourier transform is (see Eq. (3.15))

$$\boldsymbol{a}(\boldsymbol{x},\omega) = -\frac{c^2\pi}{\sqrt{l^3}}\sum_{\boldsymbol{k}} i\boldsymbol{k}\left[c(\boldsymbol{k})e^{i\boldsymbol{k}\cdot\boldsymbol{x}}\delta(\omega+\omega_{\boldsymbol{k}}) - c^*(\boldsymbol{k})e^{-i\boldsymbol{k}\cdot\boldsymbol{x}}\delta(\omega-\omega_{\boldsymbol{k}})\right]. \tag{3.26}$$

By using Eq. (3.16), the integrand in Eq. (3.23) is porportional to

$$\mathbb{E}[a_j(\boldsymbol{x},\omega)a_j(\boldsymbol{x},\nu)] = \frac{c^4\pi^2}{l^3}\left[\sum_{\boldsymbol{k}} k_j^2 F(k)\left[\delta(\omega+\omega_{\boldsymbol{k}})\delta(\nu-\omega_{\boldsymbol{k}}) + \delta(\omega-\omega_{\boldsymbol{k}})\delta(\nu+\omega_{\boldsymbol{k}})\right]\right]. \tag{3.27}$$

By inserting the last equality in Eq. (3.23), integrating the Dirac-δ functions and taking the limit l to ∞, one arrives at the following result

$$P(t) = \frac{e^2}{3\pi\epsilon_0 c^3}\frac{1}{(2\pi)^5}\int_{-\infty}^{+\infty} \mathrm{d}\boldsymbol{k}\; c^4\pi^2 k^2 F(k) = \frac{e^2 c\, l_p^{4/3}}{9\pi\epsilon_0\Gamma\left(\frac{1}{3}\right)}\int_0^{\frac{2\pi}{\lambda_c}} \mathrm{d}k\; k^{7/3}, \tag{3.28}$$

where in the second line we used Eq. (3.19) and integrated over the angular variables. The emission rate can be found by comparing this equation to Eq. (3.21), imposing the cutoff mentioned before $k \leq 2\pi/\lambda_c$ and expressing $\omega = kc$. This leads to

$$\frac{\mathrm{d}\Gamma(t)}{\mathrm{d}\omega_{\boldsymbol{k}}} = \frac{e^2 l_p^{4/3}}{9\pi\epsilon_0\Gamma\left(\frac{1}{3}\right)c^{7/3}\hbar}\omega_{\boldsymbol{k}}^{4/3}. \tag{3.29}$$

As already discussed in [70], the Károlyházy model predicts a large amount of radiation emitted due to the spacetime fluctuations, in disagreement with observations. To see this, we compare the predicted emission rate to the data in [76] used to set the strongest bounds on the Continuous Spontaneous Localization (CSL) [9, 23, 81, 82] and Diósi-Penrose (DP) [25–27] parameters. A direct comparison of Eq. (3.29) with the data in [76] requires a detailed statistical analysis that goes beyond the purpose of this thesis. Instead, we set an upper bound on the experimentally measured emission rate by taking the formula for the emission in the CSL model considered in Eq. (2) of [76], namely

$$\frac{\mathrm{d}\Gamma(E)}{\mathrm{d}E} = A_f \times \frac{\hbar\lambda}{4\pi^2\epsilon_0 m_0^2 c^3 r_C^2 E}, \tag{3.30}$$

where $A_f = N_{\mathrm{Ge}}N_{\mathrm{e}}e^2$ is a charge-dependent amplification factor, and apply it to the case we are considering for a single particle with charge e.[3] As already said in Chapter 1, the CSL model has two phenomenological parameters: the collapse rate λ, which sets the strength of the collapse, and the correlation length r_C, which set the spatial scale of the collapse. The radiation emission rate depends on the ratio λ/r_C^2, which is bounded to $\lambda/r_C^2 \leq 5.39\times10^{-1}\mathrm{s}^{-1}\mathrm{m}^{-2}$, for details see [76].

[3] We want to stress that there is no exact mapping between CSL and Károlyházy. Both models induce small stochastic accelerations of charged particles, which lead to electromagnetic emission scaling similarly with the particle charge and acceleration, allowing an order-of-magnitude comparison with the X-ray emission data in [76] that set the strongest bounds on CSL and DP parameters. So what is usually done is to treat the Károlyházy stochastic acceleration as "equivalent" to a CSL-type stochastic process and use the same formula to estimate the radiation.

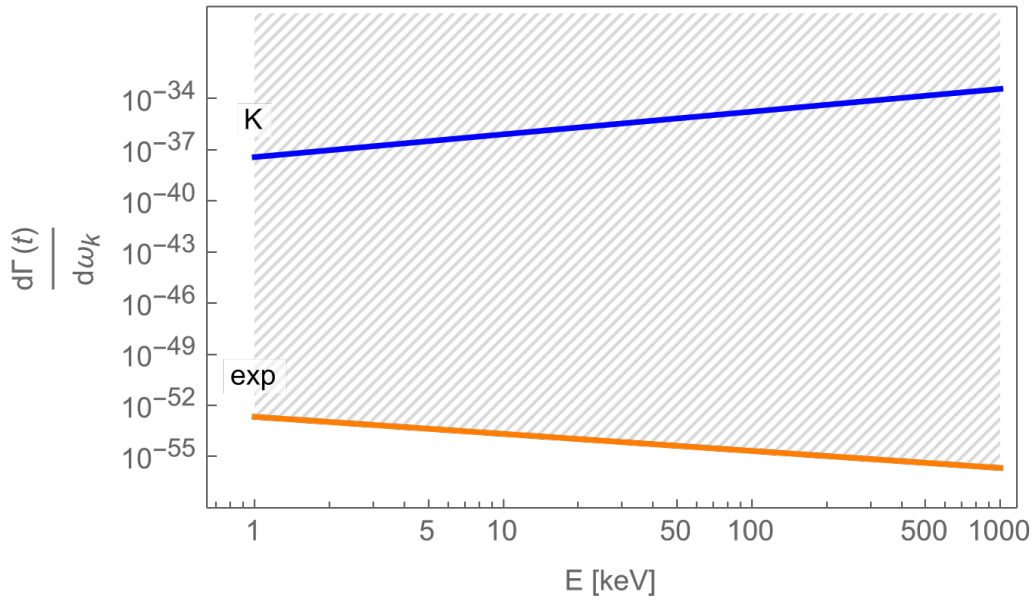

Figure 3.2: Comparison between the radiation emission rate predicted by Károlyházy's model in Eq. (3.29) (blue line) and the upper bound on the rate inferred by the experimental data shown in Eq. (3.31) (orange line).The shaded area indicates the values of radiation emission rate that are excluded by the experiment in [76].

We take as values for the CSL parameters those given by this bound. Then we get

$$\frac{\mathrm{d}\Gamma(t)}{\mathrm{d}\omega_{\boldsymbol{k}}}\Big|_{\mathrm{exp}} \leq \frac{e^2\hbar\lambda}{4\pi^2\epsilon_0 m_0^2 c^3 r_C^2 \omega_{\boldsymbol{k}}} = \frac{5.09\times 10^{-35}\ \mathrm{s}^{-1}}{\omega_{\boldsymbol{k}}}. \tag{3.31}$$

In Figure 3.2 we compare the radiation emission rate from a particle of charge e, as predicted by the Károlyházy model, with the experimentally observed rate found using Eq. (3.31). Károlyházy's predictions are more than 13 orders of magnitude larger than the observed radiation rate.

3.4 Generalization and predictions

As discussed in the previous Section, the Károlyházy model predicts a large amount of radiation emitted, which is in contrast with observations. At the core of Károlyházy's idea lies the assumption that the stochastic metric should reproduce Eq. (3.6). However, in formulating his model, Károlyházy further assumed that the metric fluctuations should satisfy a wave equation and therefore be of the form given in Eq. (3.15). This leads to a correlation function for the fluctuations γ_β reading,

$$f(\boldsymbol{x},\boldsymbol{x}',t,t') = \mathbb{E}[\gamma_\beta(\boldsymbol{x},t)\gamma_\beta(\boldsymbol{x}',t')], \tag{3.32}$$

that is highly non-Markovian and where the spatial and temporal dependencies are not factorized [49], see Eq. (3.9).

One might wonder if, by considering a factorised correlation function in the Károlyházy model, the predicted radiation emission rate might be smaller. We will answer this question by tackling the problem in a more general way: we will look for the general form of the correlation function, which still satisfies the constraint in Eq. (3.13), and then we will consider the experimental consequences. In particular, we will relax the hypothesis that the wave equation in Eq. (3.14) must be fulfilled.

By relaxing the expansion in plane waves, we assume only that the correlation function of the fluctuations $\gamma_\beta(\boldsymbol{x}, t)$ be translational covariant in space and time and symmetric under time reversal, i.e.

$$f(\boldsymbol{x}, \boldsymbol{x}', t, t') = g(\boldsymbol{x} - \boldsymbol{x}', 0, t - t', 0). \tag{3.33}$$

We start from the master equation [79]

$$\begin{aligned}\frac{\mathrm{d}\hat{\rho}(t)}{\mathrm{d}t} = &-\frac{i}{\hbar}\left[\hat{H}, \hat{\rho}(t)\right] - \left(\frac{c^2}{2\hbar}\right)^2 \int_{-\infty}^{+\infty} \mathrm{d}\boldsymbol{x} \int_{-\infty}^{+\infty} \mathrm{d}\boldsymbol{x}' \int_0^t \mathrm{d}t' g(\boldsymbol{x} - \boldsymbol{x}', t - t') \times \\ &\times \left[\hat{\rho}(\boldsymbol{x}), \left[e^{\frac{i}{\hbar}\hat{H}(t'-t)}\hat{\mu}(\boldsymbol{x}')e^{-\frac{i}{\hbar}\hat{H}(t'-t)}, \hat{\mu}(t)\right]\right],\end{aligned} \tag{3.34}$$

where we relaxed the requirement that the correlation function must depend on $(t - t')$ and we considered a not necessarily point-like mass density for the particles, namely the corresponding mass density operator is

$$\hat{\mu}(\boldsymbol{x}) = \sum_i m_i \mu(\boldsymbol{x} - \hat{\boldsymbol{q}}_i), \tag{3.35}$$

with m_i being the mass of the i-th particle and $\mu(\boldsymbol{x} - \hat{\boldsymbol{q}}_i)$ describing the shape of the mass density.

As mentioned earlier, we want to consider factorized correlation functions to test whether the predicted radiation emission rate might be lower. We look for the general form of correlation function, which satisfies the constraint in Eq. (3.13), but contemporarily relax the constraint in Eq. (3.14) must be fulfilled.

By using Eq. (3.11) one gets the condition

$$\int_0^T \mathrm{d}t' \int_0^T \mathrm{d}t\; g(0, t - t') = 4\Big(\frac{l_p}{c}\Big)^{\frac{4}{3}} T^{\frac{2}{3}}. \tag{3.36}$$

We rewrite its left-hand side by performing the change of variables $\tau = t - t'$ and $\tau_+ = t + t'$. We obtain

$$\int_0^T \mathrm{d}t \int_0^T \mathrm{d}t'\; g(0, |t - t'|) = \frac{1}{2} \int_0^T \mathrm{d}\tau \int_\tau^{2T-\tau} \mathrm{d}\tau_+ \left[g(0, \tau) + g(0, \tau)\right] = \\ = 2 \int_0^T \mathrm{d}\tau\; (T - \tau)\; g(0, \tau).$$

We derive both sides of Eq. (3.36) with respect to T

$$\frac{\mathrm{d}}{\mathrm{d}T} \left\{ 2 \int_0^T \mathrm{d}\tau\; (T - \tau)\; g(0, \tau) \right\} = \frac{\mathrm{d}}{\mathrm{d}T} \Big[4\Big(\frac{l_p}{c}\Big)^{\frac{4}{3}} T^{\frac{2}{3}} \Big], \tag{3.37}$$

so we have

$$\int_0^T g(0, \tau) \mathrm{d}\tau = \frac{4}{3}\Big(\frac{l_p}{c}\Big)^{\frac{4}{3}} T^{-\frac{1}{3}}. \tag{3.38}$$

We derive one more time, thus obtaining

$$\frac{\mathrm{d}}{\mathrm{d}T} \Big[\frac{4}{3}\Big(\frac{l_p}{c}\Big)^{\frac{4}{3}} T^{-\frac{1}{3}} \Big], \tag{3.39}$$

and

$$g(0, T) = -\frac{4}{9}\Big(\frac{l_p}{c}\Big)^{\frac{4}{3}} T^{-\frac{4}{3}}. \tag{3.40}$$

The fact that the correlation in Eq. (3.40) is not proportional to a Dirac delta $\delta(T)$ implies that the Károlyházy model is necessarily non-Markovian. This is reflected in the predicted emitted rate in Eq. (3.29), which does not have dependence $1/\omega$ typical of the Markovian models, see for example Eq. (3.31) or [73, 74]. Note that the non-Markovianity is present also for the original Károlyházy's proposal, see the master Eq. (6) in [49], which is clearly not-Markovian. Let us now introduce the Fourier transform of the correlation function $g(\boldsymbol{y}, |\tau|)$

$$\tilde{g}(\boldsymbol{k}, \omega) := \int_{-\infty}^{+\infty} \mathrm{d}\boldsymbol{y} \int_{-\infty}^{+\infty} \mathrm{d}\tau e^{-i(\boldsymbol{k}\cdot\boldsymbol{y} + \omega\tau)} g(\boldsymbol{y}, \tau). \tag{3.41}$$

This implies that

$$g(0, \tau) = \frac{1}{(2\pi)^4} \int_{-\infty}^{+\infty} \mathrm{d}\omega\; e^{i\omega\tau} f(\omega), \tag{3.42}$$

where we defined

$$f(\omega) := \int_{-\infty}^{+\infty} \mathrm{d}\boldsymbol{k}\ \tilde{g}(\boldsymbol{k},\omega). \tag{3.43}$$

By comparing Eq. (3.40) with Eq. (3.42) we obtain that

$$f(\omega) = (2\pi)^3 \frac{4\sqrt{3}}{3}\left(\frac{l_p}{c}\right)^{\frac{4}{3}}\Gamma\left(\frac{2}{3}\right)\omega^{\frac{1}{3}}. \tag{3.44}$$

To summarize, we showed that given a correlation function of the form $g(0,\tau)$, and its Fourier transform $\tilde{g}(\boldsymbol{k},\omega)$, the Károlyházy condition in Eq. (3.6) corresponds to the condition in Eq. (3.44) with $f(\omega)$ defined in Eq. (3.43).

The next task is to compute the constraints on the correlation function given by experimental data. We will consider two scenarios: radiation emission, as discussed before, and violation of energy conservation, both induced by the gravitational noise.

3.4.1 Radiation emission rate

Starting with radiation emission, given in Eq. (3.23), which is true in general and that, for the sake of convenience, we report here

$$P(t) = \frac{e^2}{6\pi\epsilon_0 c^3}\frac{1}{(2\pi)^2}\sum_{j=1}^{3}\int_{-\infty}^{+\infty}\mathrm{d}\nu\int_{-\infty}^{+\infty}\mathrm{d}\omega\ e^{i(\nu+\omega)t}\ \mathbb{E}[a_j(\boldsymbol{x},\omega)a_j(\boldsymbol{x},\nu)], \tag{3.45}$$

we need to compute the correlations $\mathbb{E}[a_i(\boldsymbol{x},\omega)a_j(\boldsymbol{x},\nu)]$. We follow the same step as done in Section 3.3 but now the correlations be used are those in Eq. (3.33). As before, we consider the general factorized form of correlation function $g(\boldsymbol{y},\tau)$. We use the same step done in Eq. (3.41-3.43), relating the correlation function to the acceleration with Eq. (3.26) and we obtain the expression for the correlations

$$\mathbb{E}[a_i(\boldsymbol{x},\omega)a_j(\boldsymbol{x},\nu)] = \frac{c^4}{4(2\pi)^2}\delta(\omega+\nu)\int_{-\infty}^{+\infty}\mathrm{d}\boldsymbol{k}\ k_i k_j \tilde{g}(\boldsymbol{k},\omega). \tag{3.46}$$

By substituting this in Eq. (3.45), we arrive at the radiation emission rate in terms of $\tilde{g}(\boldsymbol{k},\omega)$

$$P(t) = \frac{e^2 c}{12(2\pi)^5\epsilon_0}\int_{-\infty}^{+\infty}\mathrm{d}\boldsymbol{k}\int_{-\infty}^{+\infty}\mathrm{d}\omega\ k^2\tilde{g}(\boldsymbol{k},\omega). \tag{3.47}$$

The corresponding emission rate can be found by comparing this equation to Eq. (3.21), leading to

$$\frac{\mathrm{d}\Gamma(t)}{\mathrm{d}\omega} = \frac{e^2 c}{6(2\pi)^5 \epsilon_0} \frac{1}{\hbar\omega} \int_{-\infty}^{+\infty} \mathrm{d}\boldsymbol{k}\, k^2 \tilde{g}(\boldsymbol{k}, \omega), \tag{3.48}$$

where the factor 6 in place of the factor 12 in the denominator is due to the fact that the integral in Eq. (3.21) goes from 0 to $+\infty$, while that in Eq. (3.47) goes from $-\infty$ to $+\infty$. This is the radiation emission rate for a generic correlation function of the form introduced in Eq. (3.33). Any function $\tilde{g}(\boldsymbol{k}, \omega)$ is allowed, as long as it satisfies the relation in Eq. (3.44) with $f(\omega)$ given by Eq. (3.43) and, at the same time, it predicts a radiation emission rate compatible with experimental bounds [76]. Considering the data in [76] (namely, the bound $\lambda/r_C^2 \leq 5.39 \times 10^{-1}\mathrm{s}^{-1}\mathrm{m}^{-2}$), which currently sets the strongest bound on the radiation emission rate, one arrives at the bound

$$\int_{-\infty}^{+\infty} \mathrm{d}\boldsymbol{k}\, k^2 \tilde{g}(\boldsymbol{k}, \omega) \leq 3.6 \times 10^{-46} \frac{\mathrm{s}}{\mathrm{m}^2}, \tag{3.49}$$

for all the frequencies ω corresponding to the energies considered in the experiment, which are in the range of [1-1000] KeV.

3.4.2 Energy violation

We next consider energy violation. All collapse models and decoherence models imposing position spread [83] predict a change of the kinetic energy of a system due to the interaction with the noise inducing the diffusion [83]. This effect is present also in the Károlyházy model, where the random fluctuations of the metric induce diffusion in momentum. Several experiments based on this energy increase have been considered for the CSL model, ranging from optomechanical devices [84, 85], to cold atoms [77], to thermal emission from planetary systems [86]. Recently, strong bounds have been set by studying the residual heat leak experiments performed in ultra-low temperature cryostats for both the CSL model [87, 88] as well as the DP model [89]. Here we extend this analysis to the Károlyházy model. As can be understood from the experiments carried out so far, one of the most efficient strategy to analyse the energy violation is the study of the heating rate of a crystal per unit of mass, which we derive below. We derive it following closely the derivation done in [87] for the CSL model when applied to

a crystal. An alternative derivation, which resort to a perturbative approach, can be found in [88].

We start by rewriting the master equation. In particular, we Fourier expand the mass density operator, thus obtaining

$$\hat{\mu}(\boldsymbol{x}) = \frac{1}{(2\pi)^3}\int \mathrm{d}\boldsymbol{k} \sum_i m_i \tilde{\mu}(\boldsymbol{k}) e^{i\boldsymbol{k}\cdot(\boldsymbol{x}-\hat{\boldsymbol{q}}_i)} = \frac{m_0}{(2\pi)^3}\int \mathrm{d}\boldsymbol{k}\; e^{i\boldsymbol{k}\cdot\boldsymbol{x}}\tilde{\mu}(\boldsymbol{k})\hat{L}(\boldsymbol{k}), \tag{3.50}$$

where we used the definitions for the Fourier and the anti-Fourier transforms

$$\tilde{\mu}(\boldsymbol{k}) := \int \mathrm{d}\boldsymbol{x}\; \mu(\boldsymbol{x}) e^{-i\boldsymbol{k}\cdot\boldsymbol{x}}, \qquad \mu(\boldsymbol{x}) = \frac{1}{(2\pi)^3}\int \mathrm{d}\boldsymbol{k}\; \tilde{\mu}(\boldsymbol{k}) e^{i\boldsymbol{k}\cdot\boldsymbol{x}}, \tag{3.51}$$

and where

$$\hat{L}(\boldsymbol{k}) := \sum_i \frac{m_i}{m_0} e^{-i\boldsymbol{k}\cdot\hat{\boldsymbol{q}}_i}. \tag{3.52}$$

By replacing Eq. (3.50) in the Eq. (3.34) and carrying on the integrals, one gets

$$\begin{aligned}\frac{\mathrm{d}\hat{\rho}(t)}{\mathrm{d}t} = &-\frac{i}{\hbar}\left[\hat{H},\hat{\rho}(t)\right] - \left(\frac{c^2}{2\hbar}\right)^2 \frac{m_0^2}{(2\pi)^3}\int \mathrm{d}\boldsymbol{k}\int_0^t \mathrm{d}t'\; \tilde{h}(\boldsymbol{k},t-t') \\ &\times\left[\hat{L}^\dagger(\boldsymbol{k}),\left[e^{\frac{i}{\hbar}\hat{H}(t'-t)}\hat{L}(\boldsymbol{k})e^{-\frac{i}{\hbar}\hat{H}(t'-t)},\hat{\rho}(t)\right]\right],\end{aligned} \tag{3.53}$$

where we introduced

$$\tilde{h}(\boldsymbol{k},t-t') := |\tilde{\mu}(\boldsymbol{k})|^2 \tilde{g}(\boldsymbol{k},t-t'), \tag{3.54}$$

and

$$\tilde{g}(\boldsymbol{k},t-t') = \int \mathrm{d}\boldsymbol{x}\; g(\boldsymbol{x},t-t') e^{-i\boldsymbol{k}\cdot\boldsymbol{x}}. \tag{3.55}$$

Given the master equation in Eq. (3.53), one can associate a corresponding *unitary unravelling*, i.e., a stochastic Schrödinger equation whose ensemble average over the noise reproduces the same reduced dynamics. In this picture, each realization of the noise $w(t,\boldsymbol{k})$ generates a possible stochastic trajectory $|\psi(t)\rangle$ for the system state, and the statistical properties of the noise are chosen such that the mean over all trajectories recover the master equation (3.53). This This construction makes explicit the connection between the abstract master equation and individual system evolutions, as is common in collapse and decoherence models. This is given

by a stochastic Schrödinger equation of the form

$$i\hbar\frac{\mathrm{d}|\psi(t)\rangle}{\mathrm{d}t} = \left[\hat{H} + \hat{V}(t)\right]|\psi(t)\rangle, \tag{3.56}$$

where

$$\hat{V}(t) = -\hbar\int\frac{\mathrm{d}\boldsymbol{k}}{(2\pi)^3}w(t,\boldsymbol{k})\hat{L}(\boldsymbol{k}), \tag{3.57}$$

with $w(t,\boldsymbol{k})$ being a noise with zero average and correlation

$$\mathbb{E}\left[w(t,\boldsymbol{k})w(t',\boldsymbol{k}')\right] = (2\pi)^3\frac{m_0^2c^4}{4\hbar^2}\tilde{h}(-\boldsymbol{k},t-t')\delta(\boldsymbol{k}+\boldsymbol{k}'). \tag{3.58}$$

Note that the requirement $\hat{V}(t)$ being Hermitian implies that $w(t,\boldsymbol{k}) = w^*(t,-\boldsymbol{k})$. Equation (3.57) should be compared to the stochastic potential induced by the CSL model shown in Eq. (4) of [87], namely

$$\hat{V}(t) = -\hbar\int\frac{\mathrm{d}\boldsymbol{k}}{(2\pi)^3}e^{-r_c^2k^2/2}\,\xi(t,\boldsymbol{k})\hat{L}(\boldsymbol{k}), \tag{3.59}$$

where $\xi(t,\boldsymbol{k}) = \mathrm{d}W(t,\boldsymbol{k})/\mathrm{d}t$ is a complex Gaussian noise field where $W(t,\boldsymbol{k})$ is a Wiener process. We see that the two models are identical as long as one replaces

$$e^{-r_C^2\boldsymbol{k}^2/2}\xi(t,\boldsymbol{k}) \longrightarrow w(t,\boldsymbol{k}), \tag{3.60}$$

with the correlation of the $w(t,\boldsymbol{k})$ given in Eq. (3.58).

Given a three-dimensional crystal, we want to obtain the total energy at time t and we use the notation of [87], which we briefly summarize here. We adopt the labeling of atoms within a primitive cell, a convention commonly used in solid-state textbooks, see for example [90]. A primitive cell is defined by three primitive vectors a_1, a_2, a_3 forming a parallelepiped. The i-th primitive cell is located at the i-th lattice site, with position vector $\boldsymbol{R}_i$, commonly referred to as the lattice vector of the i-th site. Each $\boldsymbol{R}_i$ can be expressed as $\boldsymbol{R}_i = \sum_{l=1}^{3} n_{il}\boldsymbol{a}_l$, where n_{il} are integers. Atoms within each primitive cell are indexed by Greek letters ν, κ, ranging from 1 to r, where r is the number of atoms in a primitive cell. Greek indices α, β denote Cartesian components ($\alpha, \beta = 1, 2, 3$). To specify the positions of atoms within a primitive cell, a set of basis vectors d_ν is introduced, pointing from the origin of the cell to the ν-th atom. The equilibrium position of the ν-th atom in the i-th primitive cell is $\boldsymbol{R}_i + \boldsymbol{d}_\nu$. Thus, the α-th component

of the instantaneous position operator for the ν-th atom in the i-th primitive cell can be expressed as the sum of a classical equilibrium position and a quantum displacement

$$\hat{x}_{\alpha,i\nu} = R_{\alpha,i} + d_{\alpha,\nu} + \hat{u}_{\alpha,i\nu}, \tag{3.61}$$

where the quantum displacement operator $\hat{\boldsymbol{u}}_{i\nu}$ can be written in terms of phonon creation and annihilation operators of crystal phonons [91], namely where the first sum is performed over the mode in the first Brillouin zone (BZ),

$$\hat{\boldsymbol{u}}_{\alpha,i\nu} = \sum_{\boldsymbol{k}\in \mathrm{BZ}} \sum_{s=1}^{3r} \left(\frac{\hbar}{2NM_\nu \omega_{\boldsymbol{k}s}}\right)^{1/2} [\boldsymbol{\epsilon}^{(s)}_{\alpha,\nu}(\boldsymbol{k}) e^{i\boldsymbol{k}\cdot\boldsymbol{R}_i} \hat{\boldsymbol{a}}_{\boldsymbol{k}s} + \mathrm{H.}c.], \tag{3.62}$$

where N is the total number of primitive cells, M_ν is the mass of the ν-th atom, and $\boldsymbol{\epsilon}^{(s)}_{\alpha,\nu}$ are normalized vectors that describe the direction in which the ν-th atom moves. Finally, the total energy at time t is given by

$$\mathbb{E}\left[\hat{H}(t)\right] = \sum_{\boldsymbol{k}\in \mathrm{BZ}} \sum_{s=1}^{3r} \hbar\omega_{\boldsymbol{k}s} \mathbb{E}\left[\hat{a}^\dagger_{\boldsymbol{k}s}(t)\hat{a}_{\boldsymbol{k}s}(t)\right], \tag{3.63}$$

where the second sum runs over the $3r$ vibrational branches of the crystal, which include the acoustic branches, corresponding to collective modes in which neighboring atoms oscillate approximately in phase and whose frequency vanishes as $\boldsymbol{k} \to 0$, and the optical branches, corresponding to modes in which neighboring atoms oscillate out of phase and typically have a finite frequency at $\boldsymbol{k} = 0$, and $\hat{a}_{\boldsymbol{k}s}(t)$ and $\hat{a}^\dagger_{\boldsymbol{k}s}(t)$ are, respectively, the phonons annihilation and creation operators evolved in the Heisenberg picture at time t. Having established the connection in Eq. (3.60) between our model and the CSL model studied in [87], we can directly take the solution for $\hat{a}_{\boldsymbol{k}s}(t)$ in [87] and use the replacement in Eq. (3.60). So, we get

$$\hat{a}_{\boldsymbol{k}s}(t) = e^{-i\omega_{\boldsymbol{k}s}t}\hat{a}_{\boldsymbol{k}s} + i\int \frac{\mathrm{d}\tilde{\boldsymbol{k}}}{(2\pi)^3} \int_0^t \mathrm{d}t' e^{-i\omega_{\boldsymbol{k}s}(t-t')} w(\tilde{\boldsymbol{k}}, t') \sum_{i,\nu} \frac{m_\nu}{m_0} e^{-i\tilde{\boldsymbol{k}}\cdot(\boldsymbol{R}_i+\boldsymbol{d}_\nu)} \eta_{i\nu;\boldsymbol{k}s}(\tilde{\boldsymbol{k}}), \tag{3.64}$$

where

$$\eta_{i\nu;\boldsymbol{k}s}(\tilde{\boldsymbol{k}}) = -i\left(\frac{\hbar}{2Nm_\nu\omega_{\boldsymbol{k}s}}\right)^{\frac{1}{2}} \sum_\alpha \tilde{k}_\alpha \boldsymbol{\epsilon}^{(s)*}_{\alpha,\nu}(\boldsymbol{k}) e^{-i\boldsymbol{k}\cdot\boldsymbol{R}_i}. \tag{3.65}$$

Inserting Eq. (3.64) in Eq. (3.63), using Eq. (3.58) and carrying out the calculation we obtain

$$\mathbb{E}\left[\hat{H}(t)\right] = \hat{H} + \frac{m_0^2 c^4}{4\hbar^2} \sum_{\boldsymbol{k}\in \mathrm{B}Z} \sum_{s=1}^{3r} \hbar\omega_{\boldsymbol{k}s} \int \frac{\mathrm{d}\tilde{\boldsymbol{k}}}{(2\pi)^3} \int_0^t \mathrm{d}t' \int_0^t \mathrm{d}t' e^{i\omega_{\boldsymbol{k}s}(t'-t'')} \tilde{h}(\tilde{\boldsymbol{k}}, t''-t') \times \left(\sum_{j,\kappa} \frac{m_\kappa}{m_0} e^{i\tilde{\boldsymbol{k}}\cdot(\boldsymbol{R}_j+\boldsymbol{d}_\kappa)} \eta^*_{j\kappa;\boldsymbol{k}s}(\tilde{\boldsymbol{k}}) \sum_{i,\nu} \frac{m_\nu}{m_0} e^{-i\tilde{\boldsymbol{k}}\cdot(\boldsymbol{R}_i+\boldsymbol{d}_\nu)} \eta_{i\nu;\boldsymbol{k}s}(\tilde{\boldsymbol{k}}) \right). \tag{3.66}$$

By replacing the definition in Eq. (3.65) and using $\sum_{\boldsymbol{k}\in \mathrm{B}Z} = \frac{N}{V_{\mathrm{B}Z}} \int_{\mathrm{B}Z} \mathrm{d}\boldsymbol{k}$, we get[4]

$$\mathbb{E}\left[\hat{H}(t)\right] = \hat{H} + \frac{m_0^2 c^4}{4\hbar^2} \frac{\hbar^2}{2V_{\mathrm{B}Z}} \sum_{\kappa,\nu} \frac{\sqrt{m_\kappa m_\nu}}{m_0^2} \int \frac{\mathrm{d}\tilde{\boldsymbol{k}}}{(2\pi)^3} e^{i\tilde{\boldsymbol{k}}\cdot(\boldsymbol{d}_\kappa-\boldsymbol{d}_\nu)} \int_{\mathrm{B}Z} \mathrm{d}\boldsymbol{k} \sum_{i,j} e^{i(\tilde{\boldsymbol{k}}+\boldsymbol{k})\cdot(\boldsymbol{R}_j-\boldsymbol{R}_i)} \times \sum_{s=1}^{3r} \int_0^t \mathrm{d}t' \int_0^t \mathrm{d}t' e^{i\omega_{\boldsymbol{k}s}(t'-t'')} \tilde{h}(\tilde{\boldsymbol{k}}, t''-t') \left(\sum_{\alpha,\beta} \tilde{k}_\beta \tilde{k}_\alpha \boldsymbol{\epsilon}^{(s)*}_{\alpha,\nu}(\boldsymbol{k}) \boldsymbol{\epsilon}^{(s)}_{\beta,\kappa}(\boldsymbol{k}) \right). \tag{3.67}$$

We proceed by using [87]

$$\begin{aligned} \int_0^t \mathrm{d}t_1 \int_0^t \mathrm{d}t_2 \, e^{-i\omega_{\boldsymbol{k}s}(t_2-t_1)} f(t_2-t_1) &= \int_{-\infty}^{\infty} \frac{\mathrm{d}\omega}{2\pi} \gamma(\omega) \int_0^t \mathrm{d}t_1 \, e^{i(\omega_{\boldsymbol{k}s}-\omega)t_1} \int_0^t \mathrm{d}t_2 \, e^{i(\omega_{\boldsymbol{k}s}-\omega)t_2} \\ &= \int_{-\infty}^{\infty} \frac{\mathrm{d}\omega}{2\pi} \gamma(\omega) \int_{-t/2}^{t/2} \mathrm{d}t_1 \, e^{i(\omega_{\boldsymbol{k}s}-\omega)t_1} \int_{-t/2}^{t/2} \mathrm{d}t_2 \, e^{i(\omega_{\boldsymbol{k}s}-\omega)t_2} \\ &= \int_{-\infty}^{\infty} \frac{\mathrm{d}\omega}{2\pi} \gamma(\omega) [2\pi\delta^{(t)}(\omega_{\boldsymbol{k}s}-\omega)]^2, \end{aligned} \tag{3.68}$$

where $\gamma(\omega)$ is the collapse noise spectrum (also called collapse noise spectral density), $2\pi\delta^{(t)}(\omega) = \int_{-t/2}^{t/2} \mathrm{d}t' \, e^{-i\omega t'}$. Since $\delta^{(t)}(\omega_{\boldsymbol{k}s}-\omega)$ has its maximum at $\omega_{\boldsymbol{k}s} = \omega$ and falls rapidly to zero elsewhere, to a first approximation one can replace $[\delta^{(t)}(\omega_{\boldsymbol{k}s}-\omega)]^2 \approx \delta^{(t)}(\omega_{\boldsymbol{k}s}-\omega)\delta^{(t)}(0) = (t/2\pi)\delta^{(t)}(\omega_{\boldsymbol{k}s}-\omega)$. Also, when $\omega_{\boldsymbol{k}s}t \gg 1$, one can approximate $\delta^{(t)}(\omega_{\boldsymbol{k}s}-\omega) \approx \delta(\omega_{\boldsymbol{k}s}-\omega)$ (see Refs. [92–94]). Introducing these approximations into the above equations yields

$$\int_0^t \mathrm{d}t_1 \int_0^t \mathrm{d}t_2 e^{-i\omega_{\boldsymbol{k}s}(t_2-t_1)} \tilde{h}(\tilde{\boldsymbol{k}}, t_2-t_1) \approx t\tilde{H}(\tilde{\boldsymbol{k}}, \omega_{\boldsymbol{k}s}), \tag{3.69}$$

[4] See Eq. (1.2.13) in [91], which is different from the one reported in [87] but necessary to obtain the correct result.

where we introduced $\tilde{H}(\tilde{\boldsymbol{k}},\omega)$, such that

$$\tilde{H}(\tilde{\boldsymbol{k}},\omega)=\int_{-\infty}^{+\infty}\mathrm{d}t\;\tilde{h}(\tilde{\boldsymbol{k}},t)e^{-i\omega t}, \tag{3.70}$$

obtaining

$$\mathbb{E}\left[\hat{H}(t)\right]=\hat{H}+\frac{m_0^2c^4}{4\hbar^2}\frac{\hbar^2 t}{2V_{\mathrm{BZ}}}\sum_{\kappa,\nu}\frac{\sqrt{m_\kappa m_\nu}}{m_0^2}\int\frac{\mathrm{d}\tilde{\boldsymbol{k}}}{(2\pi)^3}e^{i\tilde{\boldsymbol{k}}\cdot(\boldsymbol{d}_\kappa-\boldsymbol{d}_\nu)}\int_{\mathrm{BZ}}\mathrm{d}\boldsymbol{k}\sum_{i,j}e^{i(\tilde{\boldsymbol{k}}+\boldsymbol{k})\cdot(\boldsymbol{R}_j-\boldsymbol{R}_i)}$$

$$\times\sum_{s=1}^{3r}\tilde{H}(\tilde{\boldsymbol{k}},\omega_{\boldsymbol{k}s})\sum_{\alpha,\beta}\tilde{k}_\beta\tilde{k}_\alpha\boldsymbol{\epsilon}^{(s)*}_{\alpha,\nu}(\boldsymbol{k})\boldsymbol{\epsilon}^{(s)}_{\beta,\kappa}(\boldsymbol{k}). \tag{3.71}$$

Note that, in Eq. (3.71), the $\tilde{\mathbf{k}}$ integration is over all momentum space, while $\mathbf{k}$ is confined inside the first Brillouin zone. Since the lattice constant is usually of the order $a\sim 10^{-10}$ - $10^{-9}\,\mathrm{m}$, we have $V_{\mathrm{BZ}}\sim 10^{29}$ - $10^{33}\,\mathrm{m}^{-3}$. The volume in which important $\tilde{\mathbf{k}}$ are inside is $V_c\sim(2\pi/R_K)^3\sim 10^{23}\,\mathrm{m}^{-3}$ (note $R_K\sim 10^{-7}\,\mathrm{m}$). This implies that the important $\tilde{\mathbf{k}}$ are well inside the first Brillouin zone. So we now assume that there is a cutoff in $\tilde{H}(\boldsymbol{k},\omega_{\boldsymbol{k}s})$ with respect to $\boldsymbol{k}$. Namely, there exists a characteristic length R_K such that only the modes with $k\leq 1/R_K$ are relevant. When $R_K\geq a\sim 10^{-10}-10^{-9}$ m (as we said, the typical lattice distances), all relevant $\boldsymbol{k}$'s are within the first Brillouin zone. Therefore, we can safely use the following summation relation (see Eq.(A.9b) of [91])

$$\sum_i e^{i(\tilde{\boldsymbol{k}}+\boldsymbol{k})\cdot\boldsymbol{R}_i}=V_{\mathrm{BZ}}\delta(\tilde{\boldsymbol{k}}+\boldsymbol{k}), \tag{3.72}$$

which implies

$$\sum_{i,j}e^{i(\tilde{\boldsymbol{k}}+\boldsymbol{k})\cdot(\boldsymbol{R}_j-\boldsymbol{R}_i)}=V_{\mathrm{BZ}}\delta(\tilde{\boldsymbol{k}}+\boldsymbol{k})N. \tag{3.73}$$

Then, we get

$$\mathbb{E}\left[\hat{H}(t)\right]=\hat{H}+\frac{m_0^2c^4}{4\hbar^2}\frac{\hbar^2 tN}{2}\frac{1}{m_0^2}\int\frac{\mathrm{d}\boldsymbol{k}}{(2\pi)^3}\sum_{s=1}^{3r}\tilde{H}(-\boldsymbol{k},\omega_{\boldsymbol{k}s})\left|\sum_\kappa\sum_\beta\sqrt{m_\kappa}k_\beta\boldsymbol{\epsilon}^{(s)}_{\beta,\kappa}(\boldsymbol{k})e^{-i\boldsymbol{k}\cdot\boldsymbol{d}_\kappa}\right|^2. \tag{3.74}$$

Again due to the cutoff in $\tilde{H}$, we can approximate $e^{-i\boldsymbol{k}\cdot\boldsymbol{d}_\kappa}\simeq 1$. In addition, for $r_c\gg a$, one can safely use the long-wave limit (see Ref. [95], Sec. 4.3.3) where, to leading order in a/r_C, we replaced $\mathbf{e}^{(s)}_{\alpha,\nu}(\mathbf{k})\approx\mathbf{e}^{(s)}_{\alpha,\nu}(\mathbf{0})$. In the long-wave limit, the optical branches (denoted by s_O) obey $\sum_\nu\sqrt{M_\nu}\,\mathbf{e}^{(s_O)}_{\alpha,\nu}(\mathbf{0})=0$, where $M=$

$N\sum_\kappa m_\kappa$ is the total mass of the crystal. For the acoustic branches (denoted by s_A), we have $\mathbf{e}_\nu^{(s_A)}(\mathbf{0})/\sqrt{M_\nu} = (\sum_\kappa M_\kappa)^{-1/2}$. Accordingly, to leading order in a/r_C, the above equation is dominated only by the longitudinal acoustic branch, which simplifies the formula to

$$\mathbb{E}\left[\hat{H}(t)\right] = \hat{H} + \frac{c^4}{8} Mt \int \frac{\mathrm{d}\boldsymbol{k}}{(2\pi)^3} \tilde{H}(\boldsymbol{k}, \omega_{\boldsymbol{k}LA}) \boldsymbol{k}^2, \tag{3.75}$$

where $\omega_{\boldsymbol{k}LA} = |\boldsymbol{k}| v_s$ denotes the linear dispersion relation of the longitudinal acoustic (LA) branch, with v_s the sound velocity in the crystal. As discussed above, in the long-wavelength regime relevant here, the energy contribution is dominated by this branch, while transverse acoustic and optical branches give subleading corrections. Moreover, we performed the change of variables $\boldsymbol{k} \to -\boldsymbol{k}$, which leaves the integral invariant due to the isotropy of the integrand. The corresponding heating rate per unit mass is then obtained by taking the time derivative of the energy expectation value and dividing by the total mass M. Since the first term in Eq. (3.75) is time independent, only the second term contributes to the heating rate, leading to

$$\frac{\mathrm{d}E(t)}{M\mathrm{d}t} = \frac{c^4}{8} \int_{-\infty}^{+\infty} \frac{\mathrm{d}\boldsymbol{k}}{(2\pi)^3} \tilde{H}(\boldsymbol{k}, |k| v_s) \boldsymbol{k}^2, \tag{3.76}$$

which appears just the derivative of the second term of Eq. (3.75), since the first one is time-independent. In general, given the definitions above, one can see that

$$\tilde{H}(\boldsymbol{k}, \omega) = |\tilde{\mu}(\boldsymbol{k})|^2 \tilde{g}(\boldsymbol{k}, \omega). \tag{3.77}$$

For point-like mass densities, which are those we are interested in, $\tilde{\mu}(\boldsymbol{k}) = 1$ and $\tilde{H}(\boldsymbol{k}, \omega) = \tilde{g}(\boldsymbol{k}, \omega)$. In this case, Eq. (3.76) reduces to

$$\frac{\mathrm{d}E(t)}{M\mathrm{d}t} = \frac{c^4}{8} \int_{-\infty}^{+\infty} \frac{\mathrm{d}\boldsymbol{k}}{(2\pi)^3} \tilde{g}(\boldsymbol{k}, |k| v_s) \boldsymbol{k}^2. \tag{3.78}$$

In deriving Eq. (3.78) it was assumed that the correlation function $\tilde{H}(\boldsymbol{k}, \omega)$ has a cutoff in $\boldsymbol{k}$ at $k = |\boldsymbol{k}| \leq 1/a$. Following [89], in which strong bounds have been set by analyzing spontaneous heating of matter at low temperatures, namely by studying the residual heat leak experiments performed in ultra-low temperature cryostats for the DP model, and by considering the cryostat described by Gloos

et al. [96], one can safely assume $\frac{\mathrm{d}E(t)}{\mathrm{d}M\mathrm{d}t} \leq 10$ pW/Kg, which implies

$$\int_{-\infty}^{+\infty} \mathrm{d}\boldsymbol{k}\, \tilde{g}(\boldsymbol{k}, |k|v_s)\boldsymbol{k}^2 \leq 2.5 \times 10^{-42}\, \frac{\mathrm{s}}{\mathrm{m}^2}, \tag{3.79}$$

assuming $v_s = 4000$ m/s, which is the speed of sound in copper at low temperatures.

So we have shown that any function of the form $g(\boldsymbol{x} - \boldsymbol{x}', t - t')$ that satisfies the experimental bounds given in [89] and [96], and is based on the crystal heating described by Eq. (3.79), is a valid correlation function $\tilde{g}(\boldsymbol{k}, \omega)$, with a cutoff at $|\boldsymbol{k}| \leq k_{\mathrm{max}} = 10^9\ \mathrm{m}^{-1}$.

3.5 A possible choice of the correlation function

In this Section, we go back to our initial question: is it possible that, by considering a factorised correlation function satisfying the constraint in Eq. (3.6), we can obtain a radiation emission rate compatible with experimental data? We now show that the answer to the question is positive.

Let us assume that the correlation function is of the factorized form

$$g(\boldsymbol{y}, \tau) = u(\boldsymbol{y})v(\tau). \tag{3.80}$$

Then, Eq. (3.40) imposes

$$v(\tau) = -\frac{4}{9}\left(\frac{l_p}{c}\right)^{\frac{4}{3}} \frac{1}{u(0)}\tau^{-\frac{4}{3}}. \tag{3.81}$$

We now specify the form of the spatial correlation function $u(\boldsymbol{y})$. It is reasonable to expect that fluctuations related to points in space at relatively small distances are larger compared to those between faraway points. Keeping this in mind, and inspired by the correlation function of the CSL model [23], we consider the spatial correlation function

$$u(\boldsymbol{y}) = e^{-\frac{\boldsymbol{y}^2}{R_K^2}}, \tag{3.82}$$

where spatial correlation length R_K is a free parameter.

3.5.1 Radiation emission rate

The radiation emission rate depends on the Fourier transform $\tilde{g}(\boldsymbol{k},\omega)$ of g, which is also factorized, i.e. $\tilde{g}(\boldsymbol{k},\omega) = \tilde{u}(\boldsymbol{k})\tilde{v}(\omega)$ with $\tilde{v}(\omega)$ derived from Eq. (3.44), namely

$$\tilde{v}(\omega) = \int_{-\infty}^{+\infty} \mathrm{d}\tau\, e^{-i\omega\tau} v(\tau) = \frac{4\Gamma\left(\frac{2}{3}\right)\left(\frac{l_p}{c}\right)^{4/3}}{\sqrt{3}u(0)}\omega^{\frac{1}{3}}. \tag{3.83}$$

Then, the radiation emission rate in Eq. (3.48) becomes

$$\frac{\mathrm{d}\Gamma(t)}{\mathrm{d}\omega} = \frac{e^2 c}{48\pi^5\epsilon_0\hbar}\frac{\Gamma\left(\frac{2}{3}\right)}{\sqrt{3}}\left(\frac{l_p}{c}\right)^{\frac{4}{3}}\frac{\int_{-\infty}^{+\infty}\mathrm{d}\boldsymbol{k}\, k^2\tilde{u}(\boldsymbol{k})}{u(0)}\omega^{-\frac{2}{3}}. \tag{3.84}$$

Also the corresponding bound of Eq. (3.49) depends on the Fourier transform $\tilde{g}(\boldsymbol{k},\omega)$, so it becomes

$$\frac{4\Gamma\left(\frac{2}{3}\right)\left(\frac{l_p}{c}\right)^{4/3}}{\sqrt{3}}\frac{|\omega|^{\frac{1}{3}}}{u(0)}\int_{-\infty}^{+\infty}\mathrm{d}\boldsymbol{k}\, k^2\tilde{u}(\boldsymbol{k}) \leq 3.6\times 10^{-46}\frac{\mathrm{s}}{\mathrm{m}^2}, \tag{3.85}$$

which should be fulfilled for the values of ω considered in the experiments, which range from $[10^{17} - 10^{20}]$ Hz, corresponding to energies of the emitted photons in the range [1-1000] KeV. This is clearly possible with an appropriate choice of the function $\tilde{u}$.

For the specific choice of spatial correlation function as in Eq. (3.82), the bound from radiation emission in Eq. (3.85), considering photons with frequency of $\omega = 10^{18} - 10^{19}$ Hz (which are the ones providing the strongest bound [76]), implies that

$$R_K \geq 0.11\ \mathrm{m}. \tag{3.86}$$

So, we proved that by requiring the decoherence to be compatible with experimental data, this is the range of values allowed for the parameter R_K.

3.5.2 Heating in a crystal

Regarding the heating in a crystal, the condition in Eq. (3.79) becomes

$$\frac{4\Gamma\left(\frac{2}{3}\right)\left(\frac{\ell_p}{c}\right)^{4/3} v_s^{1/3}}{\sqrt{3}u(0)}\int_{-\infty}^{+\infty}\mathrm{d}\boldsymbol{k}\,\tilde{u}(\boldsymbol{k})k^{\frac{7}{3}} \leq 2.5\times 10^{-42}\frac{\mathrm{s}}{\mathrm{m}^2}. \tag{3.87}$$

By imposing the form of $u(\boldsymbol{y})$ shown in Eq. (3.82), we find that the bound on R_K is

$$R_K \geq 1.8 \times 10^{-5}\ \mathrm{m}, \tag{3.88}$$

which is a weaker bound compared to that in Eq. (3.86).

3.5.3 Theoretical bound

Although the Károlyházy model is a decoherence model, it was proposed with the idea that it would be sufficient to explain the quantum to classical transition. We now know that this is not the case, and an actual spontaneous wave function collapse dynamics (which differs from the decoherence one) is needed. Nevertheless, one might be interested in understanding the minimal required action of the Károlyházy model to actually impose a decay of the interferences in a macroscopic superposition. As we will see, this translates into a theoretical upper bound on R_K, contrary to the lower bounds that come from experiments. Following the analysis performed in [97] for the CSL model, we require the Károlyházy effect to be strong enough to guarantee that a single-layered graphene disk of the size of $10\ \mu$m (roughly the smallest visible length by human eye) decohere in the time $t = 0.01$ s (about the smallest time resolution of the human eye).

In order to compute the decoherence effects, we start by considering the master equation (3.34). We set $\hat{H} = 0$, since we are considering free particles and big systems ($\hat{H} = \hat{\boldsymbol{p}}^2/2M$ becomes negligible in this way), and we are interested in estimating only the spatial decoherence. We write the master equation for the matrix element $\hat{\rho}(\boldsymbol{a}, \boldsymbol{b}, t) := \langle \boldsymbol{a}|\hat{\rho}(t)|\boldsymbol{b}\rangle$, where $|\boldsymbol{a}\rangle := |\boldsymbol{a}_1, ..., \boldsymbol{a}_N\rangle$ and $|\boldsymbol{b}\rangle := |\boldsymbol{b}_1, ..., \boldsymbol{b}_N\rangle$

$$\begin{aligned}\frac{\mathrm{d}\hat{\rho}(\boldsymbol{a}, \boldsymbol{b}, t)}{\mathrm{d}t} = -\left(\frac{c^2}{2\hbar}\right)^2 \int_0^t \mathrm{d}t' \sum_{i,j} m_i m_j \left[g(\boldsymbol{a}_i - \boldsymbol{a}_j, t - t') - g(\boldsymbol{a}_i - \boldsymbol{b}_j, t - t') - \right.\\ \left. - g(\boldsymbol{b}_i - \boldsymbol{a}_j, t - t') + g(\boldsymbol{b}_i - \boldsymbol{b}_j, t - t')\right] \hat{\rho}(\boldsymbol{a}, \boldsymbol{b}, t).\end{aligned} \tag{3.89}$$

If we now specialize to a factorized correlation function of the form in Eq. (3.80), the above master equation becomes

$$\frac{\mathrm{d}\hat{\rho}(\boldsymbol{a}, \boldsymbol{b}, t)}{\mathrm{d}t} = \left[-\left(\frac{c^2}{2\hbar}\right)^2 \left(\int_0^t \mathrm{d}t' v(t - t')\right) F(\boldsymbol{a}, \boldsymbol{b})\right] \hat{\rho}(\boldsymbol{a}, \boldsymbol{b}, t), \tag{3.90}$$

where we defined

$$F(\boldsymbol{a},\boldsymbol{b}) := \sum_{i,j} m_i m_j \left(u(\boldsymbol{a}_i-\boldsymbol{a}_j)-u(\boldsymbol{a}_i-\boldsymbol{b}_j)-u(\boldsymbol{b}_i-\boldsymbol{a}_j)+u(\boldsymbol{b}_i-\boldsymbol{b}_j)\right). \quad (3.91)$$

The solution of Eq. (3.90) is

$$\hat{\rho}(\boldsymbol{a},\boldsymbol{b},t) = \hat{\rho}(\boldsymbol{a},\boldsymbol{b},0)\exp\left[-\left(\frac{c^2}{2\hbar}\right)^2\left(\int_0^t \mathrm{d}t'\int_0^{t'}\mathrm{d}t''v(t'-t'')\right)F(\boldsymbol{a},\boldsymbol{b})\right], \quad (3.92)$$

with the time integrals giving the factor

$$\int_0^t \mathrm{d}t'\int_0^{t'}\mathrm{d}t''v(t'-t'') = \frac{2\pi\left(\frac{\ell_p}{c}\right)^{4/3}}{\pi u(0)}t^{2/3}, \quad (3.93)$$

if we consider $v(t)$ as in Eq. (3.81). To compute $F(\boldsymbol{a},\boldsymbol{b})$, we consider the spatial correlation function in Eq. (3.82). Keeping into account the bound in Eq. (3.86), and that we are considering a disk with radius 10 μm and a superposition distance $d = 10$ μm, we have that $R_K \geq 0.11$ m $\gg |\boldsymbol{a}_i-\boldsymbol{b}_j|$. Then, all Gaussian correlations can be Taylor expanded in the second order in $\boldsymbol{y}^2/R_K^2$, obtaining

$$\begin{aligned} F(\boldsymbol{a},\boldsymbol{b}) &\simeq -\frac{1}{R_K^2}\sum_{i,j} m_i m_j\left((\boldsymbol{a}_i-\boldsymbol{a}_j)^2-(\boldsymbol{a}_i-\boldsymbol{b}_j)^2-(\boldsymbol{b}_i-\boldsymbol{a}_j)^2+(\boldsymbol{b}_i-\boldsymbol{b}_j)^2\right) = \\ &= \frac{2}{R_K^2}\sum_{i,j} m_i m_j(\boldsymbol{a}_i-\boldsymbol{b}_i)\cdot(\boldsymbol{a}_j-\boldsymbol{b}_j). \end{aligned} \quad (3.94)$$

Taking into consideration that the disk is a rigid body and the superposition distance is $\boldsymbol{d}$, we have $\boldsymbol{b}_i = \boldsymbol{a}_i + \boldsymbol{d}$. Then, Eq. (3.94) further simplifies to

$$F(\boldsymbol{a},\boldsymbol{b}) = \frac{2M^2d^2}{R_K^2}, \quad (3.95)$$

with $M = 2.4\times10^{-16}$ kg being the mass of the graphene disk. By replacing these results in Eq. (3.92) and requiring the absolute value of the exponent to be larger than 10 (since e^{-10} is an arbitrary yet representative example of a sufficiently small number), so that the off diagonal elements are negligible, we obtain

$$R_K \leq 1.98 \text{ m}. \quad (3.96)$$

In summary, as shown in Figure 3.3, we proved that by requiring the decoherence

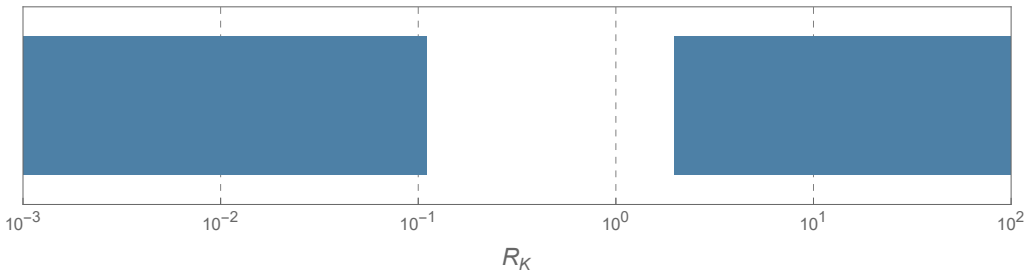

Figure 3.3: Exclusion plot for parameter R_K. The coloured areas correspond to excluded values of R_K obtained by requiring the decoherence to be compatible with experimental data and also being effective in decohering macroscopic systems.

to be compatible with experimental data and also being effective in decohering macroscopic systems, the range of values allowed for the parameter R_K is

$$0.11 \text{ m} \leq R_K \leq 1.98 \text{ m}. \tag{3.97}$$

Therefore, there is about one order of magnitude room for the parameter R_K to make the decoherence strong enough, while being compatible with experimental data.

The above analysis shows that, by relaxing the requirement that the fluctuation of the spacetime metric γ_β must fulfill the wave equation, it is possible to find models which comply with Károlyházy's condition in Eq. (3.6) and are, at the same time, compatible with experimental observations.

3.6 Summary

We reconsidered a proposal by Károlyházy on spacetime fluctuations [50, 51] as a possible source of decoherence in space. The original proposal was ruled out since it predicts a large amount of radiation emission rate from charged particles interacting with the stochastic gravitational background.

We considered generalizations of the Károlyházy model, where the constrain in Eq. (3.6) is still fulfilled, while the assumption that the stochastic metrics satisfies the wave equation [c.f. Eq. (3.14)] is relaxed. Our analysis shows that any function of the form $g(\boldsymbol{x}-\boldsymbol{x}', |t-t'|)$ that satisfies

(i) the Károlyházy's condition

$$\int_{-\infty}^{+\infty} \mathrm{d}\boldsymbol{k}\, \tilde{g}(\boldsymbol{k}, |\omega|) = (2\pi)^3 \frac{4\sqrt{3}}{3} \left(\frac{l_p}{c}\right)^{\frac{4}{3}} |\omega|^{\frac{1}{3}} \Gamma\left(\frac{2}{3}\right); \tag{3.98}$$

(ii) the experimental radiation emission bound

$$\int_{-\infty}^{+\infty} \mathrm{d}\boldsymbol{k}\; k^2 \tilde{g}(\boldsymbol{k}, |\omega|) \leq 3.6 \times 10^{-46} \frac{\mathrm{s}}{\mathrm{m}^2}, \tag{3.99}$$

for the values of ω considered in the experiments [76], which range from $[10^{17} - 10^{20}]$ Hz;

(iii) the experimental bound based on the heating of a crystal [89, 96]

$$\int_{-\infty}^{+\infty} \mathrm{d}\boldsymbol{k}\; k^2 \tilde{g}(\boldsymbol{k}, |k| v_s) \leq 2.5 \times 10^{-42}\; \frac{\mathrm{s}}{\mathrm{m}^2}, \tag{3.100}$$

where $v_s = 4000$ m/s is the speed of sound in copper at low temperatures, is a valid correlation function $\tilde{g}(\boldsymbol{k}, \omega)$, with a cutoff at $|\boldsymbol{k}| \leq k_{max} = 10^9\ \mathrm{m}^{-1}$.

We provided one example of correlation function which fulfills these conditions. In particular, for a factorized correlation function of the form $g(\boldsymbol{y}, |\tau|) = u(\boldsymbol{y}) v(|\tau|)$, with $u(\boldsymbol{y}) = exp[-\boldsymbol{y}^2/R_K^2]$ and the form of $v(|\tau|)$ being fixed by the condition set by Károlyházy, we showed that the allowed range of values for the parameter R_K is

$$0.11\ \mathrm{m} \leq R_K \leq 1.98\ \mathrm{m}. \tag{3.101}$$

This represents a narrowing of the admissible parameter interval.

3.7 Update

It is worth noting that, following the recent work published in pre-print by Aprile et al. [98], the value of the parameter λ/r_C^2 has been revised by two orders of magnitude, from $\lambda/r_C^2 = 5.39 \times 10^{-1}\mathrm{s}^{-1}\mathrm{m}^{-2}$ to $\lambda/r_C^2 = 4.4 \times 10^{-3}\mathrm{s}^{-1}\mathrm{m}^{-2}$. This result consequently changes all the quantities depending on the ratio λ/r_C^2 and the boundary on the Károlyházy model. In particular, change the radiation emission rate in Eq. (3.31) (see Figure 3.4). It becomes

$$\frac{\mathrm{d}\Gamma(t)}{\mathrm{d}\omega_{\boldsymbol{k}}}\Big|_{\mathrm{exp}} = \frac{4.15 \times 10^{-37}\ \mathrm{s}^{-1}}{\omega_{\boldsymbol{k}}}; \tag{3.102}$$

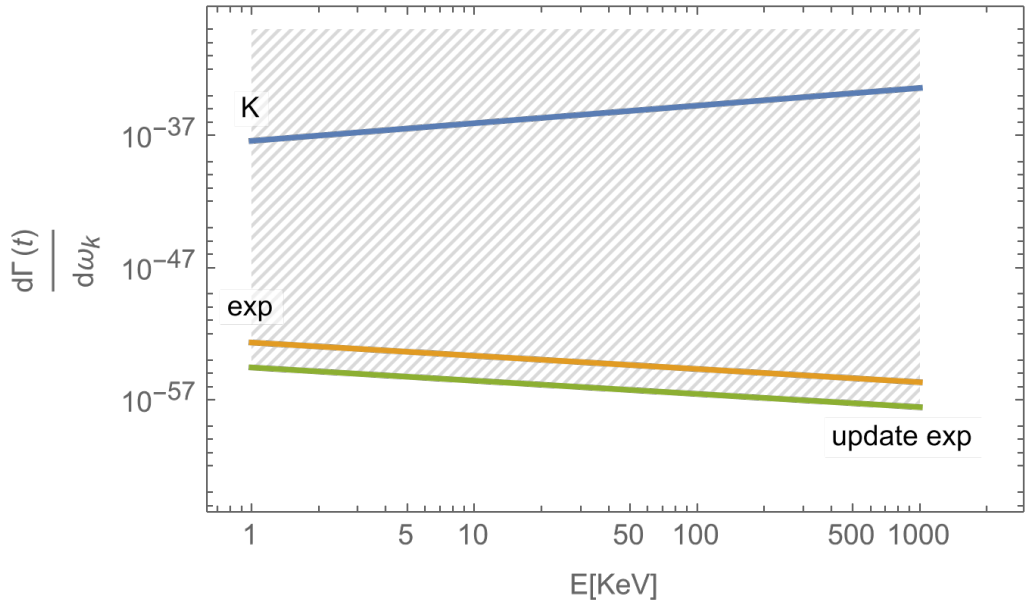

Figure 3.4: Comparison between the radiation emission rate predicted by Károlyházy's model in Eq. (3.29) (blue line), the upper bound on the rate inferred by the experimental data in Eq. (3.31) (orange line) and the upper bound on the rate inferred by the experimental data considering the update value of λ/r_C^2 in Eq. (3.102) (green line). The shaded area indicates the values of radiation emission rate that are excluded by the experiment in [98].

the experimental radiation emission bound in Eq. (3.49) (Eq. (3.99) in the Summary), which becomes

$$\int_{-\infty}^{+\infty} \mathrm{d}\boldsymbol{k}\; k^2 \tilde{g}(\boldsymbol{k}, |\omega|) \leq 2.93 \times 10^{-48} \frac{\mathrm{s}}{\mathrm{m}^2}; \tag{3.103}$$

and the allowed range of values for the parameter R_K in Eq. (3.97) (Eq. (3.101) in the Summary), which becomes

$$1.23\ \mathrm{m} \leq R_K \leq 1.98\ \mathrm{m}, \tag{3.104}$$

and in turn results in the Figure (3.5).

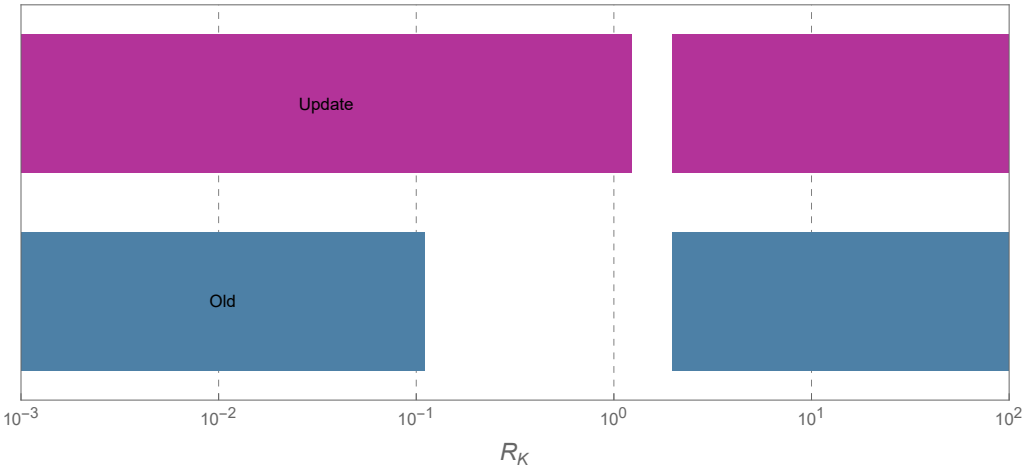

Figure 3.5: Exclusion plot for parameter R_K. The coloured areas correspond to excluded values of R_K. The blue area corresponds to excluded values of R_K given in Eq. (3.97), considering the old value of the parameter λ/r_C^2. The purple area corresponds to excluded values of R_K given in Eq. (3.104), considering the update value of the parameter λ/r_C^2.

Chapter 4

The Diósi–Penrose model

This chapter is based on the results presented in L. Figurato et al., *New Journal of Physics*, **26** (11), 113004 (2024) [99], which elaborates the data that were available until 2024.

4.1 Introduction

In this Chapter, we focus on the Diósi-Penrose model (DP) [25–27, 42, 56], which was already introduced in Chapter 2. In particular, we focus on a specific aspect of the model: that it should guarantee the localization of macroscopic objects. We refer to [100–104] for developments and further analysis.

As discussed in Chapter 2, the DP model relates a spontaneous collapse to gravity. As the mass of the quantum system increases and its associated gravitational field strengthens, the likelihood of spatial superposition of collapsing into well-localized states increases. The model is parametrized in terms of a free parameter R_0 having the dimensions of a length, and which smears the mass distribution of point particles.

The DP model makes different predictions compared to QM, hence it can be tested, resulting in experimental bounds on R_0. The idea behind setting the bound is as follows: various experiments are analyzed, and since no deviations from standard quantum mechanics are observed within a certain confidence level, we can safely conclude that the collapse predicted by the DP model, if it exists, is weaker than a certain threshold. This results in a series of lower bounds on R_0, since the smaller the value of R_0, the stronger the collapse affecting the wave function. Several experiments have been considered: matter-wave interferometry [105], neutron star heating [106], gravitational waves detector [107], heat leakage in experiments with ultralow temperature cryostats [89], and spontaneous

emission of photons from atoms of Germanium crystals [76, 78]. Currently (without considering the recent work published in pre-print by Aprile et al. [98]), the strongest bound is $R_0 \gtrsim 4 \times 10^{-10}$ m [76].

Here we investigate possible theoretical upper bounds on R_0, which comes from the requirement that the collapse dynamics needs to serve its main purpose of justifying why we do not see macroscopic quantum superpositions, thus solving the quantum measurement problem. A similar analysis was already performed for the Continuous Spontaneous Localization (CSL) model in [28, 77]. The bound is then obtained by requiring that the model should collapse quantum superpositions of any macroscopic object before we can potentially see them. Clearly there is a lot of ambiguity in this request, given that the macroscopic domain cannot be defined precisely. We can try to remove part of this ambiguity by sharpening the request as follows: a collapse model explains classicality of the macroscopic world if a delocalized state of the smallest object, that can be directly seen by the human eye, collapses within its perception time. If this happens, the quantum state of any larger object will collapse even faster, and classicality is secured.

Our analysis will show that the DP model, strictly speaking, does not satisfy this requirement when applied to a single-layer graphene [108], with a side length of $L = 25\,\mu$m corresponding to about the smallest space resolution of the eye [109]. Therefore, it does not guarantee classicality. However, we will also show that the collapse becomes rapidly effective as soon as the mass of the object increases.

4.2 Diósi-Penrose equation for the center of mass of the system

Since we are dealing with a crystal (single-layer graphene), which is a rigid system, we can simplify the problem by reducing it to the study of its center of mass (CM). We start by deriving the DP master equation (ME) for the CM of the system.

We start from the ME of the DP model in Eq. (1.30), now for N particles, which we report here for convenience

$$\mathcal{D}[\hat{\rho}(t)] = -\frac{4\pi G}{\hbar} \int \mathrm{d}\boldsymbol{r} \int \mathrm{d}\boldsymbol{r}' \, \frac{1}{|\boldsymbol{r}-\boldsymbol{r}'|} \big[\hat{\mu}(\boldsymbol{r}'), \big[\hat{\mu}(\boldsymbol{r}), \hat{\rho}(t)\big]\big]. \tag{4.1}$$

To avoid the standard divergences that occur when dealing with point-like masses, the mass density operator $\hat{\mu}(\boldsymbol{r})$ is smeared over a width R_0, which is the only free parameter of the DP model. Specifically, by assuming for convenience that the mass density as well as the smearing are of a Gaussian form [28], for a system of N distinguishable particles of radius R_i, mass m_i and of position operator $\hat{\boldsymbol{x}}_i$, one obtains

$$\hat{\mu}(\boldsymbol{r}) = \sum_{i=1}^{N} \frac{m_i}{(2\pi R_{\text{eff},i}^2)^{3/2}} e^{-\frac{(\boldsymbol{r}-\hat{\boldsymbol{x}}_i)^2}{2R_{\text{eff},i}^2}}, \tag{4.2}$$

where $R_{\text{eff},i} = \sqrt{R_0^2 + R_i^2}$ is the effective radius of the particle. In the limit of a point-like particle, $R_{\text{eff},i}$ reduces to R_0. Under the assumption of a rigid body, we can rewrite every position operator $\hat{\boldsymbol{x}}_i$ ($i = 1, \dots, N$) of each i-th particle as

$$\hat{\boldsymbol{x}}_i = \hat{\boldsymbol{x}} + \boldsymbol{x}_i^{(0)}, \tag{4.3}$$

where $\hat{\boldsymbol{x}}$ is the position operator of the CM, and $\boldsymbol{x}_i^{(0)}$ is the classical displacement of the particle with respect to it. We substitute Eq. (4.3) in Eq. (4.2) and merge the latter with Eq. (4.1), where for the sake of simplicity we take all $R_{\text{eff,i}} = R_{\text{eff}}$ to be equal. By tracing over the internal degrees of freedom, one gets

$$\mathcal{D}\left[\hat{\rho}_{\text{CM}}(t)\right] = -\frac{4\pi G}{\hbar} \int \mathrm{d}\boldsymbol{r} \int \mathrm{d}\boldsymbol{r}' \frac{1}{|\boldsymbol{r}-\boldsymbol{r}'|} \left[\hat{\mu}_{\text{CM}}(\boldsymbol{r}'), \left[\hat{\mu}_{\text{CM}}(\boldsymbol{r}), \hat{\rho}_{\text{CM}}\right]\right], \tag{4.4}$$

where $\hat{\mu}_{\text{CM}}(\boldsymbol{r})$ is the mass density of the CM, which reads

$$\hat{\mu}_{\text{CM}}(\boldsymbol{r}) = \sum_{i=1}^{N} \frac{m_i}{(2\pi R_{\text{eff}}^2)^{3/2}} e^{-\frac{(\hat{\boldsymbol{x}}+\boldsymbol{x}_i^{(0)}-\boldsymbol{r})^2}{2R_{\text{eff}}^2}}. \tag{4.5}$$

This can be rewritten in a more convenient form in the momentum space

$$\hat{\mu}_{\text{CM}}(\boldsymbol{r}) = \sum_{i=1}^{N} \frac{m_i}{(2\pi)^3} \int \mathrm{d}\boldsymbol{q}\, e^{-i\boldsymbol{q}\cdot(\hat{\boldsymbol{x}}+\boldsymbol{x}_i^{(0)}-\boldsymbol{r})} e^{-R_{\text{eff}}^2 q^2/2}, \tag{4.6}$$

and the dissipator in Eq. (4.4) becomes

$$\begin{aligned}\mathcal{D}\left[\hat{\rho}_{\text{CM}}(t)\right] = -\frac{4\pi G}{\hbar} \int \mathrm{d}\boldsymbol{r} \int \mathrm{d}\boldsymbol{r}' \frac{1}{|\boldsymbol{r}-\boldsymbol{r}'|} \sum_{i,j=1}^{N} \frac{m_i m_j}{(2\pi)^6} \times \\ \times \int \mathrm{d}\boldsymbol{q} \int \mathrm{d}\boldsymbol{k}\, e^{-R_{\text{eff}}^2(\boldsymbol{q}^2+\boldsymbol{k}^2)/2} e^{-i\boldsymbol{q}\cdot(\boldsymbol{x}_i^{(0)}-\boldsymbol{r}')} e^{-i\boldsymbol{k}\cdot(\boldsymbol{x}_j^{(0)}-\boldsymbol{r})} \left[e^{-i\boldsymbol{q}\cdot\hat{\boldsymbol{x}}}, \left[e^{-i\boldsymbol{k}\cdot\hat{\boldsymbol{x}}}, \hat{\rho}_{\text{CM}}(t)\right]\right].\end{aligned} \tag{4.7}$$

We can simplify this expression by using the following identity

$$\frac{1}{|\boldsymbol{r}-\boldsymbol{r}'|}=\frac{1}{2\pi^2}\int \mathrm{d}\boldsymbol{p}\,\frac{e^{-i\boldsymbol{p}\cdot(\boldsymbol{r}-\boldsymbol{r}')}}{p^2}, \tag{4.8}$$

and straightforward calculations lead to the following ME of the CM of the system (here we reintroduce the unitary part of the ME for completeness)

$$\frac{\mathrm{d}\hat{\rho}_{\mathrm{CM}}(t)}{\mathrm{d}t}=-\frac{i}{\hbar}\big[\hat{H}_{\mathrm{CM}},\hat{\rho}_{\mathrm{CM}}(t)\big]+\int \mathrm{d}\boldsymbol{p}\,F(\boldsymbol{p})\left(e^{i\boldsymbol{p}\cdot\hat{\boldsymbol{x}}}\hat{\rho}_{\mathrm{CM}}(t)e^{-i\boldsymbol{p}\cdot\hat{\boldsymbol{x}}}-\hat{\rho}_{\mathrm{CM}}(t)\right), \tag{4.9}$$

where we expressed

$$F(\boldsymbol{p})=\frac{4G}{\pi\hbar}\sum_{i,j=1}^{N}m_i m_j\frac{e^{-R_{\mathrm{eff}}^2p^2}}{p^2}e^{i\boldsymbol{p}\cdot(\boldsymbol{x}_i^{(0)}-\boldsymbol{x}_j^{(0)})}, \tag{4.10}$$

which is the form factor accounting for the dimension and shape of the system.

We now want to study the evolution of the matrix elements in the position basis of $\hat{\rho}_{\mathrm{CM}}(t)$. Under the assumption that we can neglect the free evolution $\hat{H}_{\mathrm{CM}}$, when represented in the position basis, the CM density matrix evolves according to

$$\langle\boldsymbol{x}|\hat{\rho}_{\mathrm{CM}}(t)|\boldsymbol{y}\rangle\simeq\langle\boldsymbol{x}|\hat{\rho}_{\mathrm{CM}}(0)|\boldsymbol{y}\rangle\exp\left[-t/\tau(\boldsymbol{x}-\boldsymbol{y})\right], \tag{4.11}$$

with $\tau(\boldsymbol{d})=\hbar/\Delta E(\boldsymbol{d})$, where

$$\Delta E(\boldsymbol{d})=-8\pi G\int \mathrm{d}\boldsymbol{r}\int \mathrm{d}\boldsymbol{r}'\,\frac{\mu_{\mathrm{CM}}(\boldsymbol{r})\left[\mu_{\mathrm{CM}}(\boldsymbol{r}'+\boldsymbol{d})-\mu_{\mathrm{CM}}(\boldsymbol{r}')\right]}{|\boldsymbol{r}-\boldsymbol{r}'|}, \tag{4.12}$$

quantifies, in the Newtonian limit, the difference between the space-time curvatures generated by two well localised configurations superimposed at a distance $d=|\boldsymbol{d}|$. The explicit derivation of Eq. (4.11) and a detailed discussion of the validity of the approximation where we neglect the free Hamiltonian, is shown in Subsection 4.2.1 and 4.2.3 respectively.

4.2.1 Explicit derivation of $\Delta E(\mathrm{d})$

We now merge Eq. (4.12) with the explicit form of $\mu(\boldsymbol{r})=\langle\boldsymbol{x}|\hat{\mu}(\boldsymbol{r})|\boldsymbol{x}\rangle$ in Eq. (4.6), in which we assume that the N particles have the same mass m (a reasonable assumption, given that the system we will consider will consist of identical carbon atoms) and using the Fourier transform of the Coulomb potential in Eq. (4.8), we

obtain

$$\Delta E(\boldsymbol{d}) = -\sum_{i,j=1}^{N} \left[J_{ij}(\boldsymbol{d}, \boldsymbol{k}) - J_{ij}(0, \boldsymbol{k}) \right], \tag{4.13}$$

where $\boldsymbol{r}_{ij} = \boldsymbol{x}_i - \boldsymbol{x}_j$ and

$$J_{ij}(\boldsymbol{d}, \boldsymbol{k}) := \int \mathrm{d}\boldsymbol{k} \frac{1}{k^2} I_{ij}(\boldsymbol{d}, \boldsymbol{k}). \tag{4.14}$$

Hence we get, defining $\boldsymbol{a_{ij}} := \boldsymbol{d} + \boldsymbol{r}_{ij}$

$$\begin{aligned} J_{ij}(\boldsymbol{d}, \boldsymbol{k}) &= \frac{4Gm^2}{\pi} \int \mathrm{d}\boldsymbol{k} \frac{1}{k^2} e^{-k^2 R_{\text{eff}}^2 + i\boldsymbol{k}\cdot\boldsymbol{a_{ij}}} = \frac{4Gm^2}{\pi} \int_0^{2\pi} \mathrm{d}\phi \int_0^{\pi} \mathrm{d}\theta \sin(\theta) \int_0^{\infty} \mathrm{d}k \; e^{-k^2 R_{\text{eff}}^2 + ika_{ij}\cos\theta} \\ &= 8Gm^2 \int_{-1}^{1} \mathrm{d}x \int_0^{\infty} \mathrm{d}k \; e^{-k^2 R_{\text{eff}}^2 + ika_{ij}x} = \frac{8\pi Gm^2}{a_{ij}} \operatorname{erf}\left(\frac{a_{ij}}{2R_{\text{eff}}} \right). \end{aligned} \tag{4.15}$$

We substitute the latter equation into Eq. (4.13), and we finally obtain

$$\Delta E(\boldsymbol{d}) = 8\pi Gm^2 \sum_{i,j=1}^{N} \left(\frac{\operatorname{erf}\left(\frac{r_{ij}}{2R_{\text{eff}}} \right)}{r_{ij}} - \frac{\operatorname{erf}\left(\frac{|\boldsymbol{d}-\boldsymbol{r}_{ij}|}{2R_{\text{eff}}} \right)}{|\boldsymbol{d}-\boldsymbol{r}_{ij}|} \right), \tag{4.16}$$

with $r_{ij} = |\boldsymbol{r}_{ij}|$.

4.2.2 Analytic solution of the equation for the center of mass

We want now to compute the analytic solution of the ME for the CM. We assume that the system's CM is free (i.e. $\hat{H}_{\text{CM}} = \hat{\boldsymbol{p}}^2/2M$, with $M = \sum_i m_i$). We will show in the next Subsection that, for suitably short times and large superposition distances, one can neglect the Hamiltonian contribution to the dynamics ($\hat{H}_{\text{CM}} \to 0$).

To solve the ME for the CM, it is convenient to introduce the characteristic function χ [110, 111], which is defined as

$$\chi(\boldsymbol{\nu}, \boldsymbol{\mu}, t) = \operatorname{Tr}\left[\hat{\rho}_{\text{CM}}(t) e^{\frac{i}{\hbar}(\boldsymbol{\nu}\cdot\hat{\boldsymbol{x}} + \boldsymbol{\mu}\cdot\hat{\boldsymbol{p}})} \right]. \tag{4.17}$$

Thus, given the ME in Eq. (4.9) for a free particle, one finds that the characteristic function satisfies the following equation

$$\frac{\mathrm{d}}{\mathrm{d}t}\chi(\boldsymbol{\nu}, \boldsymbol{\mu}, t) = \frac{1}{M}\boldsymbol{\nu} \cdot \nabla_{\boldsymbol{\mu}} \chi(\boldsymbol{\nu}, \boldsymbol{\mu}, t) + \frac{1}{\hbar} \left(E(\boldsymbol{\mu}) - E(\boldsymbol{0}) \right) \chi(\boldsymbol{\nu}, \boldsymbol{\mu}, t), \tag{4.18}$$

where

$$E(\boldsymbol{\mu}) = \hbar \int \mathrm{d}\boldsymbol{p}\, F(\boldsymbol{p}) e^{i\boldsymbol{\mu}\cdot\boldsymbol{p}}. \tag{4.19}$$

The solution to Eq. (4.18) is given by [111]

$$\chi(\boldsymbol{\nu}, \boldsymbol{\mu}, t) = \chi_0(\boldsymbol{\nu}, \boldsymbol{\mu} + \boldsymbol{\nu}\tfrac{t}{M}, t) \exp\left[\tfrac{1}{\hbar}\int_0^t \mathrm{d}\tau \left(E(\boldsymbol{\mu} + \boldsymbol{\nu}\tfrac{\tau}{M}) - E(\boldsymbol{0})\right)\right], \tag{4.20}$$

where $\chi_0(\boldsymbol{\nu}, \boldsymbol{\mu}, t)$ satisfies

$$\frac{\mathrm{d}}{\mathrm{d}t}\chi_0(\boldsymbol{\nu}, \boldsymbol{\mu}, t) = \frac{1}{M}\boldsymbol{\nu}\cdot\nabla_{\boldsymbol{\mu}}\chi_0(\boldsymbol{\nu}, \boldsymbol{\mu}, t), \tag{4.21}$$

and it corresponds to the characteristic function for the Hamiltonian dynamics only, in agreement with the standard quantum mechanical predictions.

To reconstruct the matrix elements of $\hat{\rho}_{\text{CM}}(t)$, one employs [111]

$$\langle \boldsymbol{x}|\hat{\rho}_{\text{CM}}(t)|\boldsymbol{y}\rangle = \frac{1}{(2\pi\hbar)^3}\int \mathrm{d}\boldsymbol{\nu}\, e^{-\frac{i}{2\hbar}\boldsymbol{\nu}\cdot(\boldsymbol{x}+\boldsymbol{y})}\chi(\boldsymbol{\nu}, \boldsymbol{x}-\boldsymbol{y}, t). \tag{4.22}$$

We can express $\langle \boldsymbol{x}|\hat{\rho}_{\text{CM}}(t)|\boldsymbol{y}\rangle$ in terms of the matrix elements of $\hat{\rho}^{\text{QM}}_{\text{CM}}(t)$, which is the statistical operator corresponding to the quantum dynamical evolution (that related to χ_0 alone). Such a relation reads

$$\begin{aligned}\langle \boldsymbol{x}|\hat{\rho}_{\text{CM}}(t)|\boldsymbol{y}\rangle = \frac{1}{(2\pi\hbar)^3}\int \mathrm{d}\boldsymbol{\nu}\int \mathrm{d}\boldsymbol{z}\, e^{\frac{i}{\hbar}\boldsymbol{\nu}\cdot\boldsymbol{z}}\,\langle \boldsymbol{z}+\boldsymbol{x}|\hat{\rho}^{\text{QM}}_{\text{CM}}(t)|\boldsymbol{z}+\boldsymbol{y}\rangle \times \\ \times \exp\left[\tfrac{1}{\hbar}\int_0^t \mathrm{d}\tau \left(E\left(\boldsymbol{\nu}\frac{\tau}{M} + \boldsymbol{x} - \boldsymbol{y}\right) - E(\boldsymbol{0})\right)\right].\end{aligned} \tag{4.23}$$

Under the assumption that we can neglect the free evolution $\hat{H}_{\text{CM}}$, we take in the latter equation the limit as $M \to \infty$. Indeed we assumed that the system's CM is free so $\hat{H}_{\text{CM}} = \hat{\boldsymbol{p}}^2/2M$ and, as we said before, we will show in Subsection 4.2.3 that, for suitably short times and large superposition distances, one can neglect the Hamiltonian contribution to the dynamics so $\hat{H}_{\text{CM}} \to 0$ and $M \to \infty$. Then, we have $\langle \boldsymbol{z}+\boldsymbol{x}|\hat{\rho}^{\text{QM}}_{\text{CM}}(t)|\boldsymbol{z}+\boldsymbol{y}\rangle = \langle \boldsymbol{z}+\boldsymbol{x}|\hat{\rho}_{\text{CM}}(0)|\boldsymbol{z}+\boldsymbol{y}\rangle$, and Eq. (4.23) reduces to

$$\langle \boldsymbol{x}|\hat{\rho}_{\text{CM}}(t)|\boldsymbol{y}\rangle \simeq \langle \boldsymbol{x}|\hat{\rho}_{\text{CM}}(0)|\boldsymbol{y}\rangle \exp\left[-t[E(\boldsymbol{x}-\boldsymbol{y}) - E(\boldsymbol{0})]/\hbar\right], \tag{4.24}$$

which is, namely, Eq. (4.11) with $\tau(\boldsymbol{d}) = \hbar/\Delta E(\boldsymbol{d})$ and $\boldsymbol{d} = \boldsymbol{x} - \boldsymbol{y}$, where

$$\Delta E(\boldsymbol{d}) = -8\pi G\int \mathrm{d}\boldsymbol{r}\int \mathrm{d}\boldsymbol{r}'\,\frac{\mu(\boldsymbol{r})\,[\mu(\boldsymbol{r}'+\boldsymbol{d}) - \mu(\boldsymbol{r}')]}{|\boldsymbol{r}-\boldsymbol{r}'|}, \tag{4.25}$$

is exactly Eq. (4.12), and $E(\boldsymbol{d})$ is defined as in Eq. (4.19) which, using $F(\boldsymbol{p})$ defined in Eq. (4.10), takes the explicit form of

$$E(\boldsymbol{d}) = 8\pi G \sum_{i,j=1}^{N} m_i m_j \frac{\operatorname{erf}\left(\frac{|\boldsymbol{x}_i^{(0)} - \boldsymbol{x}_j^{(0)} + \boldsymbol{d}|}{2R_{\text{eff}}}\right)}{|\boldsymbol{x}_i^{(0)} - \boldsymbol{x}_j^{(0)} + \boldsymbol{d}|}, \tag{4.26}$$

which is, namely, that given in Eqs. (4.16).

4.2.3 Neglecting the free evolution $\hat{H}_{\text{CM}}$ in the Diósi-Penrose master equation

In the following, as mentioned before, we investigate the conditions under which one can safely neglect the free evolution when studying the dynamics of the CM of a system in the DP model. We aim to study what happens in a superposition of the form «here »plus «there », and we choose a superposition of two Gaussian states as they are relatively well-behaved and analytically tractable. Specifically, we focus on the matrix element of Eq. (4.23) for the case of an initial state $\psi(\boldsymbol{x}, 0)$ being in a superposition of two equal Gaussians centered in $\pm\boldsymbol{d}/2$. Hence, we have

$$\psi(\boldsymbol{x}, 0) = \frac{1}{\mathcal{N}} \left[e^{-\frac{1}{2\sigma^2}(\boldsymbol{x}-\boldsymbol{d}/2)^2} + e^{-\frac{1}{2\sigma^2}(\boldsymbol{x}+\boldsymbol{d}/2)^2} \right], \tag{4.27}$$

where

$$\mathcal{N} = \left[2(\sqrt{\pi}\sigma)^3 \left(1 + e^{-\frac{d^2}{4\sigma^2}} \right) \right]^{1/2}, \tag{4.28}$$

is the corresponding normalization constant, $d = |\boldsymbol{d}|$, and σ is the Gaussian spread. The free, quantum mechanical evolution of the CM, where $\hat{H}_{\text{CM}} = \hat{\boldsymbol{p}}^2/2M$, leads to the following expression for the state at a time t

$$\psi(\boldsymbol{x}, t) = \frac{1}{\mathcal{N}} \left(\frac{\sigma}{\sqrt{\sigma^2 + \frac{it\hbar}{M}}} \right)^3 \left(e^{-\frac{(\boldsymbol{x}+\boldsymbol{d}/2)^2}{2\left(\sigma^2 + \frac{i\hbar t}{M}\right)}} + e^{-\frac{(\boldsymbol{x}-\boldsymbol{d}/2)^2}{2\left(\sigma^2 + \frac{i\hbar t}{M}\right)}} \right). \tag{4.29}$$

We now focus on the matrix element $\langle -\boldsymbol{d}/2 | \hat{\rho}_{\text{CM}}(t) | \boldsymbol{d}/2 \rangle$, which measures the coherence between the two wave packets. Due to the spatial decoherence induced by the DP model, we expect this term to decay. Our goal is to understand under which conditions this decay factor can be computed, with negligible error, by neglecting the quantum mechanical evolution, i.e. by setting $\hat{H}_{\text{CM}} = 0$.

From Eq. (4.29), we can directly calculate the matrix element for the density operator in the standard quantum mechanical case as

$$\begin{aligned}\langle \boldsymbol{x}|\hat{\rho}^{\mathrm{QM}}_{\mathrm{CM}}(t)|\boldsymbol{y}\rangle &= \psi^*(\boldsymbol{x},t)\psi(\boldsymbol{y},t)\\ &= \frac{1}{\mathcal{N}^2}\frac{\sigma^6\left(e^{-\frac{(\boldsymbol{x}+\boldsymbol{d}/2)^2}{2\left(\sigma^2-\frac{i\hbar t}{M}\right)}}+e^{-\frac{(\boldsymbol{x}-\boldsymbol{d}/2)^2}{2\left(\sigma^2-\frac{i\hbar t}{M}\right)}}\right)\left(e^{-\frac{(\boldsymbol{y}+\boldsymbol{d}/2)^2}{2\left(\sigma^2+\frac{i\hbar t}{M}\right)}}+e^{-\frac{(\boldsymbol{y}-\boldsymbol{d}/2)^2}{2\left(\sigma^2+\frac{i\hbar t}{M}\right)}}\right)}{\left(\sigma^4+(\frac{\hbar t}{M})^2\right)^{3/2}},\end{aligned} \tag{4.30}$$

which can then be inserted in Eq. (4.23). After integrating over $\boldsymbol{z}$, we obtain

$$\langle -\boldsymbol{d}/2|\hat{\rho}_{\mathrm{CM}}(t)|\boldsymbol{d}/2\rangle = \mathcal{K}_1+\mathcal{K}_2+\mathcal{K}_3, \tag{4.31}$$

where

$$\mathcal{K}_j = \int \mathrm{d}\boldsymbol{\nu}\, e^{-\boldsymbol{\nu}^2}\mathcal{F}(\boldsymbol{d}/2,\boldsymbol{\nu})\mathcal{G}_j(\boldsymbol{d}/2,\boldsymbol{\nu}) \tag{4.32}$$

and where we defined

$$\begin{aligned}\mathcal{G}_1(\boldsymbol{d}/2,\boldsymbol{\nu}) &= 1,\\ \mathcal{G}_2(\boldsymbol{d}/2,\boldsymbol{\nu}) &= \exp\left(-\frac{d^2}{\sigma^2}\right)\exp\left(-\frac{2\hbar t}{M\sigma^2}\frac{\boldsymbol{\nu}\cdot\boldsymbol{d}}{\sqrt{1+\left(\frac{\hbar t}{M\sigma^2}\right)^2}}\right),\\ \mathcal{G}_3(\boldsymbol{d}/2,\boldsymbol{\nu}) &= \exp\left(-\frac{d^2}{4\sigma^2}\right)\exp\left(-\frac{\hbar t}{M\sigma^2}\frac{\boldsymbol{\nu}\cdot\boldsymbol{d}}{\sqrt{1+\left(\frac{\hbar t}{M\sigma^2}\right)^2}}\right)\times 2\cos\left(\frac{1}{\sigma}\frac{\boldsymbol{\nu}\cdot\boldsymbol{d}}{\sqrt{1+\left(\frac{\hbar t}{M\sigma^2}\right)^2}}\right),\\ \mathcal{F}(\boldsymbol{d}/2,\boldsymbol{\nu}) &= \frac{1}{\pi^{3/2}\mathcal{N}^2\left[1+\left(\frac{\hbar t}{M\sigma^2}\right)^2\right]^{3/2}}\times\\ &\quad\times\exp\left[\int_0^t\frac{\mathrm{d}\tau}{\hbar}\left(E\left(\boldsymbol{d}+2\sigma\frac{\tau}{t}\frac{\boldsymbol{\nu}}{\sqrt{1+\left(\frac{M\sigma^2}{\hbar t}\right)^2}}\right)-E(\boldsymbol{0})\right)\right].\end{aligned} \tag{4.33}$$

We notice that, the exponential factor in Eq. (4.32) limits the main contributions to $\mathcal{K}_j$ to the vectors $\boldsymbol{\nu}$ such that $|\boldsymbol{\nu}|\leq 1$. Moreover, for $d\gg\sigma$, we can approximate the argument in the exponential of $\mathcal{F}(\boldsymbol{d}/2,\boldsymbol{\nu})$ in Eq. (4.33) as $(E(\boldsymbol{d})-E(\boldsymbol{0}))t$, which is possible since $\boldsymbol{\nu}$ is limited. These two approximations allow to easily compute

$\mathcal{K}_j$, which read

$$\begin{aligned}
\mathcal{K}_1 &= \frac{1}{\mathcal{N}^2}\left(\frac{1}{1+\left(\frac{\hbar t}{M\sigma^2}\right)^2}\right)^{3/2} \exp\left[\left(E(\boldsymbol{d})-E(\boldsymbol{0})\right)\frac{t}{\hbar}\right], \\
\mathcal{K}_2 &= \exp\left[-\frac{d^2}{\sigma^2}\left(1-\frac{t^2\hbar^2}{M^2\sigma^4+t^2\hbar^2}\right)\right]\mathcal{K}_1, \\
\mathcal{K}_3 &= 2\exp\left(-\frac{d^2}{4\sigma^2}\frac{2M^2\sigma^4}{M^2\sigma^4+t^2\hbar^2}\right)\cos\left(\frac{M\sigma^2 t\hbar}{M^2\sigma^4+t^2\hbar^2}\frac{d^2}{2\sigma^2}\right)\mathcal{K}_1.
\end{aligned} \tag{4.34}$$

For small times, satisfying $\hbar t \ll M\sigma^2$, we see that the expressions for $\mathcal{K}_i$ reduce to

$$\begin{aligned}
\mathcal{K}_1 &= \frac{1}{\mathcal{N}^2}\exp\left[E(\boldsymbol{d})-E(\boldsymbol{0})\right)\frac{t}{\hbar}\Big], \\
\mathcal{K}_2 &= e^{-\frac{d^2}{\sigma^2}}\mathcal{K}_1, \\
\mathcal{K}_3 &= 2e^{-\frac{d^2}{2\sigma^2}}\mathcal{K}_1,
\end{aligned} \tag{4.35}$$

and therefore

$$\langle -\boldsymbol{d}/2|\hat{\rho}_{\text{CM}}(t)|\boldsymbol{d}/2\rangle = \frac{1}{\mathcal{N}^2}\left(1+e^{-\frac{d^2}{2\sigma^2}}\right)^2 \exp\left[\left(E(\boldsymbol{d})-E(\boldsymbol{0})\right)\frac{t}{\hbar}\right], \tag{4.36}$$

which is the expression that one would have obtained if the evolution due to the Hamiltonian $\hat{H}_{\text{CM}}$ is neglected. Indeed, in such a case, one has that Eq. (4.18) changes in

$$\frac{\mathrm{d}}{\mathrm{d}t}\chi(\boldsymbol{\nu},\boldsymbol{\mu},t) \simeq \frac{E(\boldsymbol{\mu})-E(\boldsymbol{0})}{\hbar}\chi(\boldsymbol{\nu},\boldsymbol{\mu},t), \tag{4.37}$$

whose trivial solution is

$$\chi(\boldsymbol{\nu},\boldsymbol{\mu},t) \simeq \chi(\boldsymbol{\nu},\boldsymbol{\mu},0)\exp\left[\frac{E(\boldsymbol{\mu})-E(\boldsymbol{0})}{\hbar}t\right]. \tag{4.38}$$

Correspondingly, Eq. (4.23) changes in

$$\langle \boldsymbol{x}|\hat{\rho}_{\text{CM}}(t)|\boldsymbol{y}\rangle \simeq \langle \boldsymbol{x}|\hat{\rho}^{\text{QM}}_{\text{CM}}(0)|\boldsymbol{y}\rangle \exp\left[\frac{E(\boldsymbol{x}-\boldsymbol{y})-E(\boldsymbol{0})}{\hbar}t\right], \tag{4.39}$$

where

$$\langle \boldsymbol{x}|\hat{\rho}^{\text{QM}}_{\text{CM}}(0)|\boldsymbol{y}\rangle = \psi^*(\boldsymbol{x},0)\psi(\boldsymbol{y},0). \tag{4.40}$$

The trivial substitution of the latter expression in Eq. (4.39), and setting $\boldsymbol{x}=-\boldsymbol{d}/2$ and $\boldsymbol{y}=\boldsymbol{d}/2$, and the use of Eq. (4.27), leads to Eq. (4.36). Thus, under the assumptions of suitably short times satisfying $\hbar t \ll M\sigma^2$ and large superposition

distances $d \gg \sigma$, we can safely neglect the evolution due to $\hat{H}_{\rm CM}$ in the Diósi-Penrose model. Since the systems we will consider in our analysis satisfy these conditions, we will be able to use the approximate expression given in Eq. (4.39), as done in Eq. (4.11).

To summarise, in this subsection we have analysed under which conditions the free center-of-mass Hamiltonian $\hat{H}_{\rm CM}$ can be neglected in the Diósi–Penrose master equation. By comparing the characteristic timescale of the unitary spreading induced by $\hat{H}_{\rm CM}$ with the localization timescale generated by the DP dissipator, we have shown that, for sufficiently massive and extended systems, the collapse dynamics dominate over the free evolution. This allows one to consistently neglect the Hamiltonian contribution when estimating the collapse time and the suppression of spatial superpositions. This approximation will be adopted in the following sections, where it significantly simplifies both the analytical and numerical treatment of the model while preserving the relevant physical behaviour.

4.3 Application

We now fix the system of interest that will be used to quantify the theoretical upper bound on R_0. Our choice is to focus on the smallest object that is visible by the human eye. In particular, we consider a single-layer graphene sheet [108], with a side length of $L = 25\,\mu$m corresponding to about the smallest space resolution of the eye [109]. For the sake of simplicity, one can take the system as having a square shape, corresponding to a total number of carbon atoms $N = 2 \times 10^{10}$. We assume that the CM of the system is prepared in a spatial superposition of two wavepackets of width σ at a superposition distance $d = |\boldsymbol{d}|$, with $\sigma \ll d$, where d has been fixed to $d = 4L = 100\,\mu$m. This value is such that the two spatial configurations are distinguishable (namely, $d > L$ and $d > \sigma$), which is the requirement to have an actual cat state. Our goal is to compute the collapse time $\tau(\boldsymbol{d}) = \hbar/\Delta E(\boldsymbol{d})$ of this superposition and require it to be shorter than the resolution time of the human eye, $\tau_{\rm obs} = 0.01\,$s [109].

We can quantify $\tau(\boldsymbol{d})$ by explicitly evaluating the sum in Eq. (4.16), which involves the calculation of the term

$$S = \sum_{i=1}^{N} \sum_{j=1}^{N} f(\boldsymbol{r}_{ij}, R_0, \mathbf{d}), \tag{4.41}$$

where i and j run across all the N lattice sites and $f(\boldsymbol{r}_{ij}, R_0, \mathbf{d})$ is a function that depends on the distance $\boldsymbol{r}_{ij}$ between the sites i and j. In this form, the evaluation of Eq. (4.41) requires the sum of N^2 terms. Given the large systems considered here ($N \sim 10^{10}$), a direct evaluation of this sum is not feasible on a personal computer or even on a dedicated computer facility. However, as we just said, since the summed terms in Eq. (4.41) depend only on the relative distance $\boldsymbol{r}_{ij}$, we can rewrite the double sum in Eq. (4.16) as a single weighted sum. Namely,

$$S = \sum_{\boldsymbol{r}\in\mathcal{D}} \omega(\boldsymbol{r}) f(\boldsymbol{r}, R_0, \boldsymbol{d}), \tag{4.42}$$

where $\omega(\boldsymbol{r})$ is the number of atoms at a distance $\boldsymbol{r}$ within the domain $\mathcal{D}$, which accounts for every possible distance among the atoms in the considered system. Consequently, the calculation is greatly simplified once the atoms are considered to be in a periodic lattice, and thus $\boldsymbol{r}$ becomes a function of primitive vectors $\boldsymbol{a}_i$ and lattice index n_i. For a two-dimensional lattice with primitive vectors $\boldsymbol{a}_1$ and $\boldsymbol{a}_2$ and respectively N_1 and N_2 sites along these directions (where $N_1 N_2 = N$), the domain is given by

$$\mathcal{D} = \{\, n_1\boldsymbol{a}_1 + n_2\boldsymbol{a}_2, \text{ where } n_i \in [-(N_i - 1), (N_i - 1)] \,\}, \tag{4.43}$$

and we make it clear that the set is not related to the number of sites, but to the number of possible distances, which is greater than the number of sites. Specifically, it is approximately twice the number of sites in each direction. The weights instead read

$$\omega(n_1, n_2) = (N_1 - |n_1|)(N_2 - |n_2|). \tag{4.44}$$

This expression takes edge effects into account. Moreover, as a check, using small values of N, it was numerically verified that Eq. (4.42) is correct by computing S using this equation and the original double sum in Eq. (4.41). The two terms being equal up to machine precision, that is, with a relative error on the order of 10^{-8}, which corresponds to the typical error when using single-precision floating-point numbers. Thus, Eq. (4.42) becomes

$$S = \sum_{n_1=-(N_1-1)}^{N_1-1} \sum_{n_2=-(N_2-1)}^{N_2-1} \omega(n_1, n_2) f(n_1\boldsymbol{a}_1 + n_2\boldsymbol{a}_2, R_0, \boldsymbol{d}), \tag{4.45}$$

which involves the sum of $(2N_1 - 1)(2N_2 - 1) \sim 4N_1N_2 = 4N$ terms. A speedup

from a quadratic to a linear scaling in N is obtained, which is significant for $N \sim 10^{10}$. To be quantitative, as shown in the next Subsection, the evaluation of the sum for $N = 2 \times 10^{10}$ takes around 5 minutes on a personal laptop by using Eq. (4.45), while it would take around 13000 centuries by using Eq. (4.41).

In the next Subsection, we derive explicitly the expressions in Eq. (4.43) and Eq. (4.44), and extend this approach to a more general lattice. The expression in Eq. (4.45), and thus $\tau(\boldsymbol{d})$, is computed numerically for different values of R_0 and N, and by accounting for the actual geometry of the graphene lattice.

4.3.1 Algorithm for the numerical calculation

In this Subsection, we develop precise calculations for our system, i.e. a plate made of a single layer of graphene. We consider a general two-dimensional lat-

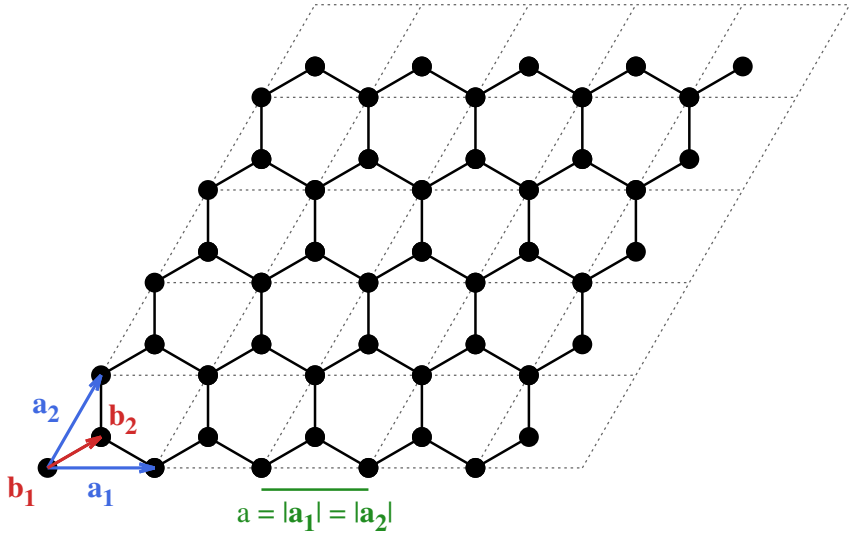

Figure 4.1: Graphical representation of the graphene lattice that was employed for the numerical summation. The lattice vectors are $\boldsymbol{a}_1 = a(1,0)$ and $\boldsymbol{a}_2 = a(\frac{1}{2}, \frac{\sqrt{3}}{2})$. For each cell, we have two carbon atoms, which are identified by $\boldsymbol{d}_1 = (0,0)$ and $\boldsymbol{d}_2 = a(\frac{1}{2}, \frac{\sqrt{3}}{6})$.

tice, with primitive vectors $\boldsymbol{a}_1$ and $\boldsymbol{a}_2$, and basis $\boldsymbol{d}_\alpha$, with $\alpha = 1, \dots, K$ being the index of the particles in the unit cell. For instance, the graphene is a two-dimensional lattice with primitive vectors $\boldsymbol{a}_1 = a\,(1,0)$, $\boldsymbol{a}_2 = a\left(\frac{1}{2}, \frac{\sqrt{3}}{2}\right)$, and basis $\boldsymbol{d}_1 = (0,0)$, $\boldsymbol{d}_2 = a\left(\frac{1}{2}, \frac{\sqrt{3}}{6}\right)$, where $a = 2.46\,\text{Å}$ is the lattice step [112] (see Figure 4.1). Each site of the lattice can be written as a linear combination of the primitive

vectors with integer coefficients, $\boldsymbol{x}_{i,\alpha} = n_1^i \boldsymbol{a}_1 + n_2^i \boldsymbol{a}_2 + \boldsymbol{d}_\alpha$, with $n_1^i, n_2^i \in \mathbb{Z}$. Therefore, also the distance between two sites can be written as a linear combination of the primitive vectors. Namely

$$\boldsymbol{r}_{ij\alpha\beta} = \boldsymbol{x}_{i,\alpha} - \boldsymbol{x}_{j,\beta} = n_1^{ij} \boldsymbol{a}_1 + n_2^{ij} \boldsymbol{a}_2 + (\boldsymbol{d}_\alpha - \boldsymbol{d}_\beta), \qquad \text{with} \quad n_1^{ij}, n_2^{ij} \in \mathbb{Z}, \tag{4.46}$$

where $n_1^{ij} = n_1^i - n_1^j$, and $n_2^{ij} = n_2^i - n_2^j$. Then, the distance between two lattice sites can be written as a function of two integers $n_1 = n_1^{ij}$, $n_2 = n_2^{ij}$ and a vector $\boldsymbol{c}_\gamma = \boldsymbol{d}_\alpha - \boldsymbol{d}_\beta$. Namely, we have

$$\boldsymbol{r}(n_1, n_2, \gamma) = n_1 \boldsymbol{a}_1 + n_2 \boldsymbol{a}_2 + \boldsymbol{c}_\gamma, \tag{4.47}$$

with $n_1, n_2 \in \mathbb{Z}$ and

$$\boldsymbol{c}_\gamma \in \mathcal{D}_b = \{ \boldsymbol{d}_\alpha - \boldsymbol{d}_\beta \mid \alpha, \beta = 1, \ldots, K \}. \tag{4.48}$$

Suppose that the lattice is finite, with N_1 and N_2 cells along the first and the second primitive vectors, respectively. In this case, the coefficients for the position of the i-th site are $n_1^i \in [0, N_1 - 1]$ and $n_2^i \in [0, N_2 - 1]$. Similarly, the coefficients that define the distance between the sites are $n_1^{ij} = (n_1^i - n_1^j) \in [-N_1 + 1, N_1 - 1]$ and $n_2^{ij} = (n_2^i - n_2^j) \in [-N_2 + 1, N_2 - 1]$. As a result, the set of all possible distances between the lattice sites is

$$\mathcal{D} = \{ \boldsymbol{r}(n_1, n_2, \gamma) \mid n_i \in [-N_i + 1, N_i - 1], \boldsymbol{c}_\gamma \in \mathcal{D}_b \}, \tag{4.49}$$

where the form of $\boldsymbol{r}(n_1, n_2, \gamma)$ is defined in Eq. (4.47).

The weights $\omega(\boldsymbol{r})$ are given by the number of pairs of lattice cells connected by the vector $\boldsymbol{r}$. The explicit value can be computed by accounting that the distance $\boldsymbol{r}(n_1, n_2, \gamma)$ links two cells that are separated by $n_i \boldsymbol{a}_i$ along the i-th direction. Since the lattice is finite, there are $N_i - |n_i|$ pairs of cells at such separation. Therefore, we have

$$\omega(n_1, n_2, \gamma) = \omega_\gamma (N_1 - |n_1|)(N_2 - |n_2|), \tag{4.50}$$

where ω_γ is the number of pairs of atoms in the same cell that are $\boldsymbol{c}_\gamma$ apart. For example, for a lattice with a single atom per unit cell there is only one basis vector $\boldsymbol{d}_1 = (0, 0)$ and only one possible (null) distance between atoms in the same cell. Thus, $\mathcal{D}_b = \{\boldsymbol{c}_1 = (0, 0)\}$ and $\omega_1 = 1$. Conversely, for the graphene plate, which is

the case of interest, one has $\boldsymbol{d}_1 = (0,0)$ and $\boldsymbol{d}_2 = a(\frac{1}{2}, \frac{\sqrt{3}}{6})$. According to Eq. (4.48), we have

$$\begin{aligned} \mathcal{D}_b &= \{\boldsymbol{c}_1 = \boldsymbol{d}_1 - \boldsymbol{d}_1, \boldsymbol{c}_2 = \boldsymbol{d}_1 - \boldsymbol{d}_2, \boldsymbol{c}_3 = \boldsymbol{d}_2 - \boldsymbol{d}_1, \boldsymbol{c}_4 = \boldsymbol{d}_2 - \boldsymbol{d}_2\}, \\ &= \{\boldsymbol{c}_1 = (0,0), \boldsymbol{c}_2 = -a(\tfrac{1}{2}, \tfrac{\sqrt{3}}{6}), \boldsymbol{c}_3 = a(\tfrac{1}{2}, \tfrac{\sqrt{3}}{6}), \boldsymbol{c}_4 = (0,0)\}. \end{aligned} \tag{4.51}$$

Since $\boldsymbol{c}_4 = \boldsymbol{c}_1$, we can neglect $\boldsymbol{c}_4$ and count twice $\boldsymbol{c}_1$. Then, we find $\omega_1 = 2$ and $\omega_2 = \omega_3 = 1$.

By considering the explicit form of the weights, Eq. (4.42) becomes

$$S = \sum_{n_1=-N_1+1}^{N_1-1} \sum_{n_2=-N_2+1}^{N_2-1} \sum_{\boldsymbol{c}_\gamma \in \mathcal{D}_b} \omega_\gamma (N_1 - |n_1|)(N_2 - |n_2|) \times f(\boldsymbol{r}(n_1, n_2, \gamma), R_0, \boldsymbol{d}). \tag{4.52}$$

Such an expression involves the sum of

$$(2N_1 - 1)(2N_2 - 1)[1 + K(K-1)] \simeq 4N_1N_2[1 + K(K-1)] = 4\frac{[1 + K(K-1)]}{K}N \tag{4.53}$$

terms, where we used that the total number of atoms is given by the product of the number of cells per direction times the number of atoms per cell, i.e. $N = N_1N_2K$. These expressions are valid for any two-dimensional lattice, and can be easily generalized to higher dimensions.

As shown by Eq. (4.53), the sum involves a number of terms that scales linearly with the number of atoms, as expected. Figure 4.2 provides the comparison of the execution time for the numerical summation when employing Eq. (4.53) (blue dots) and Eq. (4.41) (red dots), for $R_0 = 1\,\text{Å}$ and $d = 10^6\,\text{Å}$, showing the numerical advantage of Eq. (4.53). For the summation we employed a simple in-house python code with `numba` just-in-time compiler [113] on a personal laptop with Intel processor i7-8750H. We extensively verified that the results of the two sums coincide to the same value, up to the machine precision for the system with $N \leq 2 \times 10^5$ particles. Moreover, since the evaluation of Eq. (4.53) as compared to Eq. (4.41) involves approximately N additional terms, the accumulation of rounding errors during the computation renders the result obtained from Eq. (4.53) less accurate than that obtained from Eq. (4.41).

To summarise, in this subsection we have introduced the numerical algorithm used to evaluate the DP-induced energy variation $\Delta E(d)$ for extended systems.

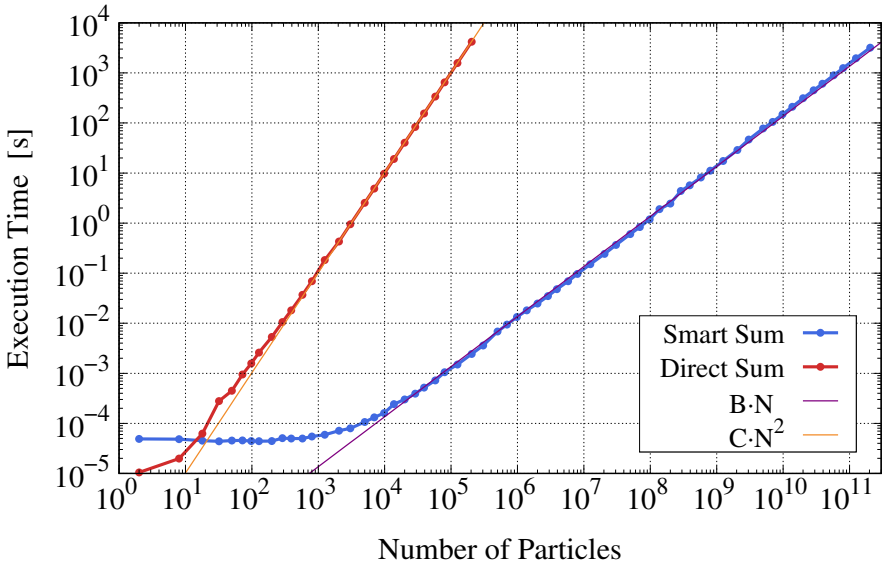

Figure 4.2: Execution time for the numerical summation as a function of the number of particles N for a plate of graphene. Each point corresponds to a single evaluation Eq. (4.53) (blue dots and fitted line) and Eq. (4.41) (red dots and fitted line). The purple and orange lines provide the scaling laws for Eq. (4.53) and Eq. (4.41), respectively.

Starting from the discretized form of the mass density, we have outlined the procedure employed to compute the gravitational self-energy difference associated with spatial superpositions at separation d. The algorithm provides a flexible framework that can be applied to different geometries and dimensionalities, and constitutes the basis for the numerical results presented in the following subsection. In particular, it allows us to systematically explore the dependence of $\Delta E(d)$ on the system parameters and to identify the emergence of characteristic regimes such as saturation plateaus.

4.3.2 Results

Figure 4.3 shows the value of $\tau(\boldsymbol{d})$, the time it takes the superposition to collapse according to the DP model, compared with the minimum human eye time resolution τ_{obs}. The gray region indicates the values of R_0 that are excluded experimentally. When $d < L$, we can observe that the collapse loses strength for all values of R_0 (the plateau in the left side), while when $R_0 > L$, the collapse becomes stronger for larger values of the superposition distance d (the increase on the right side). According to the analysis, the chosen graphene plate (corresponding to the green line $N \sim 10^{10}$) collapses on a timescale that is two orders of

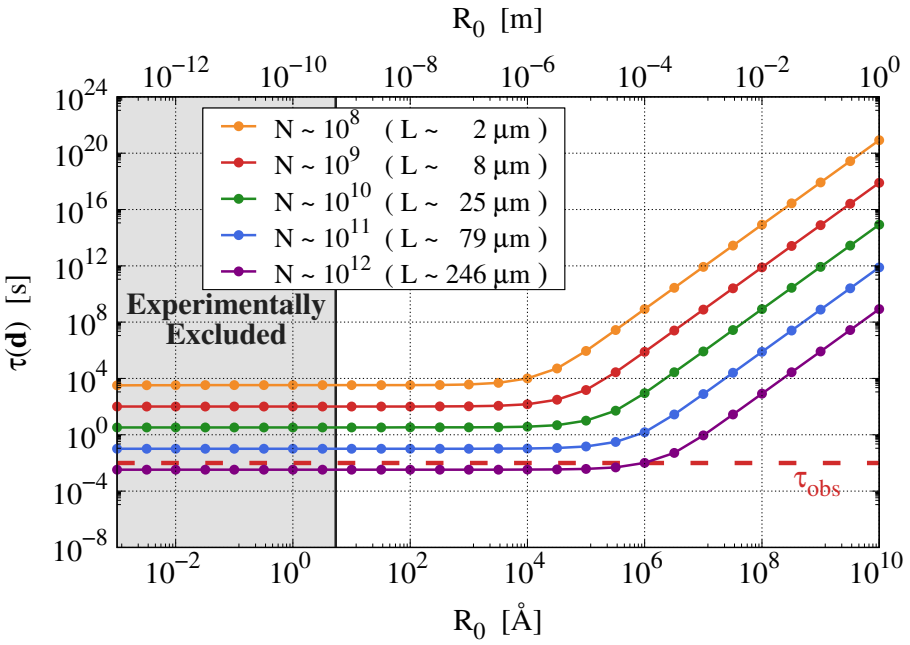

Figure 4.3: $\tau(\boldsymbol{d})$ as a function of R_0 for different sizes (equivalently, number of atoms) of a graphene square plate. The plate is assumed to be in a superposition of two localized states at a distance $|\boldsymbol{d}| = 4L$. The red dashed line indicates τ_{obs}. Values of R_0 for which $\tau(\boldsymbol{d}) > \tau_{\text{obs}}$ do not guarantee classicality. We also report the values that are currently experimentally excluded (gray shaded region) [76].

magnitude larger than τ_{obs}, for any value of R_0. This means that the model does not collapse the plate fast enough with respect to the resolution time of the human eye. The analysis also shows that, to make the collapse time shorter than τ_{obs}, one should take $\tau_{\text{obs}} \sim 3\,\text{s}$, which is clearly a too long time for requiring a macroscopic object to localize. A natural question is what happens if the superposition distance $d = |\boldsymbol{d}|$ changes. Figure 4.4 reports $\tau(\boldsymbol{d})$ for different values of d, while keeping the size of the system fixed ($L = 25\mu$m and $N = 2 \times 10^{10}$). With respect to the case studied in Fig. 4.3 where $d = 4L = 100\,\mu$m (green line in Fig. 4.4), we see that the collapse effect becomes stronger for larger values of d but only for values of $R_0 > L$. Conversely, for smaller values of d, the collapse effect loses strength for all values of R_0. In all cases, the collapse is not fast enough to occur before τ_{obs}. Therefore our result is robust against changes in the delocalization distance.

The next relevant question is how the collapse time $\tau(\boldsymbol{d})$ changes when modifying the system. We first checked what happens when increasing the size of the plate. Fig. 4.3 shows that $\tau(\boldsymbol{d})$ becomes smaller than τ_{obs} when the system length L is about ten times larger than the resolution distance of the human eye ($L = 246\,\mu$m, purple line in Fig. 4.3). In this case, we obtain an upper bound on R_0 at $10^{-4}\,\text{m}$ ($= 10^6$ Å).

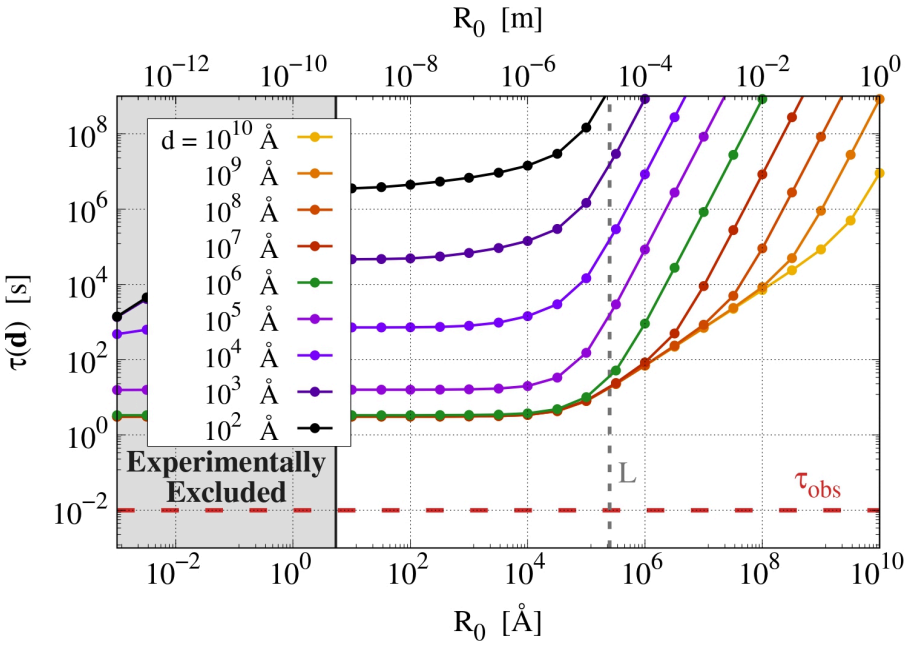

Figure 4.4: $\tau(\boldsymbol{d})$ as a function of R_0 for different values of the superposition distance d, for a graphene square plate with $N = 2 \times 10^{10}$ atoms (length $L = 25\mu$m). The value of $d = 4L = 10^6$ Å (green line) corresponds to that studied in Fig. 4.3 (green line). The gray region is excluded experimentally.

Next, we study what happens when the system has a three dimensional structure. Specifically, we consider a cubic system made of stacked layers of graphene of length L and require again that the DP dynamics collapses it on the time-scale $\tau_{\text{obs}} = 0.01$ s. The analysis is analogous to that performed in the two-dimensional case, and the results are shown in Fig. 4.5. In particular, we see that a system with $L \simeq 1\,\mu$m is sufficiently large to collapse within τ_{obs} for $R_0 \lesssim 10^3$ Å. We estimate that for an object of $L \simeq 10\,\mu$m, such as that considered in Ref. [114], the collapse takes place much faster (with $\tau(\boldsymbol{d}) \simeq 6 \times 10^{-8}$ s at the plateau) and is smaller than τ_{obs} for all values of $R_0 \lesssim 5 \times 10^6$ Å. Such an estimation is provided by analytical calculations since the numerical approach is impractical for such a large number of atoms $N \sim 10^{14}$. Specifically, we will quantify in the next Subsection the dimensionality dependence of the plateau of $\tau(\boldsymbol{d})$. We checked that the theoretical estimates match the numerical ones for smaller N.

The reason why a three-dimensional system collapses much more effectively compared to the case of a plate considered above is that, for the same length L, one has many more atoms involved, $\sim (L/a)^3$ vs $\sim (L/a)^2$, where a is the lattice step. Moreover, when taking the same number of atoms, the atoms are packed much more densely in a cube than in a plate, and this makes the collapse strength grow

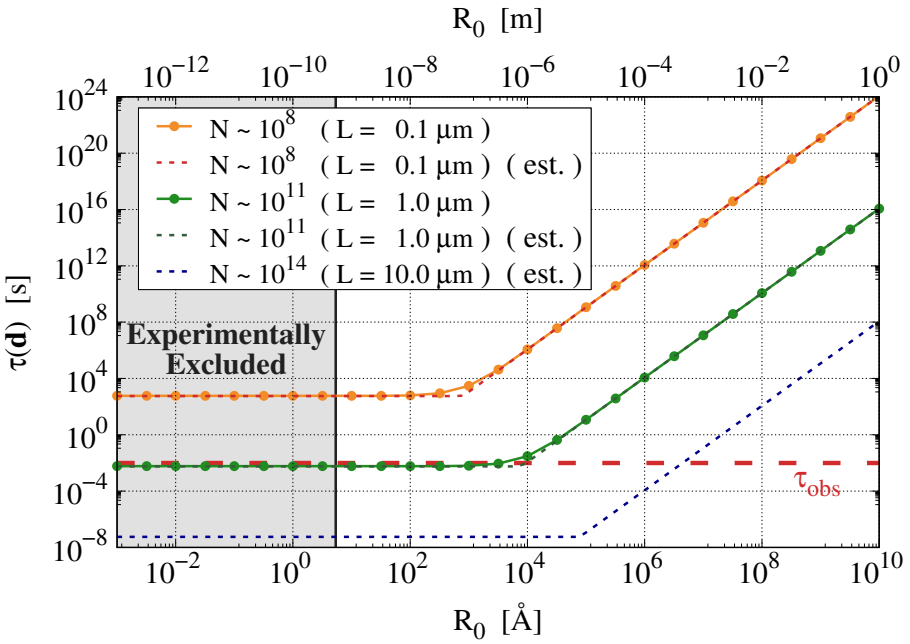

Figure 4.5: $\tau(\boldsymbol{d})$ as a function of R_0 for different numbers of atoms N (and thus length L) of a cubic graphene system in a superposition of two states at distance $|\boldsymbol{d}| = 4L$. The dashed curve provides an estimate of $\tau(\boldsymbol{d})$. The gray region is excluded experimentally.

much faster.

4.3.3 Analytical study of the behaviour of $\Delta E(\boldsymbol{d})$

We verified the numerical computation with analytical estimations of the behaviour of $\Delta E(\boldsymbol{d})$. We remind this quantity is related to the collapse time $\tau(\boldsymbol{d})$ by the relation $\tau(\boldsymbol{d}) = \hbar/\Delta E(\boldsymbol{d})$, hence to study $\Delta E(\boldsymbol{d})$ is equivalent of studying $\tau(\boldsymbol{d})$. We study the behaviour of $\Delta E(\boldsymbol{d})$ for a crystal of N atoms of mass m in the case of a two-dimensional crystal with a monoatomic square lattice with the same lattice step a, and with crystal's sides of approximately the same length L. Accordingly $L \sim \sqrt{N}a$. One can trivially generalize to the case of different length sides. Specifically, we analyze the case of a spatial superposition of the form in Eq. (4.27), where the two branches of the superposition are well separated with respect to L. Hence, the length hierarchy is given by $a \ll L \ll d$. With this setting, the vectors $\boldsymbol{r}_{ij}$ can only take discrete values, namely $\boldsymbol{r}_{ij} = a\left(n_x^i - n_x^j, n_y^i - n_y^j\right)$, where $n_k^i \in \mathbb{Z}$.

In the following, we analyse analytically the behaviour of $\Delta E(\boldsymbol{d})$ in Eq. (4.16) for different values of R_{eff}. Specifically, we provide the contributions to the sum from

the first and second term in the square bracket. Namely, these are

$$\begin{aligned} S_1 &= \sum_{i,j=1}^{N} \frac{\operatorname{erf}\left(\frac{r_{ij}}{2R_{\text{eff}}}\right)}{r_{ij}}, \\ S_2 &= \sum_{i,j=1}^{N} \frac{\operatorname{erf}\left(\frac{|\boldsymbol{d}+\boldsymbol{r}_{ij}|}{2R_{\text{eff}}}\right)}{|\boldsymbol{d}+\boldsymbol{r}_{ij}|}, \end{aligned} \tag{4.54}$$

so that $\Delta E(\boldsymbol{d}) = 8\pi G m^2 (S_1 - S_2)$. The analytical expressions will be then compared with those obtained numerically.

Analytical estimation of the first contribution to the sum S_1

The first contribution to the sum S_1 is analysed in four different intervals of interest: $R_{\text{eff}} \leq a$, $a \leq R_{\text{eff}} \leq L$, $L \leq R_{\text{eff}} \leq d$ and $d \leq R_{\text{eff}}$. We split the sum in S_1 in two contributions: the sum of the terms with $i = j$ and the sum where $i \neq j$.

When $i = j$, we have $r_{ii} = 0$ and thus the corresponding sum reads

$$\sum_{i=1}^{N} \frac{\operatorname{erf}\left(\frac{r_{ii}}{2R_{\text{eff}}}\right)}{r_{ii}} \underset{r_{ii}\to 0}{\longrightarrow} \sum_{i=1}^{N} \frac{1}{\sqrt{\pi} R_{\text{eff}}}, \tag{4.55}$$

and we have

$$S_1 = \frac{N}{\sqrt{\pi} R_{\text{eff}}} + \sum_{\substack{i,j=1 \\ i\neq j}}^{N} \frac{\operatorname{erf}\left(\frac{r_{ij}}{2R_{\text{eff}}}\right)}{r_{ij}}, \tag{4.56}$$

which we will study below.

First interval: $R_{\text{eff}} \leq a$

Consider the case $R_{\text{eff}} \leq a$. For all terms with $i \neq j$, we have that $r_{ij} \geq a$. Indeed, the minimal value of $r_{ij} = a$ is attained for the first nearest neighbor atoms. This implies $R_{\text{eff}} \leq r_{ij}$. In particular, we can divide the contributions to the sum in two cases

$$\begin{cases} \text{for } 1 \leq \frac{r_{ij}}{R_{\text{eff}}} \leq 4, & \frac{1}{2} < \operatorname{erf}\left(\frac{r_{ij}}{2R_{\text{eff}}}\right) < 1, \\ \text{for } 4 \leq \frac{r_{ij}}{R_{\text{eff}}}, & \operatorname{erf}\left(\frac{r_{ij}}{2R_{\text{eff}}}\right) \sim 1. \end{cases} \tag{4.57}$$

Since $R_{\text{eff}} \leq a$, the error function rapidly saturates to unity already at interatomic distances. As a result, except for a negligible fraction of nearest–neighbour pairs,

all terms in the sum contribute with approximately the same weight. This allows us to bound the sum by treating the distance–dependent factor as constant. The associated error scales as $O(N)$, while the total sum scales as $O(N^2)$. We can then employ these to set an upper and lower bound on the sum by approximating that all the terms weight the same independently of the value of r_{ij}. We have then

$$\sum_{\substack{i,j=1\\ i\neq j}}^{N} \frac{1}{2}\frac{1}{r_{ij}} \leq \sum_{\substack{i,j=1\\ i\neq j}}^{N} \frac{\operatorname{erf}\left(\frac{r_{ij}}{2R_{\text{eff}}}\right)}{r_{ij}} \leq \sum_{\substack{i,j=1\\ i\neq j}}^{N} \frac{1}{r_{ij}}. \tag{4.58}$$

Then, both limits depend on the same sum, which can be rewritten as

$$\sum_{\substack{i,j=1\\ i\neq j}}^{N} \frac{1}{r_{ij}} = \sum_{\substack{i,j=1\\ i\neq j}}^{N} \frac{1}{a\sqrt{(n_x^i - n_x^j)^2 + (n_y^i - n_y^j)^2}}, \tag{4.59}$$

where $n_k^i \in [-\sqrt{N}/2, \sqrt{N}/2]$. We first fix the i-th particle as that at the center of the lattice with $n_x^i = n_y^i = 0$ and sum over j. This term provides an upper bound on the other contributions of the i-sum, since fixing the i-th atom to any other in the lattice would provide a smaller contribution. Then, the corresponding vector $\boldsymbol{r}_{ij} = a(-n_x^j, -n_y^j)$ has a length of $r_{ij} = a\sqrt{(n_x^j)^2 + (n_y^j)^2}$. We obtain

$$\sum_{\substack{i,j=1\\ i\neq j}}^{N} \frac{1}{r_{ij}} \leq \sum_{i=1}^{N} \sum_{\substack{n_x^j, n_y^j = -\sqrt{N}/2\\ (n_x^j, n_y^j)\neq(0,0)}}^{\sqrt{N}/2} \frac{1}{a\sqrt{(n_x^j)^2 + (n_y^j)^2}} = \frac{N}{a} \sum_{\substack{n_x^j, n_y^j = -\sqrt{N}/2\\ (n_x^j, n_y^j)\neq(0,0)}}^{\sqrt{N}/2} \frac{1}{\sqrt{(n_x^j)^2 + (n_y^j)^2}}. \tag{4.60}$$

The contribution on right hand side of Eq. (4.60) can be approximated with the following integral

$$\frac{N}{a} \int_{-\sqrt{N}/2}^{\sqrt{N}/2} \mathrm{d}x \int_{-\sqrt{N}/2}^{\sqrt{N}/2} \mathrm{d}y \, \frac{1}{\sqrt{x^2 + y^2}} = \frac{\eta_+ N\sqrt{N}}{a}, \tag{4.61}$$

where $\eta_+ = 2\ln(3 + 2\sqrt{2}) \simeq 3.5$.

Similarly, if we fix the i-th atom to the corner of the lattice, we provide a lower bound. The corresponding vector $\boldsymbol{r}_{ij} = a(-\sqrt{N}/2 - n_x^j, -\sqrt{N}/2 - n_y^j)$ has a length

of $r_{ij} = a\sqrt{(\sqrt{N}/2 + n_x^j)^2 + (\sqrt{N}/2 + n_y^j)^2}$. Thus, we have

$$\sum_{\substack{i,j=1 \\ i\neq j}}^{N} \frac{1}{r_{ij}} \geq \sum_{i=1}^{N} \sum_{\substack{n_x^j, n_y^j = -\sqrt{N}/2 \\ (n_x^j, n_y^j) \neq (0,0)}}^{\sqrt{N}/2} \frac{1}{a\sqrt{(\sqrt{N}/2 + n_x^j)^2 + (\sqrt{N}/2 + n_y^j)^2}}. \tag{4.62}$$

Similarly as done before, we can approximate the sum to an integral, which reads

$$\frac{N}{a} \int_{-\sqrt{N}/2}^{\sqrt{N}/2} \mathrm{d}x \int_{-\sqrt{N}/2}^{\sqrt{N}/2} \mathrm{d}y \, \frac{1}{\sqrt{(\sqrt{N}/2 + x)^2 + (\sqrt{N}/2 + y)^2}} = \frac{2\eta_- N\sqrt{N}}{a}, \tag{4.63}$$

where $\eta_- = \operatorname{arcsinh}(1) \simeq 0.9$. By merging the inequality in Eq. (4.58) with those in Eq. (4.60) and Eq. (4.62), we find the bounds on Eq. (4.56) being

$$\frac{N}{\sqrt{\pi} R_{\text{eff}}} + \frac{\eta_- N\sqrt{N}}{a} \leq S_1 \leq \frac{N}{\sqrt{\pi} R_{\text{eff}}} + \frac{\eta_+ N\sqrt{N}}{a}. \tag{4.64}$$

Specifically, for

$$R_{\text{eff}} \lesssim \frac{a}{\eta_+ \sqrt{\pi N}}, \tag{4.65}$$

the first contribution is stronger and corresponds to a behaviour going as $\sim R_{\text{eff}}^{-1}$. Conversely, for larger values of R_{eff} (but still within the first interval, $R_{\text{eff}} < a$), the first term in Eq. (4.64) is negligible with respect to the second one, which is independent from R_{eff}.

Second interval: $a \leq R_{\text{eff}} \leq L$

In the second interval, $a \leq R_{\text{eff}} \leq L$, we have that r_{ij} can be comparable with R_{eff}. Namely, for $i \neq j$, we have $a \leq r_{ij} \leq \sqrt{2}L$. Due to the comparable interval of r_{ij} and R_{eff}, we have several edge effects that make the analytical estimation more difficult. One can approximate fairly enough the error function to

$$\operatorname{erf}\left(\frac{x}{2}\right) \simeq \begin{cases} \frac{x}{\sqrt{\pi}}, & x \leq 2, \\ 1, & x \geq 2. \end{cases} \tag{4.66}$$

The piecewise approximation in Eq. (4.66) is justified in the regime $a \leq R_{\text{eff}} \leq L$, where the smearing length is larger than the lattice spacing, and the error function varies smoothly over interatomic distances. Since the number of contributing

pairs is dominated by separations $r_{ij} \gg R_{\text{eff}}$, the precise shape of the crossover region around $r_{ij} \simeq 2R_{\text{eff}}$ has a negligible impact on the overall sum. The approximation therefore, captures the correct scaling and provides reliable bounds up to numerical factors of order unity. Based on all this, we divide the sum in terms for which $r_{ij} \leq 2R_{\text{eff}}$ and terms for which $r_{ij} \geq 2R_{\text{eff}}$.

For $r_{ij} \leq 2R_{\text{eff}}$,

$$\frac{\operatorname{erf}\left(\frac{r_{ij}}{2R_{\text{eff}}}\right)}{r_{ij}} \simeq \frac{1}{\sqrt{\pi}R_{\text{eff}}}, \tag{4.67}$$

and, given the i-th atom, there are roughly $(2R_{\text{eff}}/a)^2$ atoms j that are at most at a distance $2R_{\text{eff}}$. Thus, the contribution to the second term in Eq. (4.56) for $r_{ij} \leq 2R_{\text{eff}}$ can be evaluated to

$$\sum_{\substack{i,j=1 \\ i\neq j,\, r_{ij}\leq 2R_{\text{eff}}}}^{N} \frac{\operatorname{erf}\left(\frac{r_{ij}}{2R_{\text{eff}}}\right)}{r_{ij}} \simeq N \times \left(\frac{2R_{\text{eff}}}{a}\right)^2 \frac{1}{\sqrt{\pi}R_{\text{eff}}} = 4N\frac{R_{\text{eff}}}{\sqrt{\pi}a^2}. \tag{4.68}$$

For $r_{ij} \geq 2R_{\text{eff}}$,

$$\frac{\operatorname{erf}\left(\frac{r_{ij}}{2R_{\text{eff}}}\right)}{r_{ij}} \simeq \frac{1}{r_{ij}}. \tag{4.69}$$

Then, the corresponding contribution to the sum can be rewritten as

$$\sum_{\substack{i,j=1 \\ i\neq j,\, r_{ij}\geq 2R_{\text{eff}}}}^{N} \frac{\operatorname{erf}\left(\frac{r_{ij}}{2R_{\text{eff}}}\right)}{r_{ij}} \simeq \sum_{\substack{i,j=1 \\ i\neq j}}^{N} \frac{1}{r_{ij}} - \sum_{\substack{i,j=1 \\ i\neq j,\, r_{ij}\leq 2R_{\text{eff}}}}^{N} \frac{1}{r_{ij}}, \tag{4.70}$$

where the upper and lower bounds to the first sum are respectively given by Eq. (4.60) and Eq. (4.62). Also the second term can be bounded. A lower bound is given by setting all the r_{ij} to the maximum distance being $2R_{\text{eff}}$, namely

$$\sum_{\substack{i,j=1 \\ i\neq j,\, r_{ij}\leq 2R_{\text{eff}}}}^{N} \frac{1}{r_{ij}} \geq \sum_{\substack{i,j=1 \\ i\neq j,\, r_{ij}\leq 2R_{\text{eff}}}}^{N} \frac{1}{2R_{\text{eff}}} = N \times \left(\frac{2R_{\text{eff}}}{a}\right)^2 \frac{1}{2R_{\text{eff}}} = \frac{4NR_{\text{eff}}}{a^2}. \tag{4.71}$$

An upper bound is instead obtained by fixing the i-th atom to the center of the lattice, and approximating the sum over j to an integral in spherical coordinates.

Namely,

$$\sum_{\substack{i,j=1\\ i\neq j,\, r_{ij}\leq 2R_{\text{eff}}}}^{N} \frac{1}{r_{ij}} \leq \frac{2\pi N}{a}\mathcal{F}_G \int_1^{\frac{2R_{\text{eff}}}{a}} \mathrm{d}r = \frac{2\pi N}{a}\mathcal{F}_G\left(\frac{2R_{\text{eff}}}{a}-1\right), \tag{4.72}$$

where $\mathcal{F}_G$ is a geometrical factor accounting for couples of atoms (i,j) that are counted in the sum but do not pertain to the lattice (indeed, one can have that $2R_{\text{eff}} = L \geq \sqrt{2}L$ being the maximum distance r_{ij}), and accounts for the ratio of the area of a square lattice of length $2R_{\text{eff}}$ with the span of the considered r_{ij}, namely that of a planar toric lattice of internal radius a and external radius $2R_{\text{eff}}$:

$$\mathcal{F}_G = \frac{L^2}{L^2 + 4LR_{\text{eff}} + \pi R_{\text{eff}}^2}\frac{4R_{\text{eff}}^2}{\pi(4R_{\text{eff}}^2 - a^2)}. \tag{4.73}$$

By summing the contributions from Eq. (4.68) and Eq. (4.70), we find that Eq. (4.56) is bounded as follows

$$\begin{aligned}\frac{N}{\sqrt{\pi}R_{\text{eff}}} + \frac{\eta_- N\sqrt{N}}{a} + \frac{4NR_{\text{eff}}}{\sqrt{\pi}a^2} - \frac{2\pi N}{a}\mathcal{F}_G\left(\frac{2R_{\text{eff}}}{a}-1\right) \leq S_1 \leq \\ \leq \frac{N}{\sqrt{\pi}R_{\text{eff}}} + \frac{\eta_+ N\sqrt{N}}{a} + \frac{4NR_{\text{eff}}}{a^2}\left(\frac{1}{\sqrt{\pi}}-1\right).\end{aligned} \tag{4.74}$$

Specifically, for small values of $R_{\text{eff}} \gtrsim a$ the main contribution comes from the second term, i.e. $\eta_\pm N\sqrt{N}/a$, being independent from R_{eff}. For large values of $R_{\text{eff}} \lesssim L$, the third and fourth terms become the dominant ones. In particular, a change in the R_{eff} dependence of S_1 appears from values of

$$R_{\text{eff}} \gtrsim \frac{\eta_\pm N\sqrt{N\pi}a}{4}. \tag{4.75}$$

Third interval: $L \leq R_{\text{eff}} \leq d$

In this regime $r_{ij} \leq R_{\text{eff}}$ for $r_{ij} \leq L$. However, one also has distances such that $L \leq r_{ij} \leq \sqrt{2}L$ for which one can have $r_{ij} \geq R_{\text{eff}}$. Nevertheless, we have that $\sqrt{2}L < L \leq 2R_{\text{eff}}$, which implies that $r_{ij} \leq \sqrt{2}L < 2R_{\text{eff}}$. Consequently, we can employ the small distance approximation in Eq. (4.66) for all r_{ij}, and Eq. (4.56) becomes

$$S_1 \simeq \frac{N}{\sqrt{\pi}R_{\text{eff}}} + \sum_{\substack{i,j=1\\ i\neq j}}^{N}\frac{1}{\sqrt{\pi}R_{\text{eff}}}, \tag{4.76}$$

where there are $N(N-1)$ terms in the sum. This gives

$$S_1 \simeq \frac{N^2}{\sqrt{\pi} R_{\text{eff}}}, \tag{4.77}$$

whose behaviour with respect to R_{eff} is the same in the entire interval.

Fourth interval: $d \leq R_{\text{eff}}$

For the last interval, similar considerations are applied and the terms of the sum are approximated to their small distance limit. Consequently, we obtain

$$S_1 \simeq \frac{N^2}{\sqrt{\pi} R_{\text{eff}}}, \tag{4.78}$$

exactly as in the third interval.

Analytical estimation of the second contribution to the sum S_2

For the second contribution to the sum [cf. Eq. (4.54)], one needs to compare R_{eff} with $|\boldsymbol{d} + \boldsymbol{r}_{ij}|$. Considering $|\boldsymbol{d}| > L$, we have the following bounds on $|\boldsymbol{d} + \boldsymbol{r}_{ij}|$:

$$d - L \leq |\boldsymbol{d} + \boldsymbol{r}_{ij}| \leq d + L, \tag{4.79}$$

The second contribution is analysed in three different intervals of interest: $R_{\text{eff}} \leq (d-L)/2$, $(d-L)/2 \leq R_{\text{eff}} \leq (d+L)/2$, and $(d+L)/2 \leq R_{\text{eff}}$.

First interval: $R_{\text{eff}} \leq (d-L)/2$

In this interval, we have $R_{\text{eff}} \leq (d-L)/2 \leq |\boldsymbol{d} + \boldsymbol{r}_{ij}|/2$. Thus, we can safely apply the long distance approximation in Eq. (4.66) to S_2 in Eq. (4.54), thus obtaining

$$S_2 \simeq \sum_{i,j=1}^{N} \frac{1}{|\boldsymbol{d} + \boldsymbol{r}_{ij}|}. \tag{4.80}$$

By applying the bounds in Eq. (4.79), we can derive an upper and lower bound to S_2, which read

$$\frac{N^2}{d+L} \leq S_2 \leq \frac{N^2}{d-L}, \tag{4.81}$$

where the N^2 factor follows trivially.

Second interval: $(d-L)/2 \leq R_{\text{eff}} \leq (d+L)/2$

In the second interval, $(d-L)/2 \leq R_{\text{eff}} \leq (d+L)/2$. Thus, by combining the definition of the interval with Eq. (4.79), we obtain

$$\frac{d-L}{d+L} \leq \frac{|\boldsymbol{d}+\boldsymbol{r}_{ij}|}{2R_{\text{eff}}} \leq \frac{d+L}{d-L}. \tag{4.82}$$

Since the terms of the sum in S_2 are monotonically decreasing with respect to $\frac{|\boldsymbol{d}+\boldsymbol{r}_{ij}|}{2R_{\text{eff}}}$, for each of them we have

$$\frac{1}{2R_{\text{eff}}} \frac{\operatorname{erf}\left(\frac{d+L}{d-L}\right)}{\frac{d+L}{d-L}} \leq \frac{\operatorname{erf}\left(\frac{|\boldsymbol{d}+\boldsymbol{r}_{ij}|}{2R_{\text{eff}}}\right)}{|\boldsymbol{d}+\boldsymbol{r}_{ij}|} \leq \frac{1}{2R_{\text{eff}}} \frac{\operatorname{erf}\left(\frac{d-L}{d+L}\right)}{\frac{d-L}{d+L}}. \tag{4.83}$$

It follows that

$$\frac{\epsilon_- N^2}{2R_{\text{eff}}} \leq S_2 \leq \frac{\epsilon_+ N^2}{2R_{\text{eff}}}, \tag{4.84}$$

where

$$\epsilon_\pm = \frac{\operatorname{erf}\left[\left(\frac{d-L}{d+2L}\right)^{\pm 1}\right]}{\left(\frac{d-L}{d+2L}\right)^{\pm 1}}, \tag{4.85}$$

which can be quantified once fixed the ratio between L and d. For example, for $d = 4L$, we have $\epsilon_- \simeq 0.5$ and $\epsilon_+ \simeq 1$.

Third interval: $(d+L)/2 \leq R_{\text{eff}}$

In this interval, $R_{\text{eff}} \geq (d+L)/2 \geq |\boldsymbol{d}+\boldsymbol{r}_{ij}|/2$. So we can apply the short distance approximation in Eq. (4.66), which trivially gives

$$S_2 \simeq \frac{N^2}{\sqrt{\pi} R_{\text{eff}}}. \tag{4.86}$$

Both contributions

The sum of the two contributions to $\Delta E(\boldsymbol{d}) = 8\pi G m^2 (S_1 - S_2)$ can be computed case by case depending on the value of R_{eff} compared to the other lengths involved. There are a total of six different intervals. Notably, when bounds are involved, one should account that $\min(\Delta E(\boldsymbol{d})) = 8\pi G m^2 (\min(S_1) - \max(S_2))$ and $\max(\Delta E(\boldsymbol{d})) = 8\pi G m^2 (\max(S_1) - \min(S_2))$. The intervals and the corresponding equations to be used are reported in Tab. 4.1. In particular, for $(d+L)/2 \leq R_{\text{eff}} \leq d$ and $d \leq R_{\text{eff}}$, we have that the dominant contributions cancel, namely $S_1 - S_2 \simeq 0$.

For these intervals, one needs to consider also second order terms of the expansion. These give

$$\Delta E(\boldsymbol{d}) \simeq 8\pi G m^2 \sum_{i,j=1}^{N} \left(-\frac{r_{ij}^2}{12\sqrt{\pi} R_{\text{eff}}^3} + \frac{|\boldsymbol{d} + \boldsymbol{r}_{ij}|^2}{12\sqrt{\pi} R_{\text{eff}}^3} \right) = \frac{2}{3}\sqrt{\pi} G m^2 \sum_{i,j=1}^{N} \frac{d^2 + 2\, \boldsymbol{r}_{ij} \cdot \boldsymbol{d}}{R_{\text{eff}}^3}. \tag{4.87}$$

However, since $\boldsymbol{r}_{ij} = -\boldsymbol{r}_{ji}$ for all i and j, then $\sum_{i,j=1}^{N} \boldsymbol{r}_{ij} = 0$, and one obtains

$$\Delta E(\boldsymbol{d}) \simeq \frac{2}{3}\sqrt{\pi} G m^2 N^2 \frac{d^2}{R_{\text{eff}}^3}. \tag{4.88}$$

Table 4.1 summarises the analytical study of $\Delta E(\boldsymbol{d})$, which is graphically reported in Fig. 4.6, where it was compared with the numerical evaluation of the sum. Finally, a last comment is due: $\Delta E(\boldsymbol{d})$ is a monotonically decreasing function of R_{eff}, and this can be employed to estimate its values in those intervals where an analytical estimation is hard to obtain. In particular, we exploited this for R_{eff} just below L and around $(d - L)/2$, to approximate the behaviour of $\Delta E(\boldsymbol{d})$ with the black dashed line in Fig. 4.6.

To summarise, in this subsection we have provided an analytical understanding of the behaviour of $\Delta E(d)$ observed in the numerical analysis. By studying the asymptotic limits of small and large separations, we have shown that the DP energy variation initially grows with d and eventually reaches a saturation value, giving rise to the plateau structure observed numerically. The analytical expressions derived here clarify the physical origin of this behaviour and make explicit the role played by the system geometry and mass distribution. These results not only validate the numerical findings but also provide a transparent interpretation of the relevant length scales governing the collapse dynamics.

4.3.4 Plateau dependence on the dimensionality

Here, we quantify the dimensionality dependence of the plateau of $\tau(\boldsymbol{d})$, and thus $\Delta E(\boldsymbol{d})$, for $R_{\text{eff}} \sim a$. The reason for choosing this value is that it is of the order of the current lower bounds on R_0 given by radiation emission from Germanium experiments [76, 78] (note that for both protons and nucleons $R_{\text{eff}} \simeq R_0$ when R_0 is of order of Å or larger). For the sake of simplicity, we assume our system to be a sphere in $D \geq 2$ dimensions. Namely, this corresponds to a disk for $D = 2$ and a sphere for $D = 3$ both of radius $L/2$. For $R_{\text{eff}} \sim a$, S_2 can be safely bounded

Interval for R_{eff}	**Value or bounds on $\dfrac{\Delta E(\boldsymbol{d})}{8\pi G m^2} = S_1 - S_2 = \Delta S$**
$R_{\text{eff}} \leq a$	$\dfrac{N}{\sqrt{\pi}R_{\text{eff}}} + \dfrac{\eta_- N\sqrt{N}}{a} - \dfrac{N^2}{d-L} \leq \Delta S \leq \dfrac{N}{\sqrt{\pi}R_{\text{eff}}} + \dfrac{\eta_+ N\sqrt{N}}{a} - \dfrac{N^2}{d+L}$
$a \leq R_{\text{eff}} \leq L$	$\dfrac{N}{\sqrt{\pi}R_{\text{eff}}} + \dfrac{\eta_- N\sqrt{N}}{a} - \dfrac{N^2}{d-L} + \dfrac{4NR_{\text{eff}}}{\sqrt{\pi}a^2} - \dfrac{2\pi N}{a}\mathcal{F}_G\left(\frac{2R_{\text{eff}}}{a} - 1\right) \leq \Delta S \leq \dfrac{N}{\sqrt{\pi}R_{\text{eff}}} + \dfrac{\eta_+ N\sqrt{N}}{a} - \dfrac{N^2}{d+L} + \dfrac{4NR_{\text{eff}}}{a^2}\left(\frac{1}{\sqrt{\pi}} - 1\right)$
$L \leq R_{\text{eff}} \leq \frac{d-L}{2}$	$\dfrac{N^2}{\sqrt{\pi}R_{\text{eff}}} - \dfrac{N^2}{d-L} \leq \Delta S \leq \dfrac{N^2}{\sqrt{\pi}R_{\text{eff}}} - \dfrac{N^2}{d+2L}$
$\frac{d-L}{2} \leq R_{\text{eff}} \leq \frac{d+2L}{2}$	$\dfrac{N^2}{\sqrt{\pi}R_{\text{eff}}} - \dfrac{\epsilon_+ N^2}{2R_{\text{eff}}} \leq \Delta S \leq \dfrac{N^2}{\sqrt{\pi}R_{\text{eff}}} - \dfrac{\epsilon_- N^2}{2R_{\text{eff}}}$
$\frac{d+2L}{2} \leq R_{\text{eff}} \leq d$	$\Delta S = \dfrac{N^2 d^2}{12\sqrt{\pi}R_{\text{eff}}^3}$
$d \leq R_{\text{eff}}$	$\Delta S = \dfrac{N^2 d^2}{12\sqrt{\pi}R_{\text{eff}}^3}$

Table 4.1: Summary of the analytical dependence of $\Delta E(\boldsymbol{d})$ on R_{eff} across different intervals.

with Eq. (4.81), which is independent from the dimensionality of the problem and from R_{eff} as expected for the plateau. Conversely, from Eq. (4.56) we have

$$S_1 = \frac{N}{\sqrt{\pi}a} + \sum_{\substack{i,j=1 \\ i\neq j}}^{N} \frac{\operatorname{erf}\left(\frac{r_{ij}}{2a}\right)}{r_{ij}}. \tag{4.89}$$

Since, independently from the dimensionality of the problem, Eq. (4.58) still holds, one only needs to evaluate

$$\sum_{\substack{i,j=1 \\ i\neq j}}^{N} \frac{1}{r_{ij}} = \sum_{\substack{i,j=1 \\ i\neq j}}^{N} \frac{1}{a\left(\sum_{k=1}^{D}(n_k^i - n_k^j)^2\right)^{\frac{1}{2}}}. \tag{4.90}$$

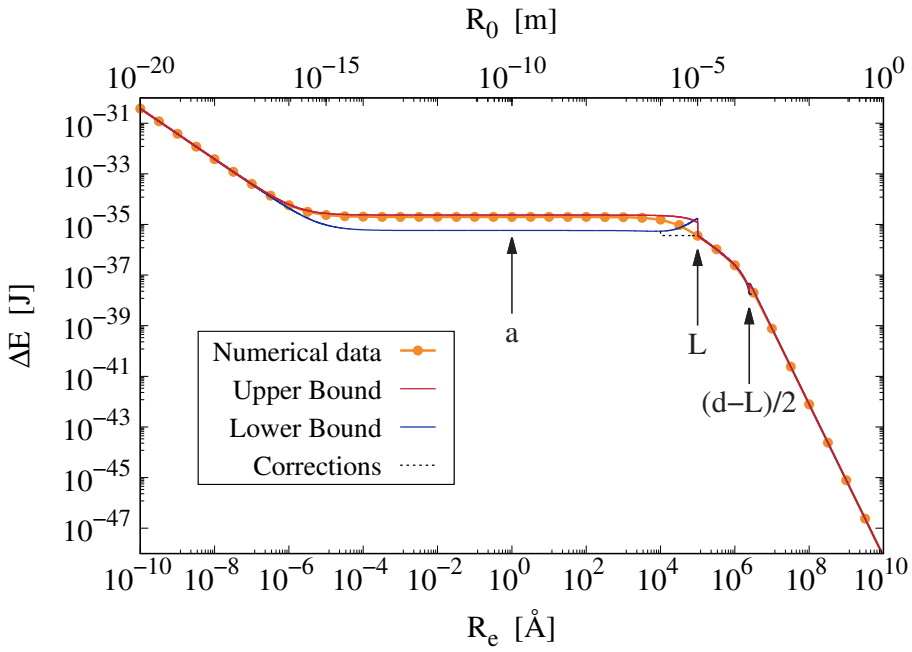

Figure 4.6: Analytical upper (red line) and lower (blue line) bounds for ΔE as a function of R_{eff}. For comparison, we reported the exact values computed numerically (orange dots). The dashed black line provides a better estimation of the lower bound for values of $R_{\text{eff}} \simeq L$ and $(d-L)/2$ by exploiting the monotonicity of $\Delta E(\boldsymbol{d})$. The vertical arrows correspond to the values of R_{eff} equal to a, L, and $(d-L)/2$ (from left to right). An inset zooms into the plateau region to highlight the tightness of the analytical bounds around the numerical values. The values of the parameters are: $a = 1.0\,\text{Å}$, $N = 10^{10}$, $L = 10^5\,\text{Å}$ and $d = 50L = 5 \times 10^6\,\text{Å}$.

By following the reasoning described above, we estimate the latter with its upper bound (see Eq. (4.60), which provided a very good estimate for S_1 for $R_{\text{eff}} \simeq a$):

$$\sum_{\substack{i,j=1 \\ i\neq j}}^{N} \frac{1}{r_{ij}} \lesssim \frac{N}{a} \sum_{\{n_k^j\}_{k=1}^{D} \in S_D} \frac{1}{\left(\sum_{k=1}^{D} (n_k^j)^2\right)^{\frac{1}{2}}}. \tag{4.91}$$

This is the generalization of Eq. (4.60) to D dimensions, with

$$S_D = \{\, n_k^j \mid 0 < |\, a(n_1^j, \ldots, n_D^j)| < L/2 \,\}\,, \tag{4.92}$$

identifying a D-dimensional sphere on which the lattice is defined. Such an expression can be simply approximated to a $1/r$ integral in D dimensions, i.e.

$$\frac{N}{a}\Omega_D \int_0^{N_D/2} \mathrm{d}x\, x^{D-1} \frac{1}{x} = \frac{N}{a} \frac{2\pi^{D/2}}{\Gamma(D/2)} \frac{N^{\frac{D-1}{D}}}{2^{D-1}(D-1)}, \tag{4.93}$$

where $\Omega_D = 2\pi^{D/2}/\Gamma(D/2)$ is the D-dimensional full angle. Correspondingly, for $R_{\text{eff}} \simeq a$, one obtains

$$\Delta E(\boldsymbol{d}) \simeq \frac{8\pi G m^2}{a} \frac{\pi^{D/2}}{\Gamma(D/2)} \frac{N^{\frac{2D-1}{D}}}{2^{D-2}(D-1)}, \tag{4.94}$$

which is plotted in Fig. 4.7 with the orange and purple lines for $D = 3$ and $D = 2$ dimensions respectively. For comparison, we report the numerical estimations of $\Delta E(\boldsymbol{d})$.

To summarise, here we have investigated how the saturation value of $\Delta E(d)$ depends on the effective dimensionality of the system. By comparing one, two, and three-dimensional configurations, we have shown that the existence and magnitude of the plateau are strongly influenced by dimensionality, reflecting the different scaling properties of the gravitational self-energy. To summarise, here we have investigated how the saturation value of $\Delta E(d)$ depends on the effective dimensionality of the system. By comparing one-, two-, and three-dimensional configurations, we have shown that the existence and magnitude of the plateau are strongly influenced by dimensionality, reflecting the different scaling properties of the gravitational self-energy. In particular, when specializing to realistic cases with $D = 1, 2, 3$ and fixing the same linear size L, it becomes clear that a three-dimensional object (e.g., a cube) collapses significantly faster than a two-dimensional plate or a one-dimensional line. This analysis highlights that dimensionality is not a merely technical aspect, but a crucial physical ingredient in determining the strength of the DP collapse. These results are particularly relevant when deriving bounds on the DP parameter R_0 for realistic experimental setups. This analysis highlights that dimensionality is not a merely technical aspect, but a crucial physical ingredient in determining the strength of the DP collapse. These results are particularly relevant when deriving bounds on the DP parameter R_0 for realistic experimental setups.

4.4 Non-Markovian generalizations of the DP model

As anticipated in Chapter 1, non-Markovian collapse models arise when the assumption of white noise is relaxed, leading to memory effects in the dynamics. Last, in this Section we introduce such generalizations only in the context of the

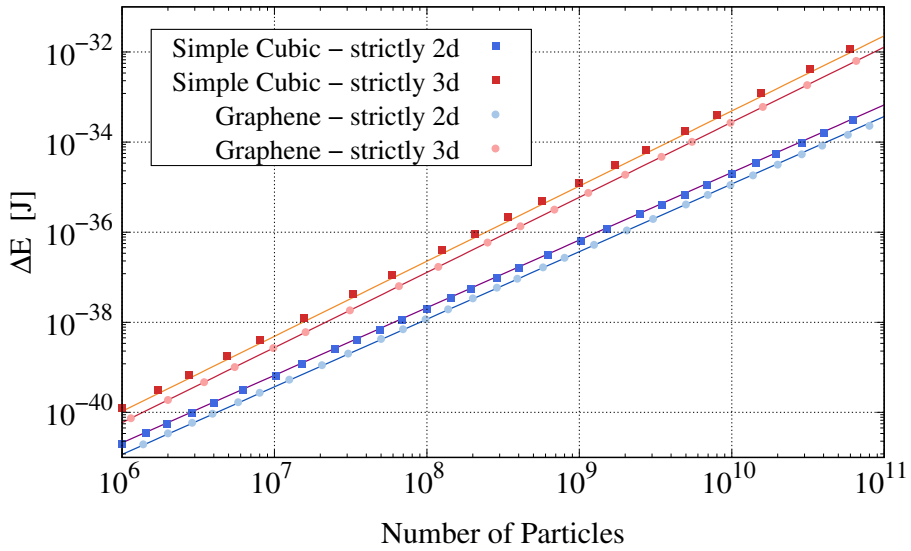

Figure 4.7: ΔE as a function of N for different two- and three-dimensional systems and comparison with the analytical behaviours. We numerically computed and compared the two- and three-dimensional cases. For the two-dimensional case, we took a sheet of graphene (blue dots) and a sheet of a material with a simple cubic lattice (blue squares). For the three dimensional case, we considered a cubic stack of graphene sheets (red dots) and a cube of material with a simple cubic lattice (red squares). The corresponding lines are obtained from Eq. (4.94) for the simple cubic lattice, while are instead fitted for the case of graphene with the same dependence from N as in Eq. (4.94). The values of the parameters are: $a = 1.0$ Å, $d = 5 \times 10^6$ Å and $m = 2.0 \times 10^{-26}$ kg for the simple cubic data and $d = 1 \times 10^6$ Å for the graphene one. In all cases, we fixed $R_{\text{eff}} = 1$ Å.

DP model, where they play a concrete physical role. We study how robust the previous analysis is with respect to physically-motivated modifications of the model. Specifically, in the standard DP model, as anticipated in Subsection 1.5.4, one assumes the noise responsible for the collapse to be white, with a Dirac-delta as the two-time correlation function. Assuming that the collapse dynamics have a physical origin, a more realistic, colored noise should be considered. The latter will be characterised by a non-trivial two-time correlation function $f(t)$. Details in the derivation of the colored collapse dynamics can be found in the literature [21, 115, 116]. Here we report the corresponding dissipator $\mathcal{D}[\hat{\rho}(t)]$ approximated to the second-order expansion in the noise, which reads

$$\mathcal{D}[\hat{\rho}_{\text{CM}}(t)] = -\frac{8\pi G}{\hbar}\int_0^t \mathrm{d}s \int \mathrm{d}\boldsymbol{r} \int \mathrm{d}\boldsymbol{r}' \frac{f(t-s)}{|\boldsymbol{r}-\boldsymbol{r}'|} \times \left[\hat{\mu}(\boldsymbol{r}'), \left[e^{\frac{i}{\hbar}\hat{H}_N(s-t)}\hat{\mu}(\boldsymbol{r})e^{-\frac{i}{\hbar}\hat{H}_N(s-t)}, \hat{\rho}_{\text{CM}}(t)\right]\right], \tag{4.95}$$

and substitutes that in Eq. (4.1). One recovers the standard DP model when $f(t-s) = \delta(t-s)$. Along the lines of the previous analysis, we can neglect the Hamiltonian evolution and we find that the CM density matrix evolves as in Eq. (4.11) with a time-dependent timescale $\tau(\boldsymbol{d}, t)$ reading

$$\tau(\boldsymbol{d}, t) = \frac{\hbar}{\Delta E(\boldsymbol{d})} \frac{t}{g(t)}, \tag{4.96}$$

where $g(t) = 2\int_0^t \mathrm{d}s \int_0^s \mathrm{d}s'\, f(s-s')$ and $\Delta E(\boldsymbol{d})$ as in Eq. (4.16).

An already considered and physically reasonable choice for the two-time correlation [117, 118] is $f(t) = \Omega_C e^{-\Omega_C |t|}/2$, which leads to

$$g(t>0) = t\left[1 - \frac{1}{\Omega_C t}\left(1 - e^{-\Omega_C t}\right)\right], \tag{4.97}$$

where the frequency cutoff Ω_C becomes a further parameter of the DP model. In the limit of $\Omega_C \to \infty$, one recovers the standard, white noise DP model, with $g(t) = t$. It is clear from Eq. (4.97) that one has $g(t) < t$ for all finite values of $\Omega_C > 0$. Consequently, the time of collapse in the colored version of the model, given by $\tau(\boldsymbol{d}, t)$ in Eq. (4.96) is always larger than that of the standard DP model. Therefore, classicality takes longer to be achieved. Although one could make different choices of $f(t)$, the physically motivated ones should decay in time and we do not expect qualitative differences in the result. In summary, including physically motivated non-Markovian effects tends to increase the collapse time $\tau(\boldsymbol{d})$.

4.5 Conclusions

The DP model finds a unique place in our efforts to understand of the quantum/gravity interplay. It proposes a path in merging the two theories, a quantum theory of gravity, by assuming that the latter is responsible for the collapse of the wave function. The model has been and is still subject to experimental verification, with different platforms. In this work we studied how effective the DP collapse is in predicting the emergence of a macroscopic classical world from an underlying quantum structure. The conclusion is that not all macroscopic objects collapse effectively, meaning that there are some objects that do not collapse within the perception time of the human eye, although they can be directly seen

by it. If its size increases by a couple of orders of magnitude in length or thickness, the collapse becomes fast enough.

Our analysis, therefore, shows that the quantum-to-classical transition in the DP model occurs roughly at the border ($10^{10} - 10^{12}$ atoms) between what we consider meso and macro. In this region, the collapse is roughly independent from R_0 for a large range of values ($1 - 10^6$ Å). This is relevant since the existence of R_0 seems artificial, and in fact, in the past, ways to removed it were proposed [25, 42, 56], which however were not successful [28, 78]. It will be interesting to see whether this boundary set by the gravitational collapse of the wavefunction is more than a coincidence.

To fully test this boundary up to $R_0 = 10^6$ Å, experiments should be considerably developed. The most promising experiments are the so-called non-interferometric ones [77], which are based on the detection of diffusive effects due to the collapse. To date, the strongest bound $R_0 \gtrsim 4\,\text{Å}$ is set by experiments searching for collapse-induced radiation emission from a Germanium crystal [76]. Since the predicted radiation emission rate is proportional to R_0^{-3}, an improvement of the bound on R_0 of six orders of magnitude (required to close the gap between experiments and theory) requires 18 orders of magnitude improvement on the sensitivity. While the expected radiation emission rate can be increased by considering photons at lower energies (order of a few keV) [119] rather than those considered in [76], it is not obvious how to fill such a large gap. Clearly, this reasoning does not hold if one rigidly focuses on the plate configuration; in that case, the model would already be ruled out. If, instead, as suggested by Penrose himself [56], one relaxes the requirement to consider a three-dimensional object, the corresponding bound shifts by approximately six orders of magnitude. Notably, a preprint work by Aprile et al. [98] improves the bound on R_0 by five orders of magnitude, leading to $R_0 > 4.5 \times 10^{-10}$ m [4.4×10^{-10} m] at 90% C.L. [95% C.L.]. Nevertheless, the gap remains quite large. Another type of experiments that might be relevant are based on the detection of spontaneous heating, which set a lower bound $R_0 \gtrsim 4.6 \times 10^{-2}$ Å [89]. This bound is two orders of magnitude lower than that from radiation, but it has the merit of being more robust to possible non-Markovian generalizations of the DP model. However, also in this case, the predicted increase is proportional to R_0^{-3}, requiring an improvement in sensitivity of 24 orders of magnitude to reach the upper bound.

Chapter 5

Conclusions

The investigation presented in this thesis addressed the interplay between quantum mechanics and gravity through the lens of collapse models and gravitationally induced decoherence. Despite the remarkable predictive power of quantum theory and the geometric elegance of general relativity, a fully consistent framework unifying the two remains elusive. One of the key open questions is how the quantum–to–classical transition arises and whether gravity itself might play an active role in this process.

Within this broader context, we have focused on two complementary approaches: the Diósi-Penrose model and the Károlyházy model. Although conceptually distinct, both share the central idea that gravitational phenomena may induce deviations from standard quantum mechanics. The DP model attributes the spontaneous collapse of the wave function to the gravitational self-energy of superpositions, while the Károlyházy model connects decoherence to stochastic fluctuations of the spacetime metric.

In the first part of the thesis, we reviewed the foundations of open quantum systems and collapse dynamics, providing the theoretical framework necessary to describe the emergence of classicality. We then analyzed the Károlyházy model, extending its formulation by relaxing the constraint that metric fluctuations satisfy a wave equation. This generalization led to a class of admissible correlation functions consistent with both theoretical conditions and experimental bounds. The resulting allowed range for the model's characteristic parameter R_K (valid for a Gaussian spatial correlation function and updated to $1.23\,\mathrm{m} \leq R_K \leq 1.98\,\mathrm{m}$) represents a narrowing of the admissible parameter interval. This work shows that, with appropriate assumptions on the stochastic structure of spacetime, Károlyházy's original intuition can be reconciled with current observations.

The second part focused on the DP model, investigating its capability to account

for the quantum-to-classical transition. Through analytical and numerical analyses, we found that the collapse becomes effective at the mesoscopic–macroscopic boundary, corresponding to systems containing 10^{10}–10^{12} atoms. Interestingly, in this regime, the collapse time is nearly independent of the parameter R_0 across several orders of magnitude. This finding suggests that the specific value of R_0 may be less critical to the emergence of classicality than previously assumed. We also explored non-Markovian generalizations of the DP model, showing that including physically motivated memory effects tends to increase the collapse time, thereby delaying the onset of classical behavior.

From an experimental standpoint, we discussed current and future efforts to constrain the parameter space of collapse models. In particular, non-interferometric tests based on spontaneous radiation or heating of crystalline systems provide the most stringent bounds on R_0. However, bridging the remaining gap between theory and experiment will require several orders of magnitude improvement in sensitivity. Notably, recent results by Aprile et al. [98] have already strengthened the existing limits, demonstrating the rapid progress in this field. Still, as discussed in this work, a rigid interpretation based solely on planar geometries would already exclude the model, while a relaxation toward three-dimensional objects, consistent with Penrose's argument [56], shifts the relevant bounds by approximately six orders of magnitude.

Overall, the results obtained in this thesis contribute to clarifying the domain of validity of gravitational collapse models and to identifying the theoretical and experimental challenges that remain open. Both the DP and Károlyházy models illustrate that gravity could provide a natural mechanism for wave-function reduction, although their ultimate physical interpretation still awaits experimental confirmation. The theoretical developments presented here lay the groundwork for future refinements, and the experimental progress expected in the coming years will be crucial to determine whether gravity indeed plays a role in the emergence of classicality from the quantum world.

Bibliography

[1] H.-P. Breuer and F. Petruccione, *The theory of open quantum systems* (OUP Oxford, 2002).

[2] A. Rivas and S. F. Huelga, *Open quantum systems*, Vol. 10 (Springer, 2012).

[3] H.-P. Breuer, E.-M. Laine, J. Piilo, and B. Vacchini, Reviews of Modern Physics **88**, 021002 (2016).

[4] I. De Vega and D. Alonso, Reviews of Modern Physics **89**, 015001 (2017).

[5] M. A. Schlosshauer, *Decoherence and the Quantum-To-Classical Transition* (Springer-Verlag Berlin Heidelberg, 2007).

[6] E. Joos, H. D. Zeh, C. Kiefer, D. J. Giulini, J. Kupsch, and I.-O. Stamatescu, *Decoherence and the appearance of a classical world in quantum theory* (Springer Science & Business Media, 2013).

[7] J. S. Bell, *Speakable and unspeakable in quantum mechanics: Collected papers on quantum philosophy* (Cambridge university press, 2004).

[8] A. Bassi and G. Ghirardi, Physics Reports **379**, 257 (2003).

[9] A. Bassi, K. Lochan, S. Satin, T. P. Singh, and H. Ulbricht, Rev. Mod. Phys. **85**, 471 (2013).

[10] G. Lindblad, Communications in mathematical physics **48**, 119 (1976).

[11] V. Gorini, A. Kossakowski, and E. C. G. Sudarshan, Journal of Mathematical Physics **17**, 821 (1976).

[12] W. H. Zurek, Reviews of modern physics **75**, 715 (2003).

[13] A. Bassi *et al.*, Oxford Research Encyclopedias (2021).

[14] E. Schrödinger, Naturwissenschaften **23**, 844 (1935).

[15] A. J. Leggett, Progress of Theoretical Physics Supplement **69**, 80 (1980).

[16] S. Weinberg, Physical Review Letters **62**, 485 (1989).

[17] G. C. Ghirardi, A. Rimini, and T. Weber, Phys. Rev. D **34**, 470 (1986).

[18] N. Gisin, Helv. Phys. Acta **62**, 363 (1989).

[19] A. Bassi, D. Dürr, and G. Hinrichs, Physical review letters **111**, 210401 (2013).

[20] A. Bassi, M. Dorato, and H. Ulbricht, Entropy **25**, 645 (2023).

[21] S. L. Adler and A. Bassi, J. Phys. A **40**, 15083 (2007).

[22] L. Arnold, New York, Wiley-Interscience, 1974. 243 p (1974).

[23] G. C. Ghirardi, P. Pearle, and A. Rimini, Physical Review A **42**, 78 (1990).

[24] M. Carlesso and S. Donadi, "Spontaneous collapse models," in *Encyclopedia of Mathematical Physics* (Elsevier, 2025) p. 237–253.

[25] L. Diósi, Physics Letters A **120**, 377 (1987).

[26] L. Diósi, Physical Review A **40**, 1165 (1989).

[27] R. Penrose, Gen. Rel. Grav. **28**, 581 (1996).

[28] G. Ghirardi, R. Grassi, and A. Rimini, Physical Review A **42**, 1057 (1990).

[29] R. Colella, A. W. Overhauser, and S. A. Werner, Physical Review Letters **34**, 1472 (1975).

[30] V. V. Nesvizhevsky, H. G. Börner, A. K. Petukhov, H. Abele, S. Baeßler, F. J. Rueß, T. Stöferle, A. Westphal, A. M. Gagarski, G. A. Petrov, *et al.*, Nature **415**, 297 (2002).

[31] J. B. Fixler, G. Foster, J. McGuirk, and M. Kasevich, Science **315**, 74 (2007).

[32] L. Diósi, Physics Letters A **105**, 199 (1984).

[33] G. Hooft, arXiv preprint gr-qc/9310026 (1993).

[34] C. Rovelli, Living Rev. Relativ. **1**, 1 (1998).

[35] M. B. Green, J. H. Schwarz, and E. Witten, *Superstring theory*, Vol. 2 (Cambridge university press, 2012).

[36] S. Adler, *Gravitation and the noise needed in objective reduction models* (in Quantum Nonlocality and Reality: 50 Years of Bell's Theorem, ed Mary Bell and Shan Gao, Cambridge University Press, 2016).

[37] B. S. DeWitt, Phys. Rev. **160**, 1113 (1967).

[38] S. Bose, A. Mazumdar, G. W. Morley, H. Ulbricht, M. Toroš, M. Paternostro, A. A. Geraci, P. F. Barker, M. Kim, and G. Milburn, Physical review letters **119**, 240401 (2017).

[39] C. Marletto and V. Vedral, Physical review letters **119**, 240402 (2017).

[40] M. Carlesso, A. Bassi, M. Paternostro, and H. Ulbricht, New Journal of Physics **21**, 093052 (2019).

[41] C. Anastopoulos and B.-L. Hu, Classical and Quantum Gravity **37**, 235012 (2020).

[42] R. Penrose, Foundations of Physics **44**, 557 (2014).

[43] J.-G. Demers and C. Kiefer, Physical Review D **53**, 7050 (1996).

[44] M. Parikh, F. Wilczek, and G. Zahariade, International Journal of Modern Physics D **29**, 2042001 (2020).

[45] S. Kanno, J. Soda, and J. Tokuda, Physical Review D **103**, 044017 (2021).

[46] A. Bassi, A. Großardt, and H. Ulbricht, Classical and Quantum Gravity **34**, 193002 (2017).

[47] M. Bell and S. Gao, *Quantum nonlocality and reality: 50 years of Bell's Theorem* (Cambridge University Press, 2016).

[48] G. Gasbarri, M. Toroš, S. Donadi, and A. Bassi, Physical Review D **96**, 104013 (2017).

[49] S. Donadi and A. Bassi, AVS Quantum Science **4** (2022).

[50] F. Karolyhazy, Il Nuovo Cimento A (1965-1970) **42**, 390 (1966).

[51] R. Penrose and C. J. Isham, (1986).

[52] F. Károlyházy, in *Sixty-Two Years of Uncertainty: Historical, Philosophical, and Physical Inquiries into the Foundations of Quantum Mechanics* (Springer, 1990) pp. 215–231.

[53] D. Kafri, J. Taylor, and G. Milburn, New Journal of Physics **16**, 065020 (2014).

[54] A. Tilloy and L. Diósi, Physical Review D **93**, 024026 (2016).

[55] J. Oppenheim, Phys. Rev. X **13**, 041040 (2023).

[56] R. Penrose, "Mathematical physics," (London: Imperial College Press, 2000) Chap. Wavefunction collapse as a real gravitational effect, pp. 266–82.

[57] C. Møller, H. Bondi, P. Vigoureux, H. Dingle, and L. Essen, Proceedings of the Royal Society of London. Series A, Mathematical and Physical Sciences **270**, 306 (1962).

[58] L. Rosenfeld, Nuclear Physics **40**, 353 (1963).

[59] M. Bahrami, A. Großardt, S. Donadi, and A. Bassi, New Journal of Physics **16**, 115007 (2014).

[60] K. Jacobs and D. A. Steck, Contemporary Physics **47**, 279 (2006).

[61] H. M. Wiseman and G. J. Milburn, *Quantum Measurement and Control* (Cambridge University Press, 2010).

[62] H. M. Wiseman, Phys. Rev. A **49**, 2133 (1994).

[63] J. L. Gaona-Reyes, M. Carlesso, and A. Bassi, Physical Review D **103**, 056011 (2021).

[64] D. N. Page and C. D. Geilker, Physical Review Letters **47**, 979 (1981).

[65] I. Layton and J. Oppenheim, PRX Quantum **5**, 020331 (2024).

[66] E. Wigner, Phys. Rev. **40**, 749 (1932).

[67] M. Hillery, R. F. O'Connell, M. O. Scully, and E. P. Wigner, Phys. Rep. **106**, 121 (1984).

[68] L. Figurato, A. Bassi, and S. Donadi, New Journal of Physics **26**, 013001 (2024).

[69] L. Diósi and B. Lukacs, Physics Letters A **142**, 331 (1989).

[70] L. Diósi and B. Lukács, Physics Letters A **181**, 366 (1993).

[71] L. Diósi and B. Lukács, Il Nuovo Cimento B (1971-1996) **108**, 1419 (1993).

[72] Q. Fu, Physical Review A **56**, 1806 (1997).

[73] S. L. Adler and F. M. Ramazanoglu, Journal of Physics A: Mathematical and Theoretical **42**, 109801 (2009).

[74] S. L. Adler, A. Bassi, and S. Donadi, Journal of Physics A: Mathematical and Theoretical **46**, 245304 (2013).

[75] S. Donadi, K. Piscicchia, R. Del Grande, C. Curceanu, M. Laubenstein, and A. Bassi, The European Physical Journal C **81**, 1 (2021).

[76] I. Arnquist, F. Avignone III, A. Barabash, C. Barton, K. Bhimani, E. Blalock, B. Bos, M. Busch, M. Buuck, T. Caldwell, *et al.*, Physical Review Letters **129**, 080401 (2022).

[77] M. Carlesso, S. Donadi, L. Ferialdi, M. Paternostro, H. Ulbricht, and A. Bassi, Nature Physics **18**, 243 (2022).

[78] S. Donadi, K. Piscicchia, C. Curceanu, L. Diósi, M. Laubenstein, and A. Bassi, Nature Physics **17**, 74 (2021).

[79] S. Bera, S. Donadi, K. Lochan, and T. P. Singh, Foundations of Physics **45**, 1537 (2015).

[80] S. Donadi, D.-A. Deckert, and A. Bassi, Annals of Physics **340**, 70 (2014).

[81] P. Pearle, Physical Review D **13**, 857 (1976).

[82] S. L. Adler and A. Bassi, Science **325**, 275 (2009).

[83] S. Donadi, L. Ferialdi, and A. Bassi, Physical Review Letters **130**, 230202 (2023).

[84] A. Vinante, M. Bahrami, A. Bassi, O. Usenko, G. Wijts, and T. Oosterkamp, Physical review letters **116**, 090402 (2016).

[85] A. Vinante, R. Mezzena, P. Falferi, M. Carlesso, and A. Bassi, Physical review letters **119**, 110401 (2017).

[86] S. L. Adler, A. Bassi, M. Carlesso, and A. Vinante, Physical Review D **99**, 103001 (2019).

[87] M. Bahrami, Physical Review A **97**, 052118 (2018).

[88] S. L. Adler and A. Vinante, Physical Review A **97**, 052119 (2018).

[89] A. Vinante and H. Ulbricht, AVS Quantum Science **3** (2021).

[90] C. Kittel, *Elementary solid state physics: a short course* (Wiley, 1962).

[91] J. Callaway, *Quantum theory of the solid state* (Academic press, 2013).

[92] L. Mandel and E. Wolf, *Optical coherence and quantum optics* (Cambridge University Press, 1995).

[93] R. Loudon, *The quantum theory of light* (OUP Oxford, 2000).

[94] J. Garrison and R. Chiao, *Quantum optics* (OUP Oxford, 2008).

[95] L. Kantorovich, *Quantum theory of the solid state: an introduction*, Vol. 136 (Springer Science & Business Media, 2004).

[96] K. Gloos, P. Smeibidl, C. Kennedy, A. Singsaas, P. Sekowski, R. Mueller, and F. Pobell, Journal of low temperature physics **73**, 101 (1988).

[97] M. Toroš, G. Gasbarri, and A. Bassi, Physics Letters A **381**, 3921 (2017).

[98] E. Aprile, J. Aalbers, K. Abe, S. A. Maouloud, L. Althueser, B. Andrieu, E. Angelino, D. A. Martin, S. Armbruster, F. Arneodo, *et al.*, arXiv preprint arXiv:2506.05507 (2025).

[99] L. Figurato, M. Dirindin, J. L. Gaona-Reyes, M. Carlesso, A. Bassi, and S. Donadi, New Journal of Physics **26**, 113004 (2024).

[100] M. Bahrami, A. Smirne, and A. Bassi, Physical Review A **90**, 062105 (2014).

[101] R. Howl, R. Penrose, and I. Fuentes, New Journal of Physics **21**, 043047 (2019).

[102] G. Di Bartolomeo, M. Carlesso, K. Piscicchia, C. Curceanu, M. Derakhshani, and L. Diósi, Physical Review A **108**, 012202 (2023).

[103] G. Di Bartolomeo and M. Carlesso, New Journal of Physics **26**, 043006 (2024).

[104] A. A. Tomaz, R. S. Mattos, and M. Barbatti, Phys. Chem. Chem. Phys. **26**, 20785 (2024).

[105] M. Toroš and A. Bassi, Journal of Physics A: Mathematical and Theoretical **51**, 115302 (2018).

[106] A. Tilloy and T. M. Stace, Physical Review Letters **123**, 080402 (2019).

[107] B. Helou, B. Slagmolen, D. E. McClelland, and Y. Chen, Physical Review D **95**, 084054 (2017).

[108] P. Blake, E. Hill, A. Castro Neto, K. Novoselov, D. Jiang, R. Yang, T. Booth, and A. Geim, Applied physics letters **91** (2007).

[109] G. H. Jacobs, *Comparative psychology of vision* (Wiley Online Library, 2003) pp. 47–70.

[110] C. M. Savage and D. F. Walls, Physical Review A **32**, 2316 (1985).

[111] A. Smirne and B. Vacchini, Physical Review A **82**, 042111 (2010).

[112] G. Yang, L. Li, W. B. Lee, and M. C. Ng, Science and Technology of Advanced Materials **19**, 613 (2018).

[113] S. K. Lam, A. Pitrou, and S. Seibert, in *Proceedings of the Second Workshop on the LLVM Compiler Infrastructure in HPC*, LLVM '15 (Association for Computing Machinery, New York, NY, USA, 2015).

[114] W. Marshall, C. Simon, R. Penrose, and D. Bouwmeester, Physical Review Letters **91**, 130401 (2003).

[115] L. Diósi and W. T. Strunz, Physics Letters A **235**, 569 (199).

[116] A. Bassi and G. Ghirardi, Physical Review A **65**, 042114 (2002).

[117] A. Bassi and L. Ferialdi, Physical Review A **80**, 012116 (2009).

[118] M. Carlesso, L. Ferialdi, and A. Bassi, The European Physical Journal D **72**, 1 (2018).

[119] K. Piscicchia, S. Donadi, S. Manti, A. Bassi, M. Derakhshani, L. Diósi, and C. Curceanu, Physical Review Letters **132**, 250203 (2024).

UNIVERSITÀ
DEGLI STUDI
DI TRIESTE

La borsa di dottorato è cofinanziata con risorse dell'Unione europea – Piano Nazionale di Ripresa e Resilienza, Progetto PNRR – M4C2 - Investimento 1.3 – NexGenerationEU – Codice Progetto PE0000023, Programma Partenariati Estesi "National Quantum Science and Technology Institute (NQSTI)" – CUP J93C22001510006